UNIVERSITY OF CALIFORNIA SAN DIEGO

The More The Brighter: Coupling and Emission Tunability in High-beta Telecom-band Semiconductor Nanolasers

A dissertation submitted in partial satisfaction of the
requirements for the degree
Doctor of Philosophy

in

Electrical Engineering (Nanoscale Devices and Systems)

by

Suruj Sambhav Deka

Committee in charge:

Professor Yeshaiahu Fainman, Chair
Professor Richard Averitt
Professor Eric Fullerton
Professor Zhaowei Liu
Professor Paul Yu

2021

The dissertation of Suruj Sambhav Deka is approved, and it is acceptable in quality and form for publication on microfilm and electronically.

University of California San Diego

2021

DEDICATION

To my parents, for their unwavering support and love and for always wanting what is best for me.

To my sister, for being a partner in crime and for keeping me grounded with her unfiltered truth.

To my friends, for replacing the serious with the silly in my life when much needed.

And finally and most importantly, to my wife, for being the rock in my life and the perfect companion on this long journey that was the PhD.

EPIGRAPH

The greatest glory in living lies not in never failing, but in rising every time we fall.

Nelson Mandela

TABLE OF CONTENTS

LIST OF FIGURES

LIST OF TABLES

ACKNOWLEDGEMENTS

I would like to thank my family and friends who have played various supporting roles to keep me motivated and strong on this long, arduous journey that has been the PhD. I truly cannot imagine getting to this stage without all of you by my side!

I would also like to thank my academic advisor, Shaya, and the rest of my committee members, colleagues that have come and gone with whom I had the pleasure of working and also the staff at UCSD's research facilities like the cleanroom for their invaluable guidance and encouragement. I have learned something valuable from each of you!

Chapter 2, in full, is a reprint of the material as it appears in S.S. Deka, S.H. Pan, S. Jiang, A. El Amili, F. Vallini, Q. Gu, and Y. Fainman "Real-Time Dynamic Wavelength Tuning and Intensity Modulation of Metal-Clad Nanolasers," *Optics Express*, Vol. 28, Issue 19, pp. 27346-27357, 2020. The dissertation author was the primary investigator and author of this publication.

Chapter 3, in part, is a reprint of the material as it appears in S.S. Deka, S.H. Pan, Q. Gu, Y. Fainman, and A. El Amili "Coupling in a dual metallo-dielectric nanolaser system," *Optics Letters*, Vol. 42, Issue 22, pp. 4760-4763, 2017. The dissertation author was the primary investigator and author of this publication. Chapter 3 section 3.4, in full, is a reprint of the material as it appears in S.H. Pan, S.S. Deka, A. El Amili, Q. Gu, and Y. Fainman "Nanolasers: second-order intensity correlation, direct modulation and electromagnetic isolation in array architectures," *Progress in Quantum Electronics*, Vol. 59, pp. 1-18, 2018. The dissertation author contributed to the measurements of high-speed and writing of the coupling section for this publication.

Chapter 4, in full, has been submitted for publication of the material as it may appear in S. Jiang, S. S. Deka, S. H. Pan and Y. Fainman "Effects of High-β on Phase-locking Stability and Tunability in Laterally Coupled Lasers". The dissertation author was co-first author and contributed to the main idea of analyzing stability for high-β nanolasers, the discussion and writing of the manuscript.

Chapter 5, in full, is a reprint of the material as it appears in S.S. Deka, S. Jiang, S.H. Pan, and Y. Fainman ”Nanolaser arrays: toward application-driven dense integration,” *Nanophootnics*, Vol. 10, Issue 1, pp. 149-169, 2021. The dissertation author was the primary investigator and author of this publication.

Chapter 6, in part, is a reprint of the material as it appears in S.S. Deka, S. Jiang, S.H. Pan, and Y. Fainman ”Nanolaser arrays: toward application-driven dense integration,” *Nanophootnics*, Vol. 10, Issue 1, pp. 149-169, 2021. The dissertation author was the primary investigator and author of this publication.

VITA

2015	Bachelor of Engineering in Electrical Engineering (magna cum laude), Vanderbilt University, Tennessee
	Master of Science in Electrical Engineering (accelerated 4 year dual-degree bachelors-masters program), Vanderbilt University, Tennessee
2021	Ph.D in Electrical Engineering (Nanoscale Devices and Systems), University of California, San Diego

PUBLICATIONS

S.S. Deka, S.H. Pan, Q. Gu, Y. Fainman, and A. El Amili “Coupling in a dual metallo-dielectric nanolaser system,” *Optics Letters*, Vol. 42, Issue 22, pp. 4760-4763, 2017.

S.S. Deka, S.H. Pan, S. Jiang, A. El Amili, F. Vallini, Q. Gu, and Y. Fainman “Real-Time Dynamic Wavelength Tuning and Intensity Modulation of Metal-Clad Nanolasers,” *Optics Express*, Vol. 28, Issue 19, pp. 27346-27357, 2020.

S.S. Deka, S. Jiang, S.H. Pan, and Y. Fainman ”Nanolaser arrays: toward application-driven dense integration,” *Nanophotonics*, Vol. 10, Issue 1, pp. 149-169, 2021.

S. Jiang, **S. S. Deka**, S. H. Pan and Y. Fainman “Effects of High-β on Phase-locking Stability and Tunability in Laterally Coupled Lasers”, submitted.

S.H. Pan, **S.S. Deka**, A. El Amili, Q. Gu, and Y. Fainman “Nanolasers: second-order intensity correlation, direct modulation and electromagnetic isolation in array architectures,” *Progress in Quantum Electronics*, Vol. 59, pp. 1-18, 2018.

S. Jiang, S. H. Pan, **S. S. Deka**, C.-Y. Fang, Z. Chen, Y. Fainman, and A. El Amili, “Impact of Fundamental Temperature Fluctuations on the Frequency Stability of Metallo dielectric Nanolasers,” *IEEE Journal of Quantum Electronics*, Vol. 55, Issue 5, pp. 1-10, 2019.

Z. Chen, **S. S. Deka**, S. H. Pan, S. Jiang, C.-Y. Fang, Y. Fainman, and A. El Amili, “Intensity noise and bandwidth analysis of nanolasers via optical injection,” *Optics Express*, Vol. 27, Issue 6, pp. 8186-8194, 2019.

ABSTRACT OF THE DISSERTATION

The More The Brighter: Coupling and Emission Tunability in High-beta Telecom-band Semiconductor Nanolasers

by

Suruj Sambhav Deka

Doctor of Philosophy in Electrical Engineering (Nanoscale Devices and Systems)

University of California San Diego, 2021

Professor Yeshaiahu Fainman, Chair

The emergence of nanolasers over the past two decades has helped enable a plethora of novel applications such as optical communications, on-chip interconnects, sensing and super-resolution imaging. Particularly for the field of computing/communication, nanolasers have become an intriguing area of research as photonic integrated circuits (PICs) of the future would require nanoscale light sources. To that end, nanolasers based on a variety of architectures and underlying physics have been demonstrated in the literature. Metallo-dielectric nanolasers (MDNLs) are particularly attractive since they combine the advantages of ultrasmall footprints and low thresholds offered by other nanolaser types while still offering electromagnetic isolation, telecom-band operation and current injection. In this dissertation, we mainly focus on exploring additional attributes of MDNLs that further lend credence to their suitability for dense integration on-chip. One of these desirable traits we study includes reversible wavelength tuning (upto 8.35 nm) and intensity modulation of an MDNL based on an external electric field (Chapter 2). More importantly, we report that this electric-field based intensity modulation can be performed at high-speeds of upto 400 MHz (limited only by the detector bandwidth). A second characteristic appropriate for dense integration involves investigating the presence of coupling when two MDNLs are designed in proximity on-chip (Chapter 3). Our results indicate that not only does coupling occur, but it can also be inhibited if independent operation of the emitters is required. We further explore the concept of coupling but with regards to phase-locking two high-β, laterally coupled lasers (Chapter 4). We found that high β values, that are usually only exhibited in nanolasers such as MDNLs, help significantly increase the stable phase-locking regions for two coupled lasers. Additionally, high β can also lead to a wider range of phase differences attainable for a stable nanolaser system (π) compared to what has been demonstrated for commercially available semiconductor lasers ($\pi/10$). Finally, we review some unique applications that have already been made possible by the inevitable next step in the nanolaser technology of integrating into dense arrays (Chapter 5) and we briefly discuss a couple of future directions that are worth pursuing in the nanolaser-arrays research field (Chapter 6).

Chapter 1

Introduction

In 1960, working for Hughes Research Laboratories, Theodore Maiman demonstrated the first ever laser based on ruby crystals; at the time, he remarked that the "laser is a solution looking for a problem" [1, 2]. Since this monumental breakthrough, lasers have been purposed to solve problems in myriad aspects of human life - from being used for optical storage, to barcode scanners and even in measuring interstellar distances between astronomical objects. In the past two decades, however, the focus has shifted from the macroscopic to the microscopic as the growth in nanotechnology has led to efforts towards the miniaturization of lasers. Such nanometer scale sources or nanolasers, can enable a plethora of novel applications ranging from optical communications and on-chip interconnects [3] to sensing [4] and super-resolution imaging [5]. Particularly for the field of computing/communication, nanolasers have become an intriguing area of research as photonic integrated circuits (PICs) of the future would require nanoscale light sources. To that end, nanolasers have been demonstrated based on a wide variety of geometric designs and their accompanying physics. One type is the photonic crystal nanolaser (PCN), an example of which is demonstrated in Fig. 1.1(a) below. Widely reported in the literature, PCNs are characterized by compact effective optical mode volumes but sizable total device dimensions due to the multiple dielectric layers used for confinement [6–11]. Along with PCNs,

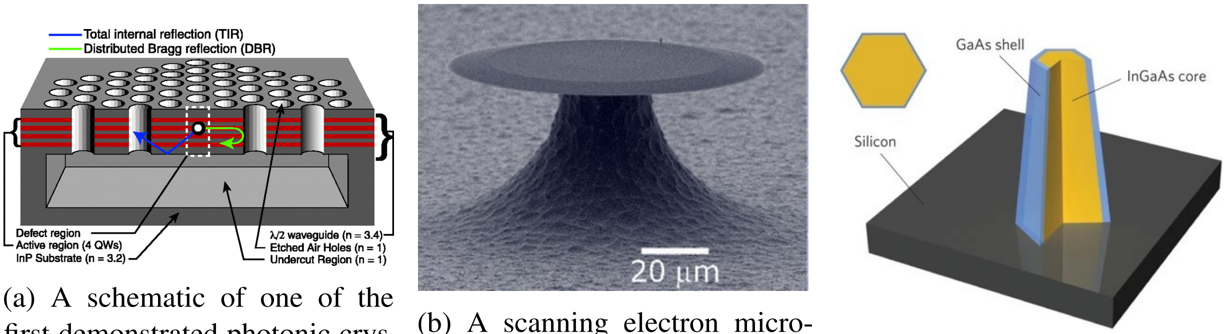

(a) A schematic of one of the first demonstrated photonic crystal nanolasers (Reprinted from Ref. [6]).

(b) A scanning electron microscope (SEM) image of an Er-doped SiO_2 microcavity laser (Reprinted from Ref. [13]).

(c) A schematic of a nanocavity pillar laser (Reprinted from Ref. [14]).

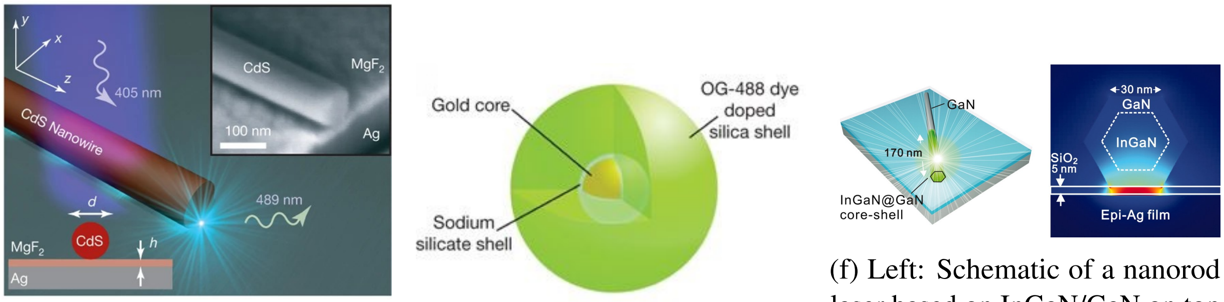

(d) Schematic of a SPASER based on a CdS nanowire fabricated on top of a Ag substrate and separated by a layer of MgF_2. Inset: SEM image of structure (Reprinted from Ref. [16]).

(e) Schematic of nanoparticle SPASER with a gold core encased in a dye-doped silica shell (Reprinted from Ref. [17]).

(f) Left: Schematic of a nanorod laser based on InGaN/GaN on top of a SiO_2-clad epitaxial Ag film. Right: Energy-density distribution of the structure (Reprinted from Ref. [18]).

Figure 1.1: Examples of dielectric and SPASER-based miniature lasers demonstrated in the literature

microdisk [12, 13] and nanopillar cavity lasers [14], shown in Fig. 1.1(b) and 1.1(c) respectively, are other examples of microscopic lasers based purely on dielectric cavities. This category of lasers generally exhibit a subwavelength optical mode in all three dimensions but usually suffer from poor electromagnetic isolation relative to other types of miniature lasers. This is due to the fact that reducing a resonator size in all three dimensions usually leads to spatial spreading of the optical mode beyond the resonator's physical boundaries [15].

To combat this issue, nanolasers relying on amplification of surface plasmons to achieve lasing have also been demonstrated. Named SPASERs (surface plasmon amplification by stimulated emission of radiation) [19], such lasers have been shown based on nanowire [16], nanoparticle [17] and nanorod cavities [18] among others as shown in Fig 1.1(d)-(f), respectively. Light is also tightly confined in such SPASERs but unlike in dielectric-cavity based sources, the use of metal in SPASERs restricts the optical mode from leaking out of the active medium, thereby ensuring electromagnetic isolation from the surrounding environment. However, most implementations of SPASERs in the literature thus far emit in the visible range and are usually optically pumped. Nanolasers intended for practical use in communication purposes would require both current injection as well as emission in the telecom bands used for fiber optics ($\sim$1260-1625 nm).

In this respect, another category of nanolasers based on metallic cladding offers advantages that make them the most suitable for use as light sources for on-chip communication purposes. These metal-clad nanolasers (MCNL) have been primarily demonstrated in two designs - the metallo-dielectric nanolaser (MDNL) [20–25] and the coaxial nanolaser (CNL) [26, 27]. Both designs are similar to SPASERs in that they also require a metallic cladding to help confine the optical mode to the active medium but MDNLs and CNLs offer the added advantages of being compatible with current injection while also operating in the telecom bands. Additionally, a fundamental difference between SPASERs and MCNLs is that the lasing modes in the latter tend to be photonic modes as opposed to plasmonic ones seen in the former. Therefore, MDNL and CNL types combine the telecom band operation afforded in purely dielectric designs with electromagnetic isolation exhibited in SPASERs while simultaneously allowing for electrical contacts needed for current injection [23, 25].

The design of a typical MDNL is shown in Fig. 1.2, better elucidating both the metal cladding that envelops the entire structure and the vertical emission from this type of resonator. Of particular importance is the thin dielectric shield deposited in between the InGaAsP gain medium and the Ag metal. This $\sim$200 nm layer of dielectric (in this case, SiO_2) plays a crucial role of acting as a buffer layer to prevent the metal from directly contacting the gain medium. Although metal helps increase the mode-gain overlap by restricting the spatial spread of the

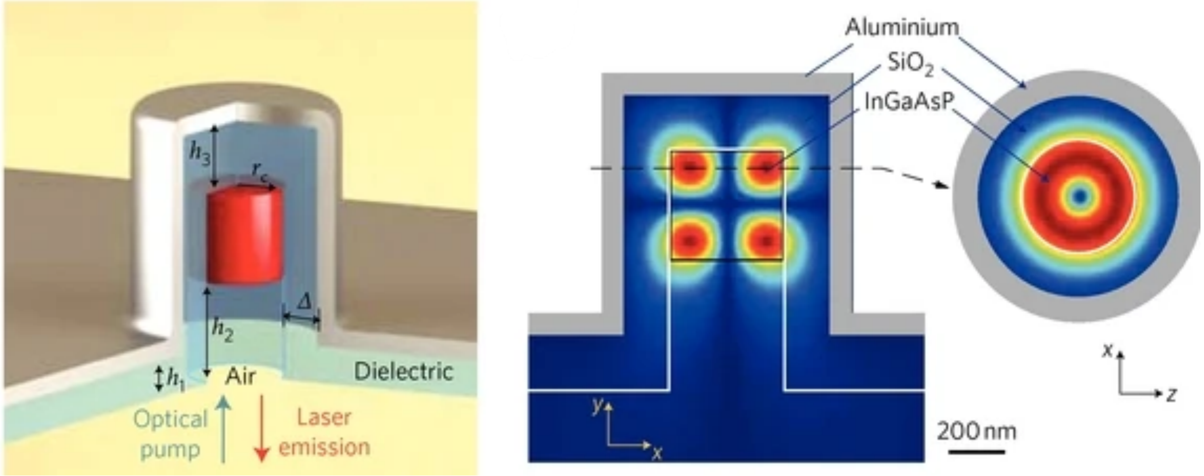

Figure 1.2: Left: Schematic of an MDNL with an InGaAsP gain core which is surrounded by a thin SiO_2 shield and Ag cladding. The nanolaser is pumped vertically and emits in the same direction. Right: Cross-sections of the electric field intensity ($|E|^2$) profile for the TE_{012} mode supported in the cavity (Reprinted from Ref. [20]).

mode, the dielectric shield reduces the mode-metal overlap which prevents the gain medium from experiencing increased losses from the metal [20]. Due to this combination of metal and dielectric, MDNLs offer truly subwavelength operation, in terms of both the optical mode as well as the device footprint. The presence of the dielectric shield is also the reason why the photonic modes supported in the MDNL cavity exhibit higher quality (Q) factors than the plasmonic cavity modes as illustrated in Fig. 1.3. A CNL, illustrated in Fig. 1.4, offers a similar infinitesimal footprint to the MDNL but lacks a dielectric shield and has not been demonstrated to operate at room temperature like an MDNL; CNLs usually require cryogenic ambient temperature to overcome the losses and lase. In return, however, certain CNLs can offer the highly desirable attribute of exhibiting unity-β if designed appropriately [26].

In fact, both MDNLs and CNLs can demonstrate high β factors, which is the fraction of spontaneous emission funneled into the lasing mode compared to all other modes. Conventionally, coherence is determined via the kink observed in the S-shaped light output vs. light/current(I) input curve (LL/LI curve) [24]. However, as the β factor increases by orders of magnitudes in nanolasers compared to commercial diode lasers, this kink becomes increasingly difficult to

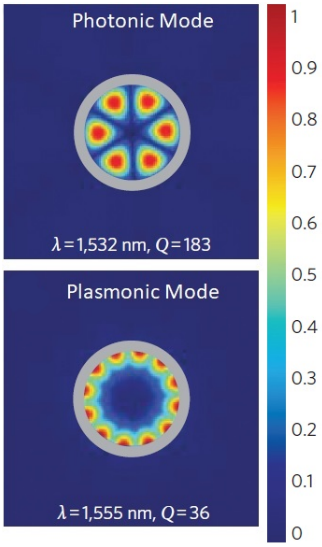

Figure 1.3: Profiles of $|E|^2$ showcasing the difference between a photonic (top) and plasmonic mode (bottom). The latter experiences higher losses from the metal and therefore, demonstrates a lower Q than the former (Reprinted from Ref. [20]).

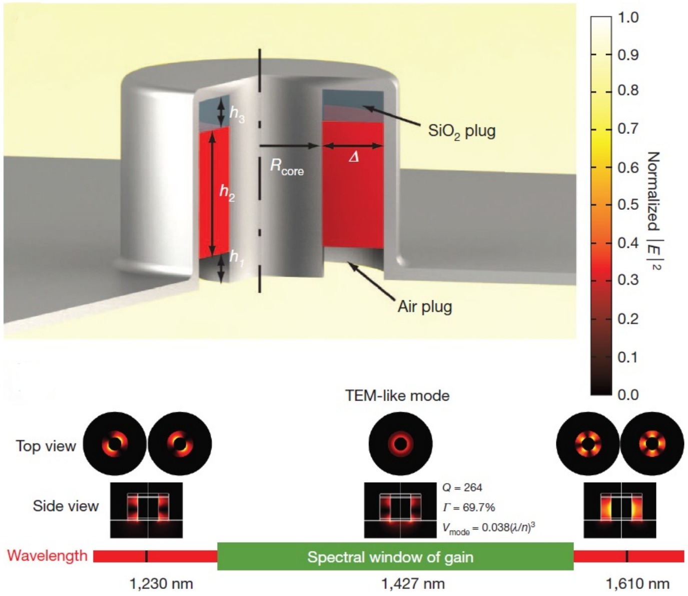

Figure 1.4: Top: Schematic of a CNL illustrating the absence of a conformal dielectric shield. Bottom: Electromagnetic modal profiles demonstrating the resonant modes supported in the cavity. Depending on the design of the CNL, only one TEM-like mode may be supported in the spectral window of the gain as shown here. The presence of only one cavity mode results in a unity-β nanolaser (Reprinted from Ref. [26]).

discern. Indeed, at the maximum possible value that β can attain of 1, the kink altogether vanishes and the LL curve is found to be completely linear [28]. This behavior, sometimes referred to as a laser being "thresholdless", has been observed in CNLs due to their unique structure which supports only one cavity mode in the entire gain-bandwidth window [26]. Though a unity-β is not usually exhibited by MDNLs, their spontaneous emission factors are still fairly high (0.1 to $\sim$1) for them to also exhibit high energy efficiency (since lasing threshold theoretically reduces with increasing β) like their metal-clad CNL counterparts. Since low power consumption is usually desirable for most systems, energy efficiency is a major reason for why high-β factors are desirable in nanolasers intended for on-chip uses. However, sources with high-β also provide additional benefits. For instance, for a nanolaser to exhibit high-β, the mode volume of the resonator is required to be infinitesimal to restrict the number of modes supported in the cavity to a handful. Usually, for cavities with such ultra-small mode volumes, the spontaneous emission rate is enhanced owing to the Purcell effect [28, 29]. Consequentially, high-β nanolasers can theoretically exhibit modulation at much higher speeds than sources with lower-β factors. Another important advantage that will be discussed in detail in Chapter 4 of this thesis, is that higher-β can aid in the phase locking of coupled nanolasers. As is evident, high-β in nanolasers offers its own entire suite of key traits expected in an ideal chipscale light source.

Owing to the numerous advantages listed above such as their subwavelength size in all three dimensions, electromagnetic isolation, telecom band operation and also high-β factors, most of this thesis work is focused on studying MDNLs. The reason for choosing MDNLs over CNLs is that the former has been shown to achieve lasing at room temperature [20], a quality desirable in any practical device. In particular, in this thesis, we will discuss our work on three particular attributes of MDNLs that are also desirable for an on-chip source in addition to the ones they already possess - real-time wavelength tuning, high-speed emission modulation and coupling between nanolasers. We begin by detailing the dynamic wavelength tuning and high-speed modulation of an MDNL in Chapter 2. Though wavelength tuning has been previously demonstrated in nanolasers in the literature, most of the methods shown are either irreversible in nature (varying material composition [30, 31], altering cavity geometry [32, 33] etc.) or cannot be repeated at high speeds (index [34], temperature [35] or pressure-based variations [36]). Instead, by applying an external electric field to our MDNL, we observe wavelength alterations that are reversible and occur in real-time [37]. In addition, we also demonstrate high-speed modulation of MDNLs via the same technique of applying an external electric field. The ability to self-tune a laser and control its intensity in this manner can prove to be crucial for dense wavelength division multiplexing (WDM) applications at a chipscale level [37].

While it is necessary to first grasp the fundamental physics governing a single nanolaser, it would seldom be the case that a single such laser works in isolation in any real-world device or application; rather, multiple such emitters are likely to work in tandem. Consequentially, it becomes imperative to investigate how such emitters would interact or couple with one another. In Chapter 3, we consider the case of two MDNLs and investigate at what intercavity distances does near-field evanescent coupling become pronounced. Though intuitively, one would expect the metal to prevent any optical cross-talk between the neighboring resonators, our study shows that when designed close enough together, the two MDNLs interact via near-field evanescence despite the presence of the metal [15]. Since some applications might require the two sources to operate independently without cross-talk, we also discuss a way in which coupling may be inhibited between the two MDNLs.

In Chapter 4, we dive into further detail about the specifics of coupling but with regards to achieving phase locking between two laterally coupled lasers. Attaining stable phase locking between elements of a laser array hold immense value for development of high-power and coherent optical beams which are desirable for applications such as LiDAR. It had been postulated in past literature, in a time before nanolasers were ubiquitous in the field of nanophotonics, that higher β factors can increase the stability region between coupled semiconductor lasers [38, 39]. Now, with the growth of nanolaser technology over the past few decades, we decided to numerically analyze the effect of increasing β in the coupled rate equations for two semiconductor lasers. Confirming the hypothesis of the earlier studies, we found that high-β values do indeed lead to increased regions of stability between the two laterally coupled lasers considered despite varying control parameters such as the pump rate, frequency detuning and coupling coefficient. Additionally, we demonstrate that higher β values can lead to increased tunability for the steady-state phase differences between coupled lasers provided they are asymmetrically pumped. These results further encapsulate how high-β nanolasers, such as MDNLs, can form the building-blocks for densely packed optical phased arrays on chip.

In Chapter 5 we briefly discuss how nanolasers seem to be headed towards the inevitable direction of dense integration into arrays and lattices and some of the unique applications that have resulted [40]. Finally, we conclude the thesis with Chapter 6 and offer some future perspectives on some novel applications and coupling schemes yet to be explored and experimentally demonstrated [40].

Chapter 2

Real-time dynamic wavelength tuning and intensity modulation of metal-clad nanolasers

2.1 Introduction

As discussed in Chapter **??**, various types of nanolasers have been demonstrated over the better part of the past two decades such as those based on photonic crystals [6–11, 41], nanowires [16, 30, 31, 36, 42] and metallo-dielectric cavities [20, 21, 23–25] to list a few. Along with their nanoscale dimensions and in the case of metal-clad cavities, even subwavelength footprints, most such nanolasers have been shown to demonstrate qualities ideal for an on-chip source such as low thresholds [16,26], dense-integration capability [15,43] and electrical injection with room-temperature operation [22]. Another characteristic that can prove to be of great value for these sources is the ability to shift their wavelength of emission as well as to modulate their output intensity at high speeds. Control over the emission wavelength and intensity would be especially well-suited for dense wavelength division multiplexing (WDM) applications at a chip-scale level [44]. Additional applications include lidar systems, virtual/augmented reality devices and imaging/sensing.

Widespread efforts to control the emission wavelength of nanocavity lasers have been reported thus far based on differing physics [45]. Examples of wavelength tuning mechanisms include varying the material composition of the active medium to alter the bandgap [30, 31, 46, 47], physically transforming the size or shape of the cavity [32, 33, 48], altering the refractive index of the environment [34], applying pressure [36, 49] as well as inducing a temperature-dependent Varshni shift of the bandgap [35]. Despite the plethora of methods, the above-mentioned approaches exhibit certain shortcomings. For instance, in devices where the material composition is varied or the cavity geometry is modified, the alterations made are static and irreversible whereas ideally, the tuning should be dynamic (in other words, achieved in a reversible manner) and in real-time. Although mechanisms based on index, pressure and temperature are reversible, the bandwidths achieved via these methods reach a few MHz at best, while on-chip communications require much higher speeds. Similarly, despite studies demonstrating high-speed intensity modulation of nanolasers [7,10,27,28], most of the methods involve direct modulation of the pump and then the response of the nanolaser is shown to merely follow the pump modulation. In these cases, introducing independence between the pump and the modulation scheme would allow for an extra degree of freedom in controlling the emission intensity.

In this chapter, we describe how we simultaneously tune the emission wavelength as well as alter the output light intensity from a metallo-dielectric nanolaser. The mechanism is based on applying an external electric field to the nanolaser device which induces modifications in both the overlap of the electron and hole wavefunctions as well as the bound state energies via the quantum-confined Stark effect (QCSE). Since the alterations to the bandgap are due to electronic effects, it is possible to attain much higher speeds than bandgap modifications based on pressure or temperature [3]. We show that tuning based on external field is both reversible in nature and offers a fine range of tuning. Using this scheme, we demonstrate intensity modulation of up to 400

MHz, limited only by the detector bandwidth, as a proof of concept for our nanolaser's high-speed capability. Additionally, we complement the dynamic fine-tuning results with geometry-based coarse-tuning ones by altering the cavity design. This is the first exploration of real-time tuning and high-speed modulation of metal-clad nanolasers based on external field, to the best of our knowledge. These results lay the path for future work on attaining room-temperature, high-speed, tunable nanolasers under electrical injection for possible applications in on-chip data communications, lidar, virtual/augmented reality devices and imaging/sensing.

This chapter is organized into five sections. In section 2.2, some insight into the design and fabrication of the multiple quantum well (MQW) nanocavity is provided along with spectral characterization confirming lasing at room-temperature. Additionally, geometry-based coarse tuning is demonstrated by altering the cavity size of the nanolasers. In section 2.3, we present our experimental results on the continuous fine-tuning of the lasing wavelength as well as high-speed modulation based on an external field. The experimental and theoretical results are compared and discussed in section 2.4 and finally, section 2.5 concludes the manuscript.

2.2 Device design and geometry-based coarse wavelength tuning

The design and fabrication of the metallo-dielectric nanocavity shown in this chapter is built upon the device first reported by Nezhad et al. [20] with certain modifications to enable external E-field application. First, the gain comprises of 300 nm of InGaAsP multiple quantum wells (MQWs) with wells and barriers of 10 and 20 nm thickness, respectively. Secondly, Al_2O_3 serves as the dielectric shield instead of the more commonly used SiO2 owing to better thermal conductivity of the former [23]. In order to apply an electric field to tune/modulate the emission from the cavity, two additional fabrication steps were added as illustrated in the device schematic in Fig. 2.1(a). A layer of SiO_2 ($\sim$500 nm) was deposited to function as the insulator and then a

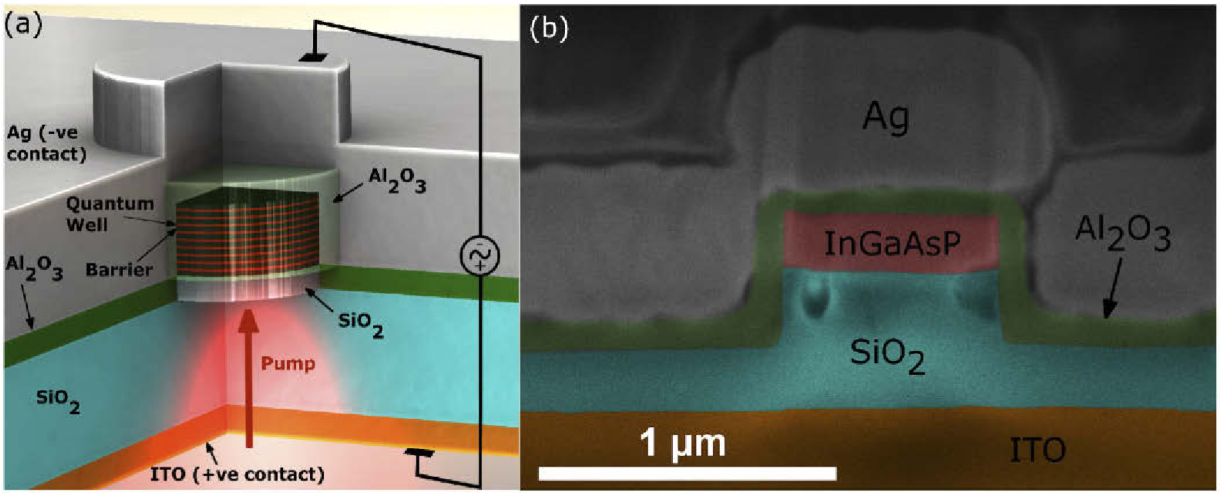

Figure 2.1: (a) Device schematic of metallo-dielectric nanolaser with constituent materials labeled. The gain comprises 10 nm thick InGaAsP quantum wells (shown in red) and 20 nm thick barriers (shown in black). The device is pumped from the bottom (red arrow) and emits in the same direction (shown via the red beam). The ITO thin film and Ag cladding serve as the bottom and top electrodes respectively, across which voltage is applied to the device (b) FIB cross-section image of a representative device with false color and constituent materials labeled (Reprinted from Ref. [37]).

thin film of ITO (∼20 nm) was deposited on top of this dielectric layer to serve as the bottom electrode. Although ITO is transparent at the NIR wavelengths of the nanolaser emission, it is still optically lossy and therefore, the film was chosen to be as thin as possible. Figure 2.1(b) is a cross-sectional focused ion beam (FIB) image post-completion of all fabrication steps depicting a representative device with a gain radius of 455 nm.

The photoluminescence (PL) of the nanocavities was then characterized at room temperature with a micro-photoluminescence (µ-PL) setup akin to the one used in Pan et al. [24]. A Nd:YAG laser operating at 1064 nm was used to optically pump the devices. The spectral features for a device of gain radius 465 nm are illustrated in Fig. 2 (a) and (b), clearly establishing the coherent nature of emission from the nanocavity. Firstly, the spectral evolution in Fig. 2.2(a) shows the emergence of a narrow peak at 1478 nm that dominates all other peaks as the peak pump intensity is increased. Secondly, and providing stronger evidence for lasing, the linear light-out vs. light-in (LL) curve portrayed in Fig. 2.2(b) exhibits a clear kink which signifies

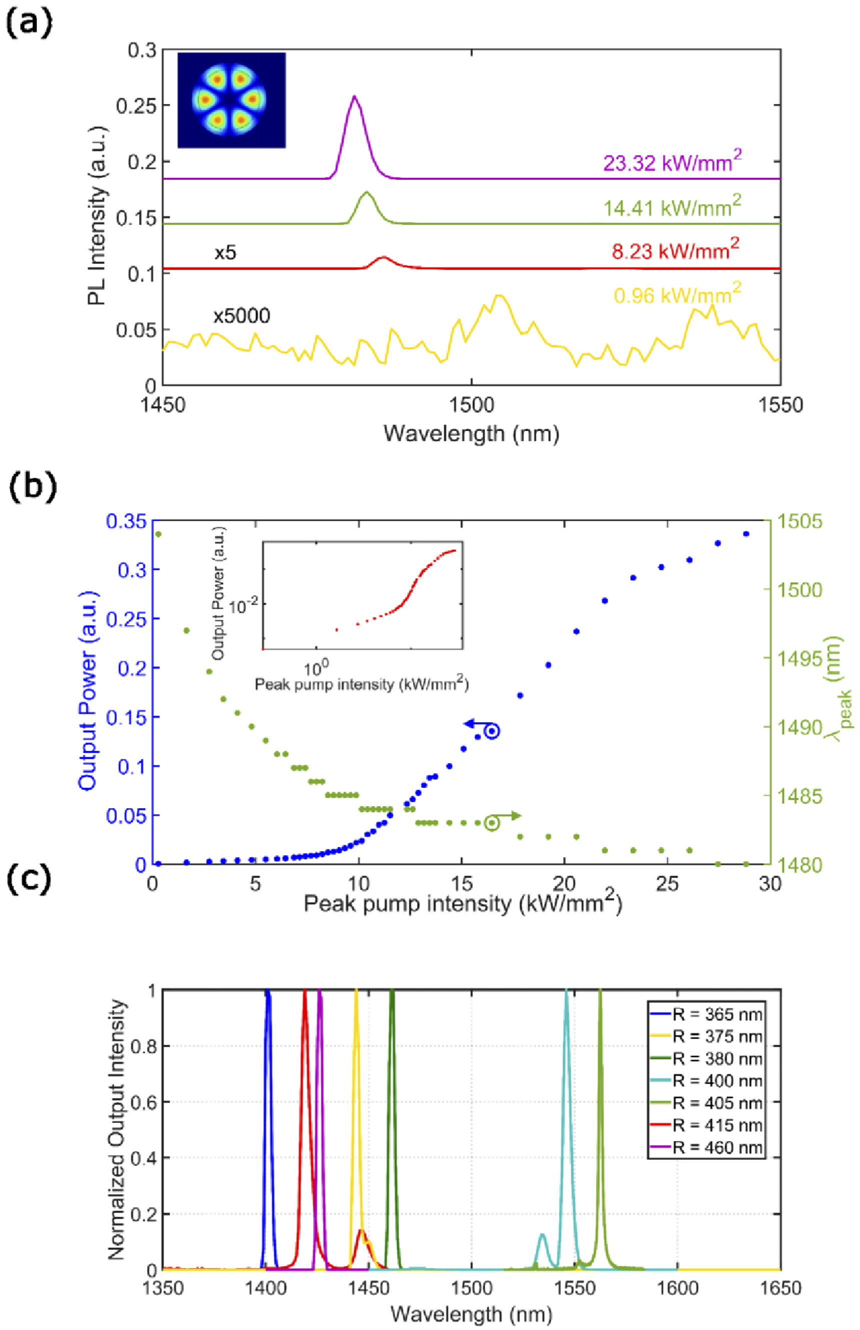

Figure 2.2: (a) Spectral evolution showing emergence of a narrow peak at 1478 nm with increased peak pump intensity. The lowest two spectral curves (red and yellow) are multiplied by a constant for easier distinguishability. Inset: Simulated modal profile of whispering gallery mode (M=3) postulated to be the lasing mode. (b) Linear LL curve (blue) illustrating onset of lasing and peak wavelength of emission (green). Inset: The same data plotted on a log-log scale showing S-shaped curve and kink. (c) Normalized spectra showing geometry-based tuning of the emission wavelength by varying the radius of the nanocavity pillar during the design stage (Reprinted from Ref. [37]).

the lasing onset; the log-log plot of the same data in the inset depicts the S-shaped curve that is conventionally associated with lasing in nanolasers [24, 50–52]. Eigenmode simulations of the cavity suggest that the lasing mode is a whispering gallery mode (M=3) as depicted in the inset of Fig. 2.2(a).

In Fig. 2.2(b), the peak emission wavelength - λ_{peak} – is also plotted alongside the LL curve. As clearly observed, significant alterations in the peak wavelength (specifically, blue-shifts) can be induced via increasing pump powers. Although the electric field-based method presented in this chapter in no way supersedes the tuning possible with varying pump powers, the former can be more advantageous in certain scenarios. Firstly, an external field method is applicable regardless of whether the device is above or below threshold. In contrast, the blue-shift incurred via increasing the pump is mainly viable for devices operating below threshold. Secondly, and most importantly, the electric field method provides an independent manner to control the emission without having to alter the pump properties. This becomes especially relevant if a single pump is pumping several nanolasers and the goal is to tune the emission of only one of the emitters. In this scenario, by applying an electric field exclusively to the device of interest while maintaining a constant pump rate, the other emitters are left unperturbed by the tuning process.

A nanolaser's emission wavelength can also be tuned according to the size of the cavity as it modifies the cavity modes supported within the gain-bandwidth window ($\sim$1.3-1.6 µm for InGaAsP MQWs). Since cavity modes can vary greatly in their resonant wavelengths, Q's and energy confinement factors, by designing and fabricating nanocavities with varying radii, the emission wavelength of our nanolasers can be coarsely but widely tuned in a static manner as illustrated in Figure 2.2(c). More interestingly, due to the ultrasmall cavity volume, it is possible to tune the lasing wavelength by substantial amounts with relatively small alterations in the gain radius. For instance, as the radius of the gain is varied from 365 to 380 nm, the emission wavelength can be tuned from 1401 to 1461 nm – a range of 60 nm. Spectra from another sample are also shown on the far right of Fig. 2.2(c) for radii of 400 and 405 nm. Although the fabrication procedures used for the two samples shown in Fig. 2.2(c) differed slightly, their spectra are plotted together to demonstrate the possibility of extending the lasing wavelength range to cover telecom bands from the E all the way up to the C band. It is important to emphasize here that the lasing mode is determined not just by the values of its Q and energy confinement factor, but also its proximity to the peak of the modal gain spectrum. Thus, similar to other studies where either the material composition is varied [30,31,46,47] or the cavity is physically altered [32,33,48], varying the radii of metal-clad nanolasers in the design phase itself provides a static or irreversible method of tuning the wavelength.

2.3 Dynamical experimental results

2.3.1 Dynamic and real-time fine wavelength tuning

In order to tune the nanolaser wavelength in real-time, an external electric field was applied perpendicular to the MQWs as depicted in Fig. 2.1(a). A Cu substrate connected to the Ag-metal cladding was chosen as one electrode while the ITO thin-film functioned as the other. Although not depicted in the device schematic in Fig. 2.1(a), this Cu electrode is the substrate to which the nanolasers, which are covered with Ag cladding, are bonded using a conductive silver epoxy; additional details about the bonding process can be found in [24,26]. A voltage source (Keithley 2400) was then used to apply the voltage across the device while it was optically pumped at an input optical intensity of $\sim 2{*}P_{th}$, where P_{th} denotes the pump intensity at the device's lasing threshold. The nanolaser's emission spectra were subsequently recorded with a monochromator. Figure 2.3(a) illustrates the effect of applying varying amounts of DC voltage on the lasing spectra of the nanolaser device for which the PL characterization is shown in Fig. 2.2(a) and (b). To provide better intuition, values of the electric field are reported as voltage instead. From Fig. 2.3(a), it can be clearly observed that with increasing voltage, the nanolaser spectra are affected in two ways. First, the output intensity of the emitted light decreases monotonically until the emission is almost completely suppressed at the highest applied voltage of 8.8 V. Secondly, the emission wavelength redshifts, also monotonically, with increasing voltage. It is important to note that both modifications to the spectra are reversible in nature, as depicted in the inset of Fig. 2.3(a). This means that, although applying voltage to an unbiased nanolaser (shown as blue, solid line) attenuates and red-shifts its spectrum (red, dashed line), the spectrum would revert back to the original behavior if it were to be measured again without any external field(orange, solid line with round markers). This reversible nature of the alterations is not shown in the main figure of 2.3(a) as the device was pushed beyond the reversible voltage limit (in this case, 8.8 V) and as a result, the ITO thin-film degraded.

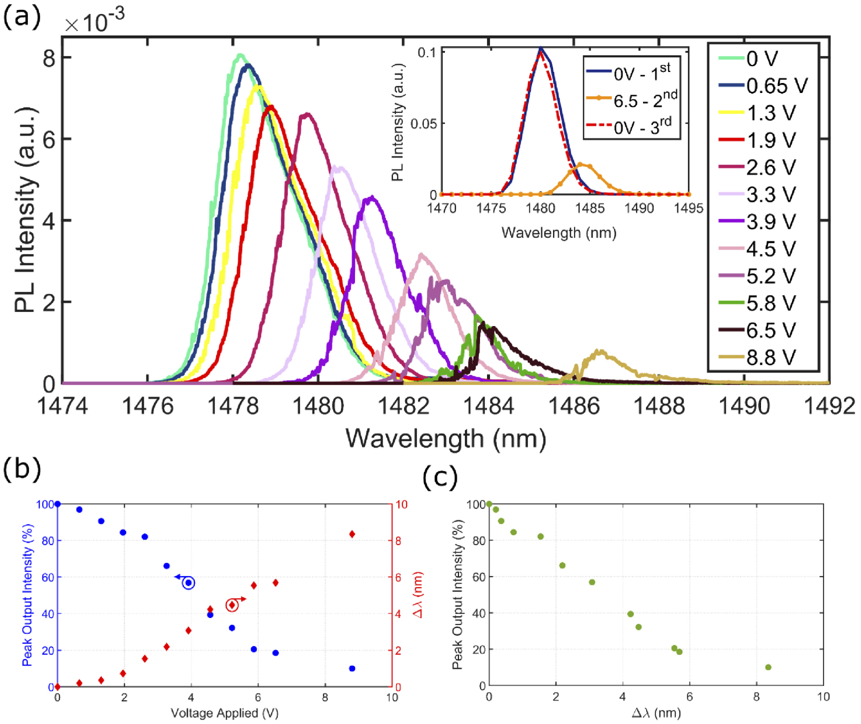

Figure 2.3: (a) Real-time dynamic tuning of lasing wavelength by applying DC electric field/voltage across the device while pumping optically. Inset: Different set of spectra from the same device confirming reversible nature of the external E-field technique (b) Peak output intensity percentage (blue circles) and tuning range in peak wavelength - $\Delta\lambda$ (red diamonds) – plotted as a function of the voltage applied to the device. The intensity can be attenuated by up to $\sim$89% and the wavelength can be red shifted by $\sim$8.35 nm at maximum when $\sim$8.8 V is applied across the device. (c) The intensity attenuation and wavelength detuning from (b) plotted together. The detuning point at which the intensity falls to 50% was determined to be at $\sim$3.7 nm via a linear fit (Reprinted from Ref. [37]).

To better quantify these effects induced by the external E-field, the nanolaser's peak output intensity, P, for each applied voltage is plotted in Fig. 2.3(b) as a percentage of P_0, the peak intensity in the absence of the E-field/voltage. A monotonic drop in the peak output intensity can be observed with the attenuation as high as $\sim$89% at the highest E-field/voltage value. Similarly, the alteration of the peak wavelength, $\Delta\lambda$, plotted on the right axis of Fig. 2.3(b) is also significant and exhibits a redshift of around 8.35 nm at maximum voltage. It is important to emphasize here that with the application of an external E-field/voltage, much finer tuning is afforded compared to the case of geometry-based tuning (Fig. 2.2(c)). A tuning sensitivity, defined as $\Delta\lambda/\Delta\mathrm{V}$, of $\sim$1.01 nm/V is found via a linear fit to the wavelength data shown in Figure 2.3(b). This corresponds to a change of close to half the laser linewidth per volt, where the linewidth is the one considered in the absence of electric field ($\sim$2.16 nm). Additionally, a peak wavelength-tuning step of smaller than 150 pm can be achieved with only a slight increment in the applied voltage ($\sim$0.65 V). This fine control also extends to the output intensity which can be attenuated by lower than $\sim$2% as the voltage is varied. Such precise tuning of the lasing peak wavelength coupled with the real-time, reversible nature of the alterations can prove to be invaluable for applications such as on-chip optical communications with WDM [4]. In addition, since the intensity attenuation and wavelength detuning are synchronous events, a direct correlation between the two is illustrated in Figure 2.3(c). It can be observed from this plot that the detuning point at which the peak intensity falls to 50% of its zero-field value (in other words, when it decreases by 3 dB) is at $\sim$3.7 nm, determined via a linear fit to the data.

2.3.2 Intensity modulation

For practical applications, high-speed modulation of nanolasers is desirable and in some cases such as for communication purposes, even imperative. To demonstrate the high-speed modulation capability of our devices under an external E-field, a small-signal modulation experiment was carried out where the nanolaser was pumped optically while an AC electric field

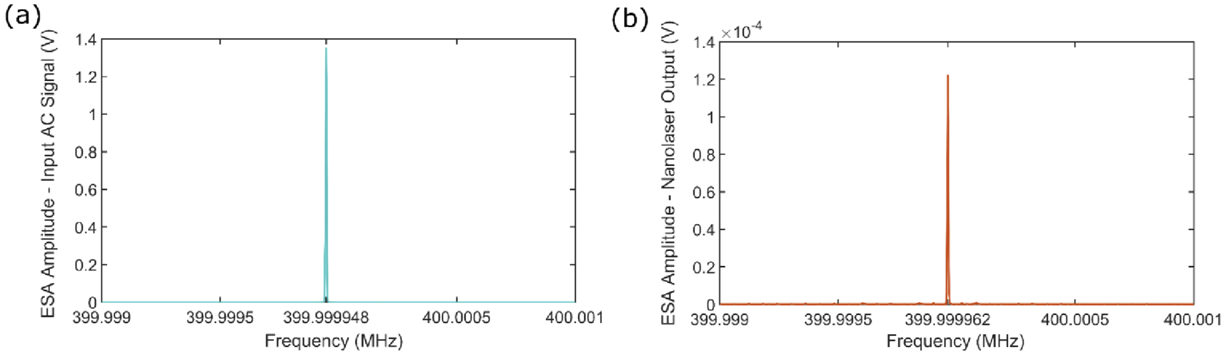

Figure 2.4: (a) 400 MHz AC sinusoidal waveform sourced from a high-speed function generator and measured via an ESA. The V_{RMS} of the signal is $\sim$1.35 V (corresponding to a peak voltage of $V_{peak} \sim 1.91$ V). (b) The nanolaser output emission when subjected to the input signal shown in (a) measured via a photodetector connected to an ESA. The amplitude measured is four orders of magnitude lower than the input AC signal. The span of both windows is 2 kHz (Reprinted from Ref. [37]).

was applied across the device's contacts via a function generator (Keysight N9181A). This input sine wave voltage was purely an AC signal with no DC components and was measured via an electrical spectrum analyzer (ESA, Keysight N9181A). The V_{RMS} of the input sine wave was confirmed to be $\sim$1.35 V (corresponding to a peak voltage of $V_{peak} \sim 1.9$ V) with a frequency of $\sim$400 MHz. A peak registered on the ESA at the exact frequency and amplitude of the input waveform is depicted in Fig. 2.4(a). Emission from the nanolaser was collected using a low-noise, high-gain APD (Thorlabs APD430C) which was then connected to the same ESA. If the device emission follows the AC signal of the voltage source, a peak would be registered in the ESA at the exact frequency of the AC input signal shown in Fig. 2.4(a). Figure 2.4(b) illustrates the result of applying the 400 MHz sinusoidal AC voltage signal to the nanolaser which registers a clear AC signal amplitude on the ESA at $\sim$400 MHz. This result confirms that our nanolaser can be modulated by an AC signal of up to 400 MHz via the external E-field technique.

Theoretically, emission alterations of nanolasers based on electronic effects can reach high speeds up to the THz regime [3]. In practice, for example in our study, further demonstrations at higher modulation speeds were impeded by the response of the APD which had a 3-dB bandwidth of 400 MHz. Additionally, the measurement error increases as the frequency is increased due to the ohmic contacts deposited on the nanolaser which are not ideal for high-speed measurements. Consequentially, only the response at the highest measurable frequency of 400 MHz is demonstrated as a proof-of-concept for high-speed modulation via the electric-field technique. Modulation at a speed of 400 MHz also confirms that the modulation mechanism is due to electronic instead of thermal effects since the latter would have limited the modulation speed to only a few MHz at most [53]. Future efforts to attain high speeds in the GHz regime and beyond would not only involve employing a detector with much higher bandwidths but would also require altering the electrode design in order to minimize measurement error and realize planarized contacts more appropriate for handling high-speed signals. Such planarized contacts can help significantly reduce the electrical losses between the source and the nanolaser which are largely responsible for the orders of magnitude difference between the input signal and device output response seen in Fig. 2.4(a) and (b) respectively. Performing the experiment at cryogenic temperatures is another manner in which the nanolaser output levels can be increased as the high optical losses incurred by the metallic cladding are lower at these temperatures.

2.4 Discussion

We believe that the mechanism behind both the red-shift in emission wavelength and attenuation in intensity is the QCSE, the quantum equivalent of the Franz-Keldysh effect [3]. According to this effect, two separate bandgap modifications occur when a field is applied to a quantum well. First, the electron and hole wavefunctions move in opposite directions relative to each other. This, in turn, reduces the radiative recombination probability and hence, the optical power being emitted. The second consequence of QCSE is the lowering of the bound state energies themselves, which effectively reduces the transition energy (or bandgap) and hence, results in a shift to lower frequencies (i.e., longer wavelengths).

To theoretically probe whether the experimental observations are indeed based on QCSE, semiconductor device analyzing tool SILVACO is used to simulate the effect of an external electric field on a representative nanolaser structure. In the 2-D simulations that are performed, the only pair of bound states that exist for both electrons and holes in this material structure is considered [54]. Additionally, the effect of light holes is not accounted for in the analysis for the sake of simplicity. The carrier mobility is modeled using a parallel electric-field dependent model while for recombination, spontaneous, Auger and band-band transitions are all considered. The bound states and wavefunctions for each of the 9 quantum wells comprising the InGaAsP gain medium are then solved for using the Schrodinger equation as varying voltages are applied to the device. Upon visualizing the results, it is observed that both the bound state energies and the wavefunctions shift during the application of an electric field in the form of voltage. In order to concretely quantify the changes induced, both the bandgap derived from the bound state energies and the wavefunction overlap are used to calculate the material gain spectrum for each of the InGaAsP quantum wells following the procedure outlined in [54]. Finally, the optical mode overlap with the wells is accounted for when calculating the modal gain spectrum for the entire MQW structure for each voltage value [55]. Figure 2.5(a) depicts the effect on the modal gain curves for a few of the representative voltage values applied to the 2-D nanolaser structure. It can be clearly observed that as the applied voltage increases, the peak of the gain spectra reduces in magnitude and red-shifts in wavelength.

In order to compare the simulated trends with the experimental ones, the change in the peak modal gain wavelength ($\Delta\lambda$) and the percentage alteration in peak modal gain amplitude are plotted with the experimental results in Fig. 2.5(b) and (c), respectively. For both the simulated quantities, the case without an E-field (zero voltage) serves as the initial reference point. The comparison reveals that while the output intensity for both experiment and simulation matched closely (Fig. 2.5(b)), the amount of tuning in the peak wavelength was higher in simulation than in experiment (Fig. 2.5(c)). This slight mismatch is expected due to several reasons, the first of which is that the two quantities that are compared – modal gain and emission intensity –

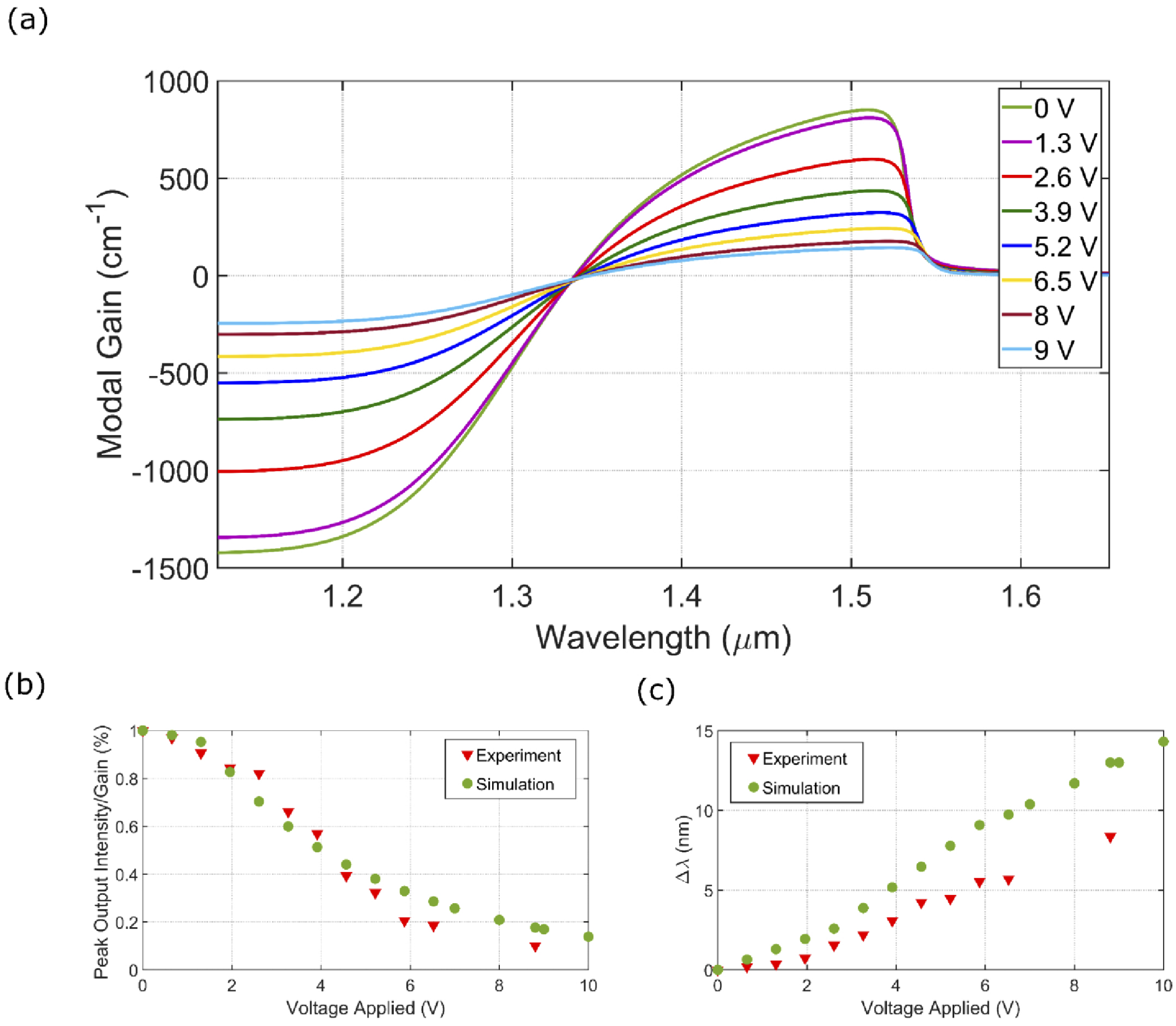

Figure 2.5: (a) Numerically calculated modal gain spectra of InGaAsP MQW gain medium comprising of 9 quantum wells. The bound state energies and carrier wavefunctions are solved using 2-D SILVACO simulations. The simulations and experiments are compared in (b) where peak modal gain (green circles) is compared to experimental emission peak intensity (red triangles) and (c) where the shift in the peak modal gain (green circles) is compared to that in the experimental peak lasing wavelength (red diamonds), $\Delta\lambda$. The trend of the experimental results matches that of the simulations but the two are not identical and not expected to be (especially for the wavelength) since any proportionality constants for the gain-intensity relationship are not considered here. Moreover, the presence of a small amount of leakage current in the experiment is also not accounted for in the 2-D simulation (Reprinted from Ref. [37]).

are related but not identical to one another. Furthermore, leakage current through the material was observed during experiments. This current arose from fabrication imperfections during the deposition of the ITO thin films used and was not accounted for in the numerical simulations, thus making it another likely reason behind the slight deviation between experiment and simulation. It is also possible that not taking light holes into account for the simulation led to an overestimation of the wavelength tuning. Finally, another cause could lie in the fact that simulations were performed in 2-D and therefore, may not be able to fully reproduce the experimental scenario. Despite the differences, the similarities between experiment and simulation build confidence that QCSE is the underlying mechanism behind the observed device behaviors.

Another interesting observation worth mentioning is the evolution of the linewidth of the emission peak that is shown in Fig. 2.3(a). It was found that the linewidth exhibits an initial narrowing as the voltage increases (till about 3.9 V), followed by a period of near constancy (4.5 V to 5.2 V), a subsequent sudden and drastic narrowing at 5.8 V and finally, broadening starting at 6.5 V. Some past studies suggest that both linewidth narrowing as well as broadening have been observed based on the QCSE. Whereas the former can be demonstrated in cases where exciton states couple less efficiently to defect-charge fluctuations [56], the latter can be a result of field-induced carrier tunneling [57]. It is possible that a combination of such mechanisms is responsible for the linewidth behavior of our device. Although a detailed exploration of this phenomenon lies beyond the scope of this study, it is an important effect worth analyzing in a future work.

Therefore, despite the presence of a small amount of leakage current, given the high-speed modulation result of Fig. 2.4(b), the emission alterations reported in this study are not believed to be caused by thermal tuning. Though applying heat to the gain material can have a similar effect of both attenuating the intensity and red-shifting the emission wavelength, heat-based modifications to the bandgap cannot occur at speeds exceeding a few MHz [53].

2.5 Conclusion

The real-time wavelength tuning and intensity modulation of metal-clad nanolasers using an external electric field are presented in this chapter. While most demonstrations of tuning for nanoscale sources in the literature are based on geometry-based, irreversible tuning, having real-time dynamic control is much more advantageous for on-chip and other applications. In this segment of the thesis, we demonstrated real-time, reversible spectral tuning and high-speed intensity modulation of a metallo-dielectric nanolaser. The emission wavelength can be tuned by up to 8.35 nm with a tuning sensitivity, defined as $\Delta\lambda/\Delta V$, of $\sim$1.01 nm/V. Additionally, the emission intensity can be attenuated by as much as $\sim$89% and this alteration can be modulated up to 400 MHz, only limited by the detector's bandwidth used for the study. Simulations suggest that QCSE accounts for the underlying bandgap modifications, inducing a shift in the carrier wavefunctions as well as lowering the bound state energies. Although some newer studies published during the preparation of this work have reported similar electric field-based changes in nanoribbon lasers [42], the nanolasers shown in this chapter are the first telecom band demonstration of dynamical tuning/modulation based on an external electric field. Future work on demonstrating modulation in the GHz regime and with continuous-wave electrically pumped devices operating at room temperature will bring us a step closer to realizing potential nanolaser applications in various areas such as photonic integrated circuits, virtual/augmented reality devices, lidar systems and imaging/sensing devices.

2.6 Acknowledgement

Chapter 2, in full, is a reprint of the material as it appears in S.S. Deka, S.H. Pan, S. Jiang, A. El Amili, F. Vallini, Q. Gu, and Y. Fainman "Real-Time Dynamic Wavelength Tuning and Intensity Modulation of Metal-Clad Nanolasers," *Optics Express*, Vol. 28, Issue 19, pp. 27346-27357, 2020. The dissertation author was the primary investigator and author of this

publication.

Chapter 3

Coupling in a dual metallo-dielectric nanolaser system

3.1 Introduction

Usually, shrinking the size of the resonator in all three dimensions leads to a spatial spreading of the optical mode beyond the resonator's physical boundaries which induces an increase in optical loss and threshold. However, as we discussed in Chapter 2, metallo-dielectric nanolasers provide unique advantages making them suitable for subwavelength operation. Specifically, the metal cladding in these types of sources helps confine the optical mode to the high index active core thereby increasing the mode-gain overlap while the dielectric shield pushes the electromagnetic mode away from the metal walls, thus reducing the mode-metal overlap and hence the Joule loss. Additionally, the metal should also aid in isolating the electromagnetic field inside each resonator from the surrounding environment. Whether the isolation provided can prevent cross-talk between optical components for purposes of dense integration on chip, however, is yet to be explored to the best of our knowledge.

The observation of coupling between non-metal based optical cavities when placed in proximity of each other has been widely reported in a host of systems such as photonic-crystal nanocavities [41, 58, 59], photonic molecule microdisk lasers [60–64], microring lasers [65, 66], ridge lasers [67] and porous silicon based microcavities [68]. Though coupling can rely on varying types of physics to occur, the most commonly reported form is based on evanescent interaction between the electromagnetic fields of the individual resonators which results in a characteristic splitting of the observed optical modes in both frequency and loss [41, 60, 63, 64, 69]. This bifurcation arises due to the presence of bonding and anti-bonding states in the coupled system, the latter of which generally exhibits lower losses and hence, becomes the lasing mode. These supermodes can then give rise to new functionalities, for instance, such as possible use in memory due to bistable behavior exhibited by the anti-bonding mode [41, 64]. However, for nanoscale devices, if the primary goal is to achieve high packing density for on-chip design, it is essential that the individual cavities comprising the coupled system can operate independently from one another. This would allow one laser to be operated or modulated without interfering in its neighbor's emission behavior. Since metal-clad nanolasers are ideally suited for this type of dense integration due to their subwavelength and nanoscale dimensions, whether coupling is induced when two such devices are designed near one another needs to be investigated.

In this chapter, we report the effect of gradually reducing the separation between two metallo-dielectric nanolasers using three-dimensional finite-element method (FEM) simulations. Contrary to expectations that the metal should inhibit coupling, a splitting of the optical modes in both the resonance wavelength, λ, and quality factor, Q, is observed for the coupled metallo-dielectric nanolaser system akin to what is reported in coupled microcavities [60, 66]. The split is caused by the creation of bonding and anti-bonding states as the distance between the dielectric shields of the nanolasers is decreased. Since the two nanoresonators share the same metal cladding, it is not possible to engineer any changes in the metal coating for one without affecting the other. Therefore, two methods are presented, one where slight detuning of one of the cavity resonances can prevent the phenomenon of coupling from occurring and another where designing the cavities to be slightly larger in size inhibits coupling as well. Both techniques help preserve the independence of the two nanolasers.

3.2 Observation of coupling

Figure 3.1 shows a representative schematic of the dual cavity system to be simulated. The gain medium comprises of bulk InGaAsP modeled with a height of $h_{InGaAsP}$ = 300 nm, radius $r_{InGaAsP}$ = 225 nm and permittivity of ε_{gain} = 11.56 [20]. Each gain was conformally cladded with SiO_2 of height h_{SiO2} = 100 nm, selected to minimize the gain threshold of the nanolaser. Additionally, an airgap, of h_{Air} = 400 nm height, below the gain layer was designed to provide optimal mode confinement. Finally, the cavities were covered with a 1 μm layer of Ag. The permittivities for the SiO_2, air and Ag material layers were taken to be $\varepsilon_{dielectric}$ = 2.16, ε_{air} =1 and ε_{silver} = -130 - 3i [70], respectively, with the values chosen considering the eigenmode wavelength supported by the nanocavity design (around 1.55 μm) and assuming room temperature operation.

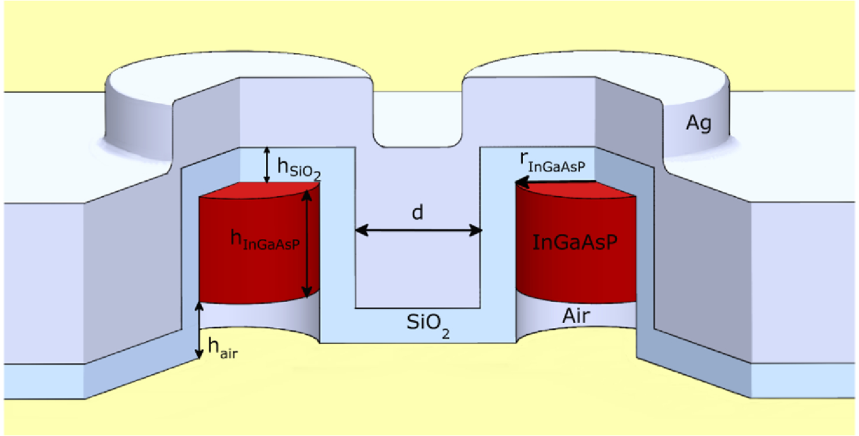

Figure 3.1: Device schematic of the dual-cavity system with the constituent materials labeled. The heights of the gain, SiO_2 cladding, airgap, and radius of the gain are represented by $h_{InGaAsP}$, h_{SiO2}, h_{Air} and $r_{InGaAsP}$ respectively. The distance, *d*, between the dielectric shields is the parameter changed during a parametric sweep to probe the characteristics of the modes. (Reprinted from Ref. [15]).

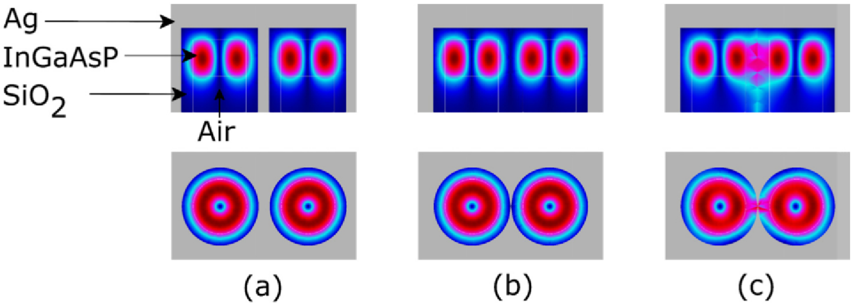

Figure 3.2: Electric field intensity profile across the side (top row) and top (bottom row) cross sections of the dual-cavity nanolaser system. (a) Distance between the dielectric shields is 90 nm and the system supports two identical modes. (b) Shields are now in contact, and an anti-bonding supermode is created with strong confinement of the electromagnetic mode to the gain medium of each resonator. (c) New bonding mode is created for the same separation as in (b), but the mode is poorly confined to the gain regions for this state. (Reprinted from Ref. [15]).

To study the effect of reducing the separation, *d*, between the dielectric shields of the two cavities comprising the dual system, we first consider two cases - when the cavities are far apart at 90 nm and when they are in contact at 0 nm. For each separation distance, the electric field intensity across a two-dimensional side and top cross-section of the gain was recorded. Figure 3.2 illustrates the side and top profiles of the magnitude of the electric field of the TE_{011} mode supported by each nanocavity for the two separations mentioned. For the case of $d = 90$ nm, the metal between the two cavities prevents the electromagnetic fields inside each resonator from interacting with one another. In other words, the evanescent field from each cavity is allowed adequate space to decay exponentially due to damping by the metal, thereby producing little to no interaction of fields in the metallic region. This isolation can be clearly seen in Fig. 3.2(a) where the two identically-sized cavities support the same resonant modes but there is no interaction between the two TE_{011} modes. However, for smaller *d* and taking the extreme case of when $d = 0$ nm as in Figs. 3.2(b) and (c), two new optical modes are observed due to increased evanescent coupling between the two cavities. The bonding state, shown in Fig. 3.2(c), demonstrates poor confinement of the mode to the gain media of the two resonators with a significant portion of the field interaction seen to be occurring in the dielectric shields. In contrast, the anti-bonding state in Fig. 3.2(b) still shows the mode to be strongly confined to the gain medium of each resonator.

In fact, the mode profile of the anti-bonding state is nearly identical in appearance to when the cavities support independent modes of their own when designed far apart as seen in Figs. 3.2(b) and (a) respectively.

To further elucidate the impact of coupling between the two cavities, d was varied in an eigenfrequency solver module of COMSOL Multiphysics. The eigenmode wavelength, λ, and quality factor, Q for the modes supported by the system are calculated for each intercavity distance. As seen in Fig. **??**(a), the λs for the two modes supported by the system are nearly identical to each other when the two cavities are placed far enough apart; the same can be said for the Q shown in Fig. **??**(b). Therefore, only intercavity spacings up to 60 nm are plotted for better contrast. In fact, this behavior is expected since the modes supported in these high-separation designs are a pair of isolated cavity modes with the mode profile of each identical to the illustration shown in Fig. 3.2(a). At these intercavity separations, the two cavities are essentially independent of one another despite supporting almost the same resonant frequencies. As the nanocavities are brought closer together, two new states emerge – an anti-bonding and bonding state as depicted in Figs. 3.2(b) and (c), respectively. The cavity resonant wavelength and quality factor for the bonding state are higher and lower, respectively, than those for the individually isolated cavity mode. Conversely, for the anti-bonding mode, the λ and Q are lower and higher than the same parameters of an isolated cavity mode. Consequently, a split, which can be visibly discerned at a separation as high as around 50 nm in Fig. **??**, arises in these two parameters of the new supermodes as the intercavity separation is decreased. Coupling is most pronounced when the SiO_2 shields of the cavities contact each other at $d = 0$ nm. Hence, the difference in λ and Q between the bonding and anti-bonding eigenmodes is maximum at this point with values of $\Delta\lambda =$ 14.6 nm and $\Delta Q = 1347$.

Since the simulated nanocavities are purposed for lasing, observing the change in parameters such as the λ and Q do not provide any helpful insight on how coupling can affect the likelihood for lasing. Instead, the gain threshold, g_{th}, is calculated with the equation:

$$g_{th} = \frac{2\pi n_g}{\lambda Q \Gamma} \tag{3.1}$$

where n_g is the group refractive index and Γ is the electromagnetic mode confinement factor [23]. Fig. 3.3(c) shows that for the bonding mode, the threshold increases exponentially as the resonators are placed closer together. Therefore, it would be difficult for the lossy bonding state to feasibly lase at the lowest intercavity separations whereas the same cannot be said for its anti-bonding counterpart due to its lower threshold. The stark contrast between the lasing tendencies of the modes is evident when for d = 0 nm, the difference in the respective gain thresholds of the supermodes is found to be Δg_{th} = 217 cm^{-1}.

The split in the resonant wavelength of emission as the cavities are designed closer together is a signature of coupling as reported for both micro- [60–64, 68] and nanoscale structures [41, 58] when the individual cavities are fabricated in proximity of one another. In fact, an exponential rise in the wavelength difference between the modes of the coupled system is observed as the separation between resonators is reduced [60, 66]. This exponential behavior can be seen in Fig. 3.3(a) for intercavity distances close to 0 nm. When placed far enough apart, however, there is no coupling between the metal-clad cavities and the modes supported in the individually isolated resonators are independent of one another as has also been observed for coupled photonic molecules [60–64, 68, 69]. Additionally, the new bonding supermodes created during coupling between cavities generally incur higher losses [60, 63, 64, 69]. Thus, the bonding mode demonstrating a lower Q and hence higher λ (due to lower energy) than its anti-bonded counterpart, as seen in Figs. 3.3(a) and (b), is in line with the expected behavior from a coupled system [71]. The only unique feature observed in the coupling between the metallo-dielectric cavities is the asymmetric splitting in both the λ and Q; coupling reported in other systems generally illustrates symmetry in the splitting [63, 71]. The asymmetry for the system presented in this work is caused by the metal cladding which gives rise to a plasmonic effect that confines one mode better to the metal than the other.

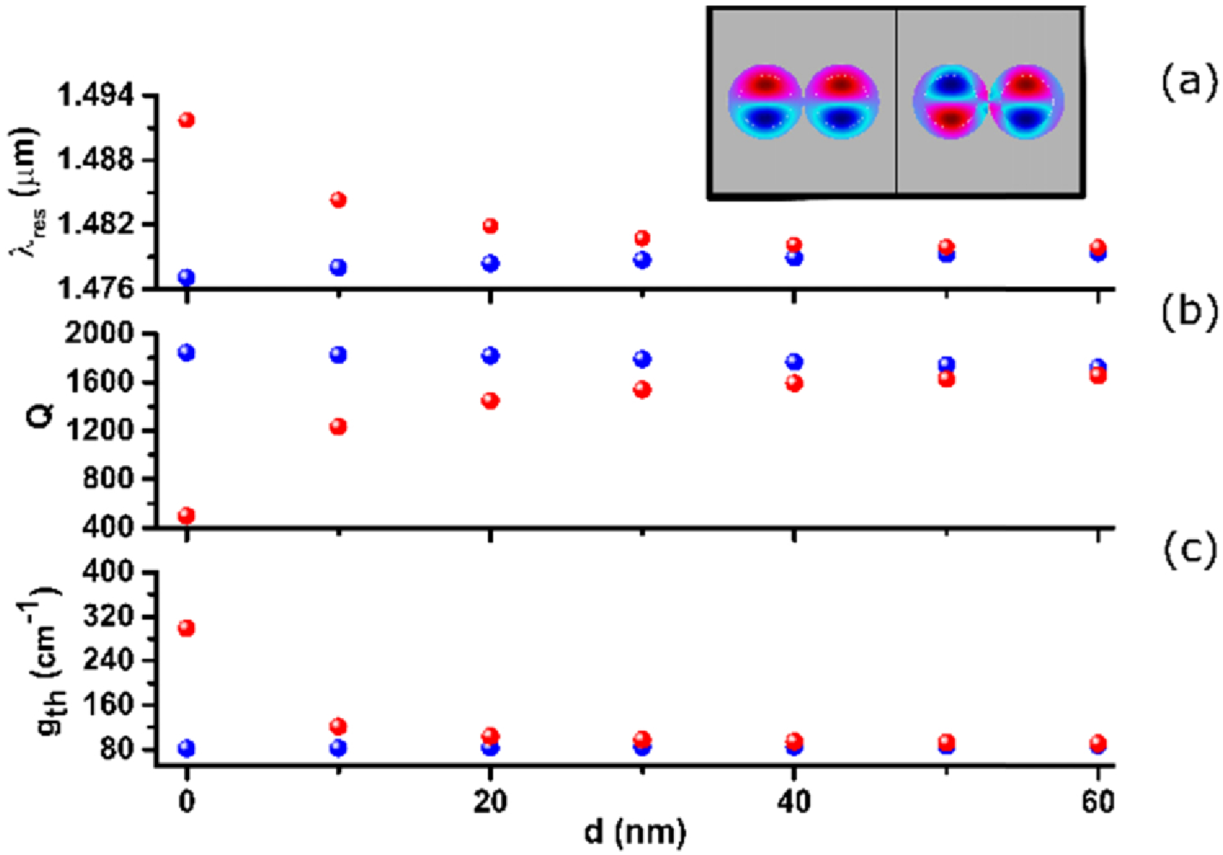

Figure 3.3: Resonance wavelengths, Q-factors, and gain thresholds for each of the two modes of the system at different intercavity separations. The red represents the bonding state, and the blue represents the anti-bonding state at lower separations. (a) Eigenmode wavelength, λ, (b) the Q-factor, and (c) the gain threshold, g_{th}. Inset: electric field distribution of the anti-bonding (left) and bonding (right) supermode. (Reprinted from Ref. [15]).

3.3 Decoupling by detuning resonances

Though coupling is generally sought after, in the case that a bifurcation of states is not desirable, methods must be introduced to control or at least mitigate the coupling between cavities. For non-metal based cavities, coupling can be reduced through various means. The region between the resonators itself, which can act as a barrier for coupling, can be altered by increasing its size, for instance, as in photonic crystal microcavities, thereby reducing the mode interaction needed for coupling [69, 72]. One cavity can also be detuned dynamically from its neighbor via thermal or carrier effects [58]. In contrast, for the nanocavities simulated in this study, the common metal shield covering both the resonators makes the above techniques less feasible to implement. Any attempt to independently control one cavity or engineer changes in its cladding is rendered futile since the changes will affect the other cavity as well via the shared metal coating.

In this scenario, one possible way to curb the evanescent field interaction outside the gain media is to detune the resonances of the cavities relative to each other. By incorporating slight changes in the physical dimensions of one of the cavities in the dual cavity system, eigenmodes for the altered cavity can be shifted far enough away to prevent any significant coupling from occurring. Figure 3.4 depicts the λ, Q and g_{th} for the two modes supported in a dual cavity system where the radius of one cavity has been designed to be 236.25 nm, exactly five percent more than that of its neighbor. Unlike in Fig. 3.3, no pronounced split in any of the three quantities is observed as the separation between the two size-mismatched cavities is decreased down to zero. The values for $\Delta\lambda$, ΔQ and Δg_{th} when the shields of the respective resonators are in contact with each other are 52.5 nm, 157 and 25.15 cm^{-1}, respectively, the latter two of which are much smaller in comparison to the previously mentioned values for these quantities for the case of two equal-sized cavities. The greater difference between the resonance wavelengths of the two modes, $\Delta\lambda$, in the size-mismatched case is due to the size detuning of one of the cavities and not due to coupling. This becomes evident when by comparing the least cavity separation of 0 nm with a larger one at 60 nm in Fig. 3.4(a), the change in $\Delta\lambda$ is only $\sim$3.3 % whereas for the case of equal-sized cavities shown in Fig. 3.3(a), the change is many times more pronounced at 2650 %. Thus, implementing a slight design change in the dimensions of one of the cavities compared to the other results in the dual system exhibiting only independent lasing modes, instead of any coupled supermodes, regardless of the distance separating the nanocavities. Therefore, size-mismatching can prevent the formation of photonic molecules by eliminating coupling and hence cross-talk between two closely spaced metallo-dielectric nanolasers.

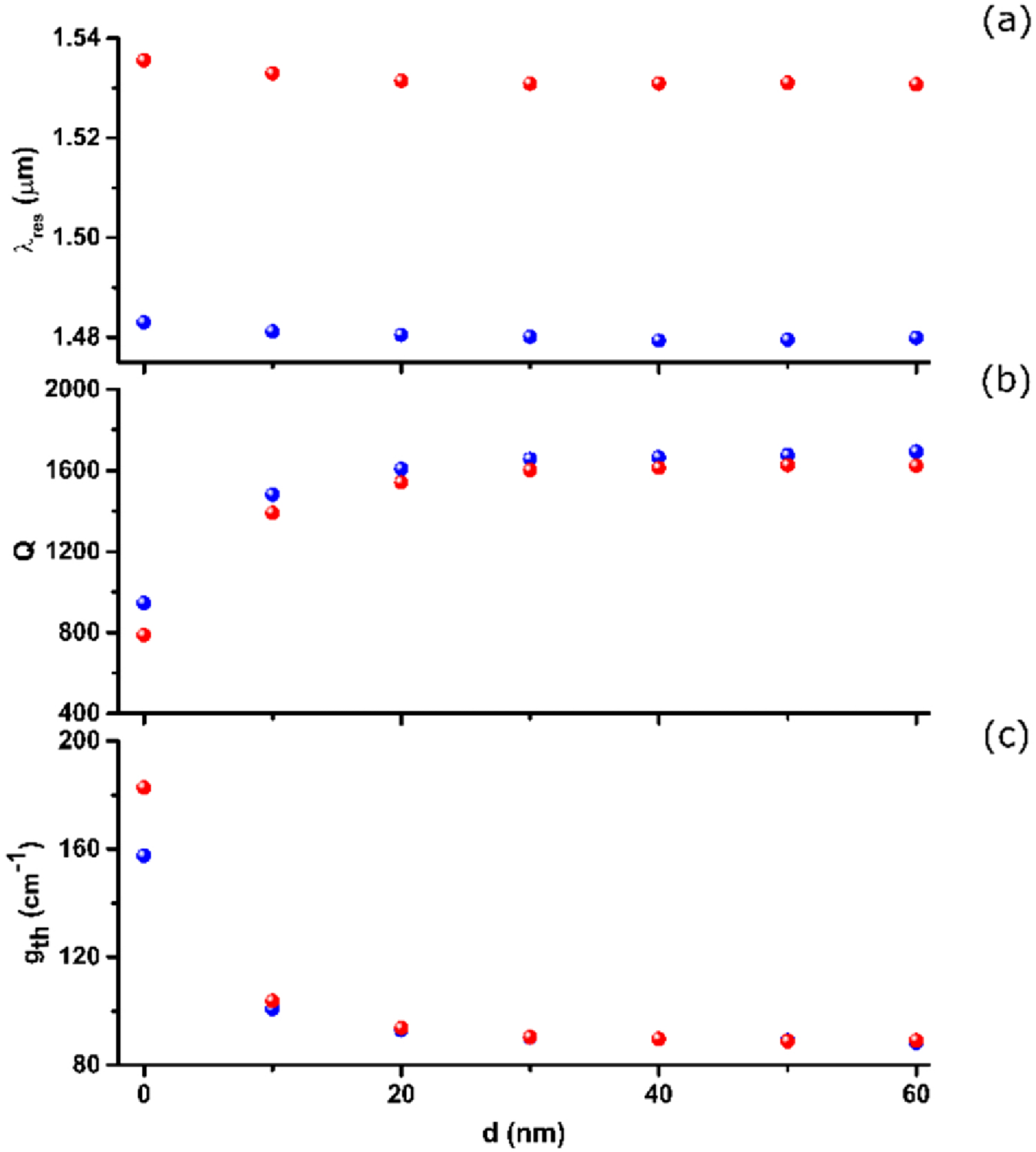

Figure 3.4: Resonance wavelengths, Q-factors, and gain thresholds for each of the two modes of the system at different intercavity separations such as in Fig. 3. The radius of one of the cavities (shown in red) is designed to be five percent larger than that of the other cavity (in blue). (a) Eigenmode wavelength, λ (b) the Q-factor and (c) gain threshold, g_{th}. (Reprinted from Ref. [15]).

3.4 Decoupling by increasing radius

An alternative method to impede coupling is to design all the resonators in the system to be larger in size. Doing so increases the order of the optical modes supported by the resonators with these higher-order modes better confined to the individual cavities than lower-order ones [71, 73]. As a result, less of the mode leaks out of the gain media even at small intercavity spacing, *d*, leading to negligible evanescent interaction of the electromagnetic fields and hence decoupling. Figure 3.5 illustrates the result of applying this technique to the dual nanolaser system in the form of the Q-factors of the modes supported by the system when the radius of each cavity is increased to 275 nm from the original 225 nm shown in Fig. 3.2. Due to the increase in the radii, more than just two modes, as is the case for the smaller-sized cavities shown in Fig. 3.4, can be observed for the enlarged-cavity system. Additionally, the Q-factors of all the modes except one stay relatively constant or increase slightly as *d* is reduced. Only one mode exhibits a higher loss (lower Q) with decreasing *d*. This mode exclusively experiences the increased loss due to coupling (due to a high overlap with the lossy metal) compared to the rest of the modes supported by the system. As the radius of the cavity is further increased, the trend that only one mode of the system demonstrates a low Q as *d* approaches 0 nm while the remainder of the cavity modes do not experience any significant change in their Q-factors, remains consistent.

Considering only this coupled mode and calculating the difference in its Q - $\Delta Q_{coupled}$ - for when the nanolasers are designed far apart (*d* = 100 nm) and when their shields are in contact (*d* = 0 nm) for different sized cavities yields the plot in Fig. 3.6. As can be seen in the schematic, with increased radius, the coupled mode exhibits reduced fluctuation in its Q despite the continual decrease in *d*. Consequently, this mode starts resembling the other modes supported in the system in that it too becomes less susceptible to losses generally experienced due to coupling. In [71], coupling between micron-sized metal/Si disks is shown to be inhibited via an observed reduction in the difference between the eigenmode wavelengths of anti-bonding and bonding modes as the

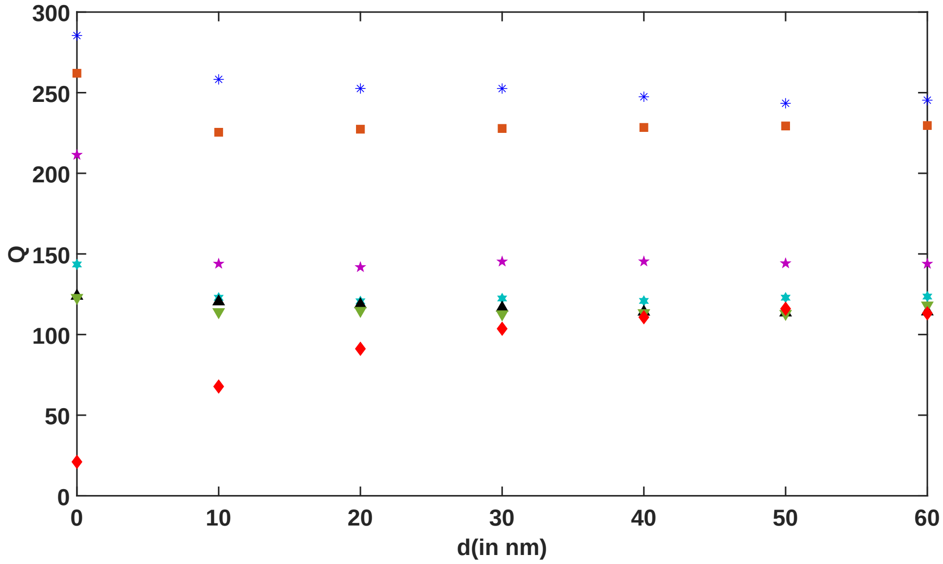

Figure 3.5: The Q-factors for the modes supported in a dual nanolaser system with cavity radius = 275 nm for different values of *d*. Only one of the modes, shown in red, experiences higher losses as *d* is decreased down to 0 nm; the Q for the rest of the cavity modes either stays constant or increases only slightly. (Reprinted from Ref. [28]).

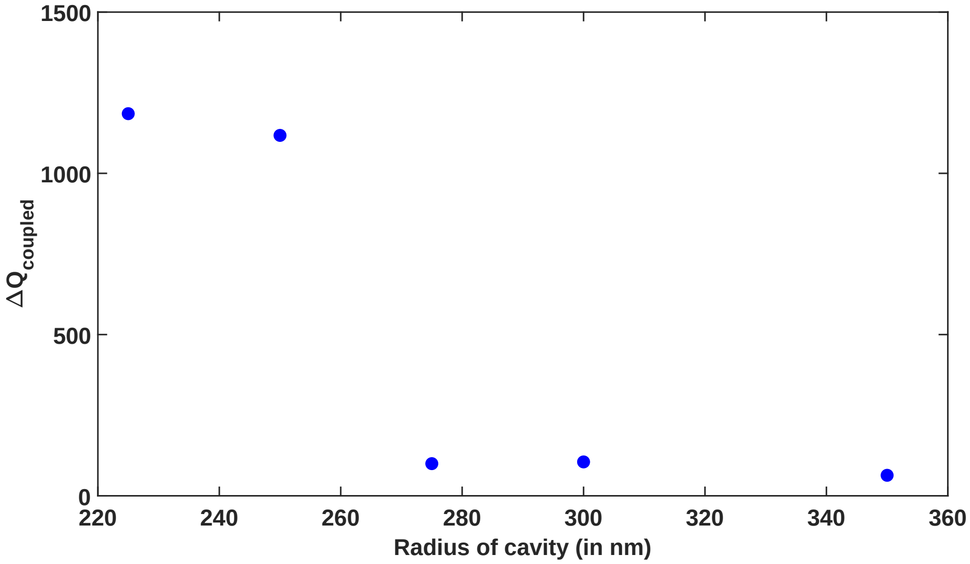

Figure 3.6: Difference in Q-factor for the coupled mode - $\Delta Q_{coupled}$ – for *d* = 100 nm and d = 0 nm for varying radii of the cavities. As radius is increased, there is less loss experienced by the mode as *d* is reduced since coupling becomes less pronounced. (Reprinted from Ref. [28]).

mode number supported by the disks is increased. Similarly, in the case of the metallo-dielectric nanolasers, the decrease in the loss incurred by the cavity modes, and especially by the one coupled mode in the system, as the cavity radius is increased to support higher order modes is also indicative of reduced coupling between the cavities. Thus, increasing the physical dimensions of all the constituent resonators of the system provides an additional means of prohibiting coupling for nanolasers which are purposed for compact on-chip integration.

3.5 Conclusion

To conclude, in this chapter, we analyzed a system of two spatially close metallo-dielectric nanolasers and demonstrated coupling upon reducing the separation between the two nanoresonators. A split observed in both the resonant wavelengths, λs, and the Q-factors of the two modes for inter-cavity separations below 50 nm is akin to bifurcations observed in coupled cavities on the micron scale. The fact that inter-cavity separations needed to observe coupling for metallo-dielectric nanolasers (<50 nm) is much smaller than the μm scale distances needed in non-metal based cavities further strengthens their viability for dense on-chip integration. The increasing difference between the wavelengths and quality factors of the two modes is caused by the creation of anti-bonding and bonding states due to evanescent electromagnetic field interaction outside the gain media of the resonators. If the primary purpose for such nanoscale light sources is dense integration on chip, then preserving the independence of each emitter is of paramount importance to allow control over one's emission behavior without interfering in that of its neighbors. To eliminate the two supermodes, a method of shifting the resonance of one of the cavities by altering its radius by five percent of that of the other cavity is presented. By doing so, albeit the resonances of the cavities were made to be dissimilar, a coupled supermode that essentially treats the system as one cavity was avoided. Such size-mismatched metal-clad nanolasers can be modulated independently without concern for crosstalk between components.

Given that even with current state-of-the-art fabrication procedures slight fluctuations from the intended size are unavoidable, even two identical cavities may produce a size mismatch and, hence, not couple. Instead, the now disparate lasing wavelengths may prove to be useful for applications such as on-chip dense wavelength division multiplexing. An alternative manner of detuning the resonances is also presented in which the radii of both cavities are designed to be slightly larger. Since larger sized cavities support higher-order modes which exhibit tighter confinement to the gain media than lower-order modes, two larger cavities demonstrate reduced coupling despite being spatially close ($d = 0$ nm) and equal to one another in dimensions.

3.6 Acknowledgement

Chapter 3, in part, is a reprint of the material as it appears in S.S. Deka, S.H. Pan, Q. Gu, Y. Fainman, and A. El Amili "Coupling in a dual metallo-dielectric nanolaser system," *Optics Letters*, Vol. 42, Issue 22, pp. 4760-4763, 2017. The dissertation author was the primary investigator and author of this publication. Chapter 3 section 3.4, in full, is a reprint of the material as it appears in S.H. Pan, S.S. Deka, A. El Amili, Q. Gu, and Y. Fainman "Nanolasers: second-order intensity correlation, direct modulation and electromagnetic isolation in array architectures," *Progress in Quantum Electronics*, Vol. 59, pp. 1-18, 2018. The dissertation author contributed to the measurements of high-speed and writing of the coupling section for this publication.

Chapter 4

Effects of High-β on Phase-Locking Stability and Tunability in Laterally Coupled Lasers

4.1 Introduction

In 3, we discussed the effects of designing two MDNLs in proximity and how it leads to near-field coupling between the two resonators despite the presence of the metal cladding. We also discovered that for applications where independent functioning of the emitters is required, the coupling can be inhibited by either detuning the resonances of the two lasers or by designing them to support higher order modes in Sections 3.3 and in 3.4, respectively. However, in most instances, coupling is a desirable phenomenon and in particular, achieving phase-locking between coupled sources has been extensively investigated owing to their potential in generating high-power and coherent optical beams valuable for applications such as LiDAR, optical communications and remote sensing [74–76]. Additionally, the ability to tune the phase difference between constituent elements in an on-chip semiconductor laser array is vital for beam forming and steering applications [77, 78]. To realize the desired phase offset of the lasers in the arrays, i.e. in-phase operation for high power emission and shifted phase operation for beam forming and scanning, establishing stable phase locking is imperative. However, such stability is challenging to achieve due to multiple factors such as mode competition, distinct time scales of photon and carrier dynamics, complex nonlinear dynamics over a wide range of physical parameters including inter-cavity distances and differences in resonator dimensions of coupled lasers, and most notably, due to the amplitude-phase coupling in semiconductor lasers quantified by the linewidth enhancement factor [79, 80]. Despite the challenges, stable in-phase locking has been demonstrated through spatial and spectral mode engineering, including evanescent coupling in topological cavities [81], non-Hermitian coupling in super-symmetry arrays [82], diffractive coupling via Talbot effect [59], global antenna coupling [83], and gain matching [84]. Achieving similar phase synchronization in laterally coupled lasers arranged in close proximity (such as the design shown in Chapter 3, although difficult, is highly desirable since it involves simpler fabrication procedures and offers denser on-chip integration compared to the other coupling schemes mentioned above. Moreover, the dynamical behavior of laterally coupled lasers can be accurately analyzed and predicted by non-complex mathematical models.

In fact, theoretical analysis of the stability in laterally coupled semiconductor lasers has been widely reported in the literature [38, 39, 85–88]. In these studies, a plethora of dynamical regimes including stable continuous-wave operation, periodic and period-doubling oscillations, chaos, bistability, and chimera states are identified via bifurcation analysis. These dynamical behaviors are obtained by either analytically or numerically solving the coupled rate equations that govern the temporal dynamics of the emitted laser field. The impact of a variety of important parameters such as current injection rate, linewidth enhancement factor, laser size differences, as well as carrier and photon lifetimes, are addressed in these analyses. However, one critical parameter consistently overlooked in the majority of the theoretical works in the literature thus far is the spontaneous emission factor β. This β factor, which was first discussed in Chapter 1, is smaller than 10^{-3}) in typical commercial laser diodes, and thus is reasonably neglected in most bifurcation studies [85–87]. As mentioned in the previous chapters however, nanolasers that exhibit intrinsically high and non-negligible β values have been demonstrated on various platforms over the past two decades [24–26, 29, 89]. A handful of studies so far have reported on the significant impact that spontaneous emission can exert on coupling behavior such as mode switching for coupled photonic crystal nanolasers [41, 59] and partial locking for mutually coupled micropillar lasers operating in the few-photon regime [90, 91]. Notably, some previous theoretical investigations have suggested that the larger damping effect induced by higher β may help suppress the instability encountered in lateral coupling schemes [39, 92]. This hypothesis as well as the rapid advances in nanolaser technology necessitate an in-depth analysis of how large values of β can contribute towards stable phase-locking operation.

In this chapter, we theoretically investigate the effects of varying β on the stability of phase locking in two laterally coupled semiconductor lasers through bifurcation analyses. With increasing β, a corresponding expansion of the stability region is observed when first considering a purely imaginary coupling coefficient, representing a system where the supermodes have identical losses. In order to assess the feasibility of such stability enhancement due to high-β in a more practical device, we also consider other important control parameters such as the pump rate and the resonance frequency detuning between the coupled lasers that can result due to fabrication imperfections. We then further extend the study by including complex coupling coefficients in order to better account for realistic scenarios where the supermodes face dissimilar losses. Increases in the phase-locking stability regions driven by increases in β are observed across variations of all the control parameters, thereby confirming that the β-driven stable phase-locking phenomenon is not merely restricted to any specific pump power level or to only negligibly small frequency detuning. Finally, by pumping the two lasers unequally, it can be shown that the steady-state phase difference between the emitters varies as a function of β, with higher values of β resulting in a wider range of relative phase tunability. Therefore, the results presented here emphasize the significance of using high-β nanolasers in phase-locked arrays which can demonstrate both high output power density as well as beam forming and steering capabilities depending on the desired application.

This chapter is organized into four sections. Section II elaborates on the theoretical model used to perform the numerical simulations. Then in Section III, the effects of varying β on the phase-locking stability is discussed in detail. To provide an intuitive understanding of the results in this section, the model is reduced to be as simple as possible initially and then sequentially increased in complexity, one additional parameter at a time. Specifically, equal pumping, an imaginary coupling coefficient and no frequency detuning are assumed while evaluating the effects of altering β in Section III-A. Then, the pump rate, frequency detuning and a complex coupling coefficient are gradually introduced into the model in Sections III-B, III-C and III-D, respectively. In Section IV, we present our results for the case of unequal pumping, demonstrating how increasing β yields a much wider range for the steady state values of the phase difference. Finally, Section V concludes the chapter.

4.2 Theory and Methods

The coupled rate equations, with β included, that govern the temporal dynamics of two laterally coupled laser cavities considered here are given by:

$$\begin{aligned}\frac{d|E_{1,2}|}{d\tau} &= (\Gamma G_N(N_{1,2}-N_0)-\frac{1}{\tau_p})\frac{|E_{1,2}|}{2} + \frac{\Gamma F_p \beta N_{1,2}}{2\tau_{rad}|E_{1,2}|^2}|E_{1,2}| \\ &\mp \kappa cos(\Delta\phi)|E_{2,1}| + \gamma sin(\Delta\phi)|E_{2,1}|\end{aligned} \tag{4.1}$$

$$\frac{d|N_{1,2}|}{d\tau} = P_{1,2} - \frac{N_{1,2}}{\tau_{nr}} - \frac{(F_p\beta+1-\beta)N_{1,2}}{\tau_{rad}} - G_N(N_{1,2}-N_0)|E_{1,2}|^2 \tag{4.2}$$

$$\frac{d\Delta\phi}{d\tau} = \frac{\alpha}{2}\Gamma G_N(N_2-N_1) + \Delta\omega \pm \kappa(\frac{|E_1|}{|E_2|}-\frac{E_2}{E_1})cos(\Delta\phi) - \gamma(\frac{|E_1|}{|E_2|}+\frac{E_2}{E_1})sin(\Delta\phi) \tag{4.3}$$

where $|E_{1,2}|$ are the amplitudes of the electric fields in cavities 1 and 2, $|E_{1,2}|^2$ are the photon densities, $N_{1,2}$ are the carrier densities and $\Delta\phi = \phi_2 - \phi_1$ is the phase difference between the electric fields in the two cavities. The definitions of the other parameters and their representative values for an InGaAsP material system that is considered in the numerical simulations, are summarized in Table 4.1. Additionally, even though the Purcell factor F_p and β are correlated, they are treated as independent from one another in this study since we are primarily interested in the trends of stability with respect to increasing values of β.

Table 4.1: Descriptions and values of the symbols used in the rate-equation simulation.

Symbol	Description	Value
α	Henry factor	4
τ_p	Photon lifetime	1.5 (ps)
τ_{rad}	Radiative carrier lifetime	2 (ns)
τ_{nr}	Nonradiative carrier lifetime	0.625 (ns)
Γ	Confinement factor	0.8
N_0	Transparent carrier density	$2 \times 10^{23}(m^{-3})$
F_p	Purcell factor	1
G_N	Differential gain	$4.28 \times 10^{-12}(m^{-3})$
$P_{1,2}$	Pump rate	10^{35} to $1.2 \times 10^{36}(m^{-3}s^{-1})$
$\Delta\omega$	Frequency detuning between two lasers $\Delta\omega = \omega_2 - \omega_1$	-2 to 2 (Thz)

Finally, the coupling between the two cavities is introduced in a phenomenological manner via a complex coupling coefficient $i\kappa + \gamma$, that includes a dispersive coupling rate κ and a dissipative coupling rate γ. The parameters κ and γ originate from the dissimilarities in effective refractive indices and losses, respectively, between the two eigenmodes – bonding and anti-bonding - supported by the coupled cavities. To be more precise, κ can be calculated from the frequency splitting between the bonding and antibonding modes (denoted by + and -) using $\kappa = \frac{1}{2}(\omega_+ - \omega_-)$, while γ can be calculated from the loss splitting as $\gamma = \frac{\omega_-}{Q_-} - \frac{\omega_+}{Q_+}$, where $Q_(+ / -)$ are the quality factors of the supermodes [41]. To generalize the effects of increasing β for any laterally coupled system, the dependence of κ and γ on either coupling geometry or material properties is neglected, and their values are chosen to be within a range that can be feasibly achieved in coupled laser platforms [43, 92]. Although both the sign and the values of κ and γ can be precisely controlled through altering the coupling geometry and material composition [69, 72, 93, 94], such as changing the size of the nanoholes in the center barrier for coupled photonic crystal lasers, we first assume $\gamma = 0$ and $\kappa > 0$ for the simplicity of understanding the model and results presented here. Once we obtain enough initial insight into how stability depends on β and the other control parameters, we extend the study to consider a complex coupling coefficient with $\gamma neq 0$ and the coupling rates demonstrating both positive and negative signs. This allows the model to reflect scenarios where either of the supermodes can exhibit higher eigenfrequency and/or higher losses. In other words, in addition to the coupling geometry and material composition, the sign and values of κ and γ also depend on the comparative values of the eigenfrequencies and losses of the two supermodes.

4.3 Phase-locking stability vs. β

In this study, the stable phase locking regions for the two laterally coupled lasers are identified as functions of β, pump rate P and the frequency detuning $\Delta\omega$ using the bifurcation software XPPAUT, which contains the numerical continuation package AUTO [95]. The electric fields and carrier densities in (1) are normalized to reduce the simulation time. The time scale of the rate equations is also normalized with respect to the photon lifetime τ_p (see Appendix). Additionally, a small signal analysis is performed to provide physical insight into the results (see Appendix for details). In this work, only three types of bifurcation points are discussed – pitchfork, saddle-node (SN) and Hopf bifurcations – since the stable regions are found to be exclusively bounded by these three types of bifurcations. It is important to note here that although the numerical continuation analysis of the coupled laser model reveals a plethora of dynamical regimes such as stable phase-locking, periodic oscillations, period doubling, and chaotic oscillations, we only consider the conditions that yield stable phase-locking. As a result, the latter three dynamical behaviors are categorized as unstable locking regimes for the purposes of this study.

4.3.1 Imaginary coupling coefficient

The simplest representation of the model assumes no frequency detuning, a constant pump rate and a purely imaginary coupling coefficient represented as $i\kappa\tau_p$, which is representative of the case when the two supermodes experience similar losses. Figures 4.1(a) and (b) illustrate the stability maps within the same parameter space for in-phase ($\Delta\phi = 0$) and out-of-phase ($\Delta\phi = \pi$) solutions, respectively, as a function of $\kappa\tau_p$ and β at a pump power of $P_{1,2} = 1.2P_{th}$. The variable P_{th} denotes the pump power at lasing threshold for a single laser and can be identified from the steady-state solutions of the rate equations when no coupling is considered. The solid purple and blue lines in Fig. 4.1(a) denote the Hopf bifurcation boundary and the dashed purple line in Fig. 4.1(b) represents the pitchfork bifurcation boundary. The Hopf boundary in Fig. 4.1(a) can be further demarcated into the supercritical Hopf (purple) and the subcritical Hopf (blue) branches. The regions colored in green and orange denote the stable and unstable locking regimes, respectively, for both figures. The coexistence of in-phase and out-of-phase solutions for some

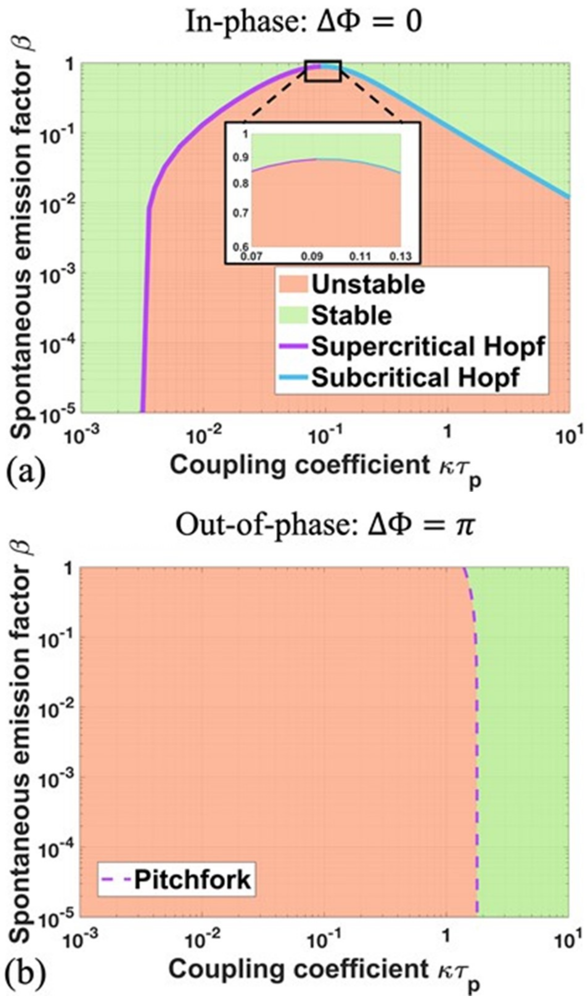

Figure 4.1: 2-parameter bifurcation diagrams of the (a) in-phase solution and (b) out-of-phase solution in ($\kappa\tau_p$, β) plane with $P_1 = P_2 = 1.2P_{th}$. Stable locking region is shown in green, unstable region in orange. Solid lines are the supercritical (purple) and subcritical (blue) Hopf bifurcation boundaries. Dashed line is the pitchfork bifurcation boundary.

values of $\kappa\tau_p$ and β can be explained by the fact that the two supermodes exhibit identical losses ($\gamma = 0$).

A phenomenon common to both Fig. 4.1(a) and (b) is the expansion of the green stable regions as β is increased from $10^{-5)}$ to its maximum possible value of 1. For the out-of-phase solutions depicted in Fig. 4.1(b), the slight increase in the area of the stable phase-locking region, located to the right of the plot at higher $\kappa\tau_p$ values, is easier to distinguish due to the solitary pitchfork boundary present in this graphic. In comparison, the supercritical and subcritical

Hopf bifurcations for in-phase solutions in Fig. 4.1(a) dissect the parameter space into multiple sections. For $\beta \leq 10^{-2}$, only one stable region exists at very small coupling rates and it remains nearly unchanged in area as β increases from 10^{-5} to 10^{-2}, bounded by the supercritical Hopf bifurcation point. In comparison, for $\beta > 10^{-2}$, it can be observed that the stable locking region in the weak coupling regime significantly expands when β is increased due to the supercritical Hopf bifurcation point moving to much higher values of $\kappa\tau_p$. Moreover, as the coupling coefficient $\kappa\tau_p$ further increases, a second stable region appears after the subcritical Hopf point, seen towards the right side of Fig. 4.1(a). This second stability region has not been reported in literature till date, where mainly weak coupling $\kappa\tau_p \ll 1$ and negligible β are considered. Despite the complex demarcations in Fig. 4.1(a), it can be clearly observed that increasing β leads to a narrowing of the unstable region as the boundaries of the two Hopf bifurcations move towards each other. In fact, when $\beta = 0.89$, the two bifurcation branches become connected at $\kappa\tau_p \approx 0.09$ as shown in the inset of Fig. 4.1(a). For values of β beyond this point of confluence (i.e. $\beta > 0.89$), the steady-state solutions of the rate equations yield in-phase, stable solutions irrespective of the coupling strength. This result holds major significance as it suggests that nanolasers with β values approaching 1 are ideal candidates to be used in phase-locking arrays to generate high power far-field emission.

4.3.2 Pump rate

In the previous section, the pump rate was fixed at a constant value for both lasers. In order to gauge whether increasing β leads to a similar expansion in the stability regions for any arbitrary pump rate, 3-dimensional (3-D) stability plots with varying P/P_{th} ($P_1 = P_2 = P$) being the third dimension, are created for the in-phase and out-of-phase solutions as shown in Fig. 4.2(a) and (b), respectively. The stable regions are denoted in white while the unstable ones are shaded in grey in these figures. For the in-phase solutions depicted in Fig. 4.2(a), when $\beta \leq 0.01$, the supercritical bifurcation branch (surface on the left) moves towards larger $\kappa\tau_p$ as the pump rate

P/P$_{th}$ increases, thereby enhancing the stability. This trend has also been reported in another study that focused exclusively on weak coupling and did not consider the effect of the β factor [86]. For $\beta \geq 0.01$, however, increasing the pump rate can cause the supercritical bifurcation to shift to smaller $\kappa\tau_p$, and thus shrink the stable locking region. This stability reduction as pump rate increases can be explained by the small signal analysis detailed in the Appendix. Essentially, for weak coupling, the damping rate of the small perturbations can be mathematically approximated to be that of the relaxation oscillations, with this rate increasing for small β and decreasing for large β as pump rate increases. Therefore, as the pump rate is increased for large β, the lower damping rate means that the system is now more susceptible to small perturbations and hence, exhibits less stability. Similarly, for the subcritical bifurcation branch (right side of the surface in Fig. 4.2(a)), an increasing pump rate P/P$_{th}$ pushes the branch to larger coupling coefficients, which also leads to narrowing of the stable locking region. Despite these seemingly disparate effects of the pump on stability, however, the most important observation from Fig. 4.2(a) is that the two Hopf bifurcation branches always move towards each other as β increases. The increasing proximity of the two bifurcations in turn, results in an expansion of the stability region. Therefore, it can be concluded that although varying the pump rate affects the stability in a non-uniform manner, higher β values always contribute towards increased in-phase locking irrespective of the pump rate.

In contrast, for the out-of-phase solutions depicted in Fig. 4.2(b), the pitchfork bifurcation boundary remains almost unaltered despite varying both P/P$_{th}$ and β. The reason for this can be inferred from small signal analysis (see Appendix),which reveals that the pitchfork boundary is approximately proportional to $N_{1,2} - N_0$. Given that N$_{1,2}$ clamps to a threshold value as P/P$_{th}$ increases, the stability boundary therefore stays almost constant. Though higher β values result in a slight increase of N$_{1,2}$, the consequent expansion of the stability region is miniscule. Fortuitously, for most applications, only the in-phase solutions are of interest as they are essential for the generation of higher power density. Therefore, in the next section when we consider

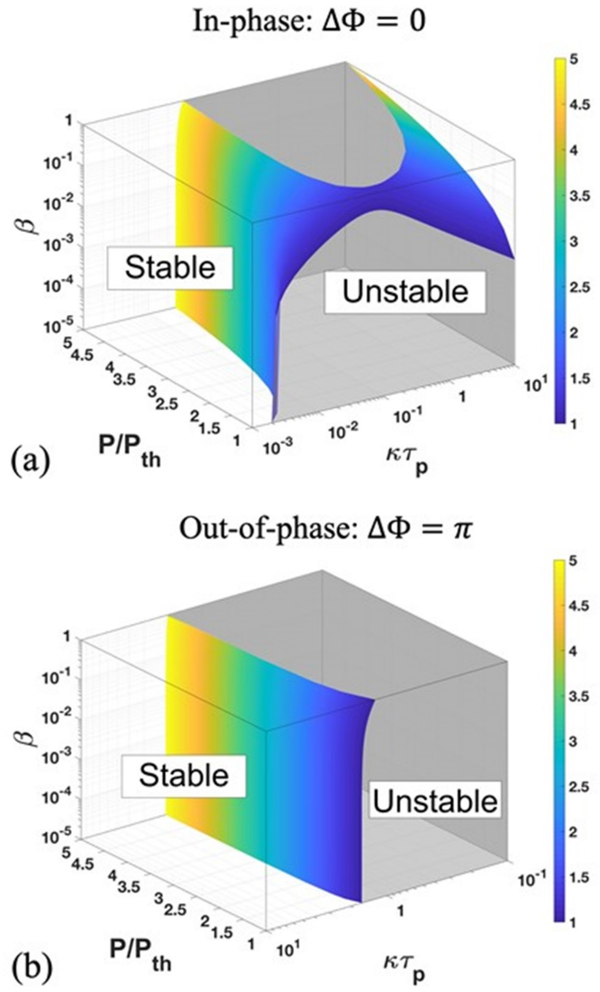

Figure 4.2: (a) 3-dimensional stability plot in the ($\kappa\tau_p$,P/P$_{th}$, β) plane for in-phase solutions. The 3-D surface is the Hopf bifurcation stability boundary. The color denotes various pump rate as shown in the colorbar. Stable phase locking region is shown in white, and the unstable region in grey. (b) 3-D stability plot in the ($\kappa\tau_p$,P/P$_{th}$, β) plane for out-of-phase solutions using same color convention as in (a). The surface now represents the pitchfork bifurcation stability boundary.

frequency detuning, we focus exclusively on the solutions around $\Delta\phi = 0$, which are referred to as "in-phase solutions" for simplicity.

4.3.3 Frequency detuning

Now we consider the case where two cavities exhibit disparate resonance frequencies and investigate whether a stability enhancement from high-β can be observed in this scenario.

While frequency detuning is usually induced by dissimilarities in the dimensions of the resonators caused by fabrication imperfections, it can also be intentionally introduced into the coupled structure for certain applications. For example, phase-locked laser arrays with shifted frequencies between the adjacent elements can be implemented in ultra-high-resolution lidar systems for distance-angle beam steering tasks [96–98].

In Fig. 4.3, the stable regions of the in-phase solutions are depicted in a 3-D parameter space $\kappa\tau_p$,$\Delta\omega\tau_p$, β) with $P_{1,2}/P_{th} = 1.2$. To provide a more intuitive visualization, the parameter space is dissected into two regions at $\kappa\tau_p = 0.1$, which is the approximate point of confluence where the supercritical and subcritical Hopf branches become connected, as shown in the zoomed-in inset of Fig. 4.1(a). Consequentially, Fig. 4.3(a) represents the region of $\kappa\tau_p \leq 0.1$ containing the supercritical Hopf bifurcation while Fig. 4.3(b) illustrates the scenario when $\kappa\tau_p \geq 0.1$ and the subcritical Hopf branch is observed. Like in Fig. 4.2, the stable and unstable regions are represented in white and grey, respectively, in Fig. 4.3(a) and (b) as well.

Detuning the frequency gives rise to two symmetric SN bifurcation boundaries for the case of weak coupling $(\kappa\tau_p \leq 0.1)$ depicted in Fig. 4.3(a). These SN bifurcation surfaces, along with the supercritical Hopf boundary, enclose the stable in-phase locking region. As detuning is decreased, the SN boundaries move closer to one another but remain unconnected for the case of zero detuning resulting in only Hopf bifurcation boundaries that are observed in this case. More importantly, as β increases, although the SN boundaries remain largely unperturbed, the supercritical Hopf branch relocates to higher $\kappa\tau_p$ values. This, in turn, expands the stable phase locking region in Fig. 4.3(a). Similarly, for$\kappa\tau_p \geq 0.1$ in Fig. 4.3(b), the stable phase locking region is also seen to expand for higher β values when the subcritical Hopf bifurcation serving as its sole boundary shifts towards smaller $\kappa\tau_p$. It is important to note here that the subcritical Hopf points for ultra-small β (the bluer-parts of the 3-D surface in Fig. 4.3(b)) require extremely high values of $\kappa\tau_p$ $(\kappa\tau_p > 10)$ which are not realistically achievable in experiment. This explains why the second stability region shown in Fig. 4.3(b) has not been previously reported in the literature where usually, only weak coupling and negligible β are considered. The results here indicate that increasing β helps expand the stable, in-phase locking regions for both weak and strong coupling cases despite the lasers demonstrating dissimilar frequencies.

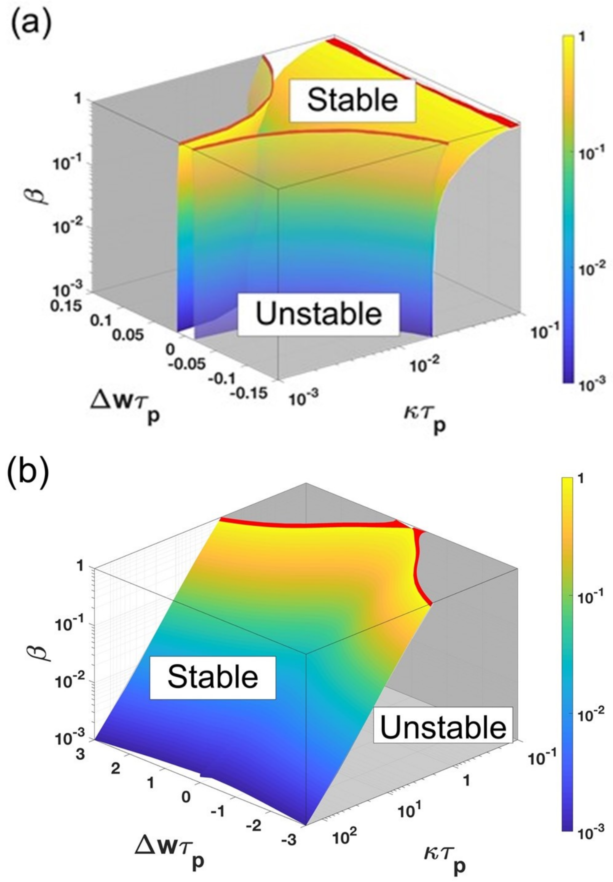

Figure 4.3: (a) 3-dimensional stability plot in the ($\kappa\tau_p$,$\Delta\omega\tau_p$, β) plane for in-phase solutions with $\kappa\tau_p \in [10^{-3}, 10^{-1}]$. The 3-D surfaces are the stability boundaries for Hopf and SN bifurcations. The colors denote varying β as shown in the colorbar. The red region denotes $\beta \geq 0.89$. Stable phase locking region is shown in white, and the unstable region is colored in grey. (b) 3-D stability plot in the ($\kappa\tau_p$,$\Delta\omega\tau_p$, β) plane for in-phase solutions with $\kappa\tau_p \in [10^{-1}, 200]$ using the identical color convention as in (a).

In Fig. 4.1(a), it was seen that when $\beta \geq 0.89$, stability holds irrespective of the strength of coupling for the $\Delta\omega = 0$ case. However, the same does not hold true when the frequency detuning between the two lasers is non-zero. For $\beta \geq 0.89$ with non-zero detuning, the stability boundaries are colored in red as shown in Fig. 4.3(a) and (b) and indicate that the stability is lost when detuning is non-negligible. To better illustrate the in-phase stability map with frequency detuning in the low, moderate and high β regimes, we combine the parameter spaces shown in Fig. 4.3(a) and (b) and present them in Fig. 4.4 as 2-D parameter projections at $\beta = 10^{-3}$,0.25 and approaching 1. The stable regions are now denoted in green while their unstable counterparts are colored in orange. Considering first the case of $\beta = 10^{-3}$ in Fig. 4.4(a), the stable solutions can be seen to be enclosed in an extremely narrow parameter space by the SN (dashed purple lines) and supercritical Hopf (solid purple line) bifurcations. As β is increased to 0.25 in Fig. 4.4(b),the stable region expands to cover a much larger area while a second stable region is created at high $\kappa\tau_p$ values due to the presence of the subcritical Hopf boundary (solid blue line). Finally, as β is increased beyond 0.89 in Fig. 4.4(c), the supercritical and subcritical Hopf boundaries merge, resulting in stable in-phase locking regions that span a significantly larger range of both $\kappa\tau_p$ and $\Delta\omega\tau_p$ values. Akin to what was observed when varying the pump rate, the desirable result of high-β increasing the stability of two laterally coupled lasers is preserved even when frequency detuning is considered.

It is worth mentioning here that the enhancement of stability due to large β for the non-zero frequency detuning case is not restricted only to the pump rate assumed in the above results. Though they have not been included in this work, additional simulations show that increasing or decreasing the pump rate around $P_{1,2}/P_{th} = 1.2$ will only slightly modify the quantitative value of the bifurcation points while the main features of the stability plots remain unaltered. Specifically, increasing the pump rate provides increased stability for coupled lasers with small β and a reduction in the stable region for coupled lasers with high β, as observed in Fig. 4.2(a). More importantly, it is observed that for any given pump rate, systems with higher β always demonstrate a larger stable phase locking region over the parameter space $(\kappa\tau_p, \Delta\omega\tau_p)$, i.e. better stability. Another reason for choosing the pump rate of $P_{1,2}/P_{th} = 1.2$ for the above simulations is that in practice, lasers operating lightly above threshold have the highest energy transfer efficiency,

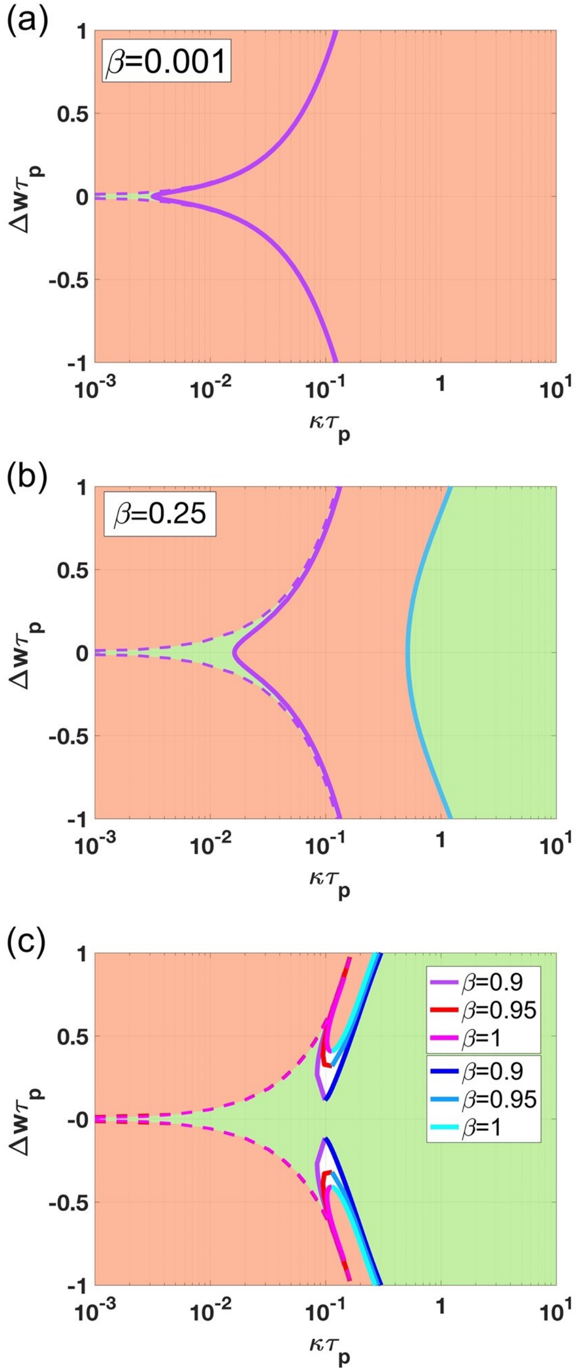

Figure 4.4: 2-parameter bifurcation diagrams of the in-phase solutions in the ($\kappa\tau_p$,$\Delta\omega\tau_p$, β) plane with $P_1 = P_2 = 1.2P_{th}$ for (a) $\beta = 10^{-3}$, (b) $\beta = 0.25$, and (c) $\beta \geq 0.9$. Stable locking regions are colored in green, unstable regions in orange. Solid lines represent the supercritical (purple, red, magenta) and subcritical (blue, light blue, cyan) Hopf bifurcation boundaries. Dashed line denotes the SN bifurcation points.

i.e. wall plug efficiency (WPE) [99], and can also be prevented from overheating due to large current injection. Since nanolasers with high β exhibit a low pumping threshold [28], it is not only energy efficient to operate slightly above threshold, but stable phase locking is also most achievable with a high β value and low pump rate.

4.3.4 Complex coupling coefficient

To further extend the analysis to account for the scenarios where the supermodes exhibit dissimilar losses, a complex coupling coefficient $i\kappa + \gamma$ - where κ and γ can be either positive or negative - is used to replace the purely imaginary coupling coefficient used thus far in the model. This modification is especially important if considering coupling geometries employing gain-guiding and carrier-induced index antiguiding [86], where either of the supermodes can exhibit higher eigenfrequencies and/or higher losses. In order to simplify the ensuing bifurcation analysis, the coupling amplitude $|\kappa|$ and phase θ_κ are used instead of κ and γ to provide better intuition for the control parameters used, i.e. $i|\kappa|\, e^{j\theta_\kappa} = i\kappa + \gamma$, $\kappa = |\kappa| cos\theta_\kappa$, and $\gamma = -|\kappa| sin\theta_\kappa$, where $\theta_\kappa \in [-\pi, \pi]$. Furthermore, the pump rates are assumed to be $P_{1,2}/P_{th} = 1.2$ to obtain a high energy efficiency in practice. Altering the pump rate around this value does not significantly impact the general shape of the stability regions and only negligibly shifts the boundaries. Therefore, the variation of the stable phase locking regions due to β is unlikely to be affected by the choice of the pump rate level. Finally, the frequency detuning is assumed to be 0 initially for simplicity, with a more detailed analysis on non-zero detuning discussed briefly towards the end of this section.

The stability plots, when considering the complex coupling coefficient and varying $\beta = 10^{-3}$, 0.05, 0.25 and 1, are superimposed and presented in Fig. 4.5(a). Although the bifurcation analysis yields a plethora of bifurcation boundaries, in Fig. 4.5(a), we only show those that directly demarcate the stable and unstable regions, i.e. Hopf points (solid lines) and the pitchfork points (dashed lines). In Fig. 4.5(a), the regions in red represent stable in-phase solutions, the ones colored in blue denote stable out-of-phase solutions and the white, unshaded

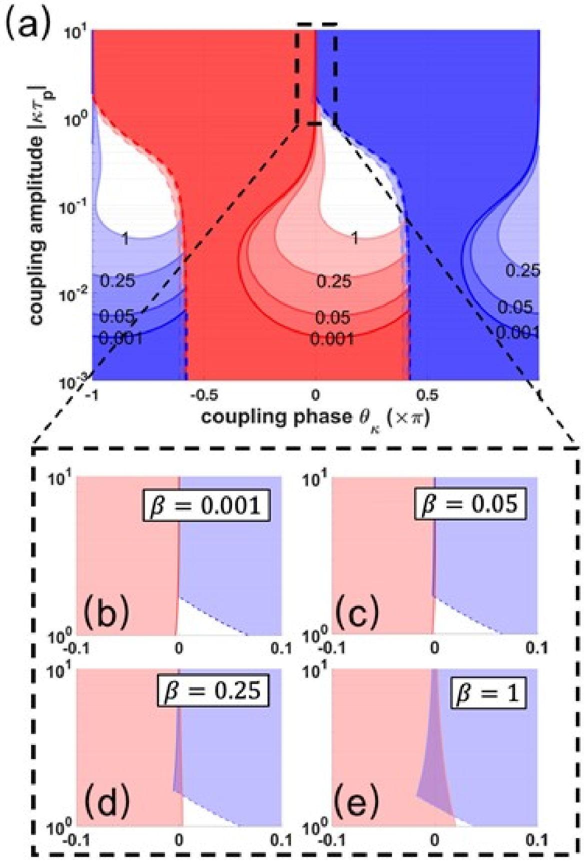

Figure 4.5: (a) 2-parameter bifurcation diagrams of in-phase and out-of-phase solutions in the (θ_k, $|\kappa\tau_p|$) plane with $\beta = 10^{-3}$, 0.05, 0.25 and 1. The stable in-phase locking region is shown in red; the stable out-of-phase locking region is colored in blue and the unstable region is shown in white. The solid lines denote Hopf bifurcations, while the dashed lines denote Pitchfork bifurcations. (b) – (d) Zoom-in of the region $\theta_\kappa \in [-0.1\pi, 0.1\pi], |\kappa\tau_p| \in [1, 10]$ for $\beta = 0.001, 0.05, 0.25, 1$, respectively.

regions represent unstable solutions. From this figure, it can be observed that the stability regions of in-phase (red) and out-of-phase solutions (blue) with the same β values are identical in shape albeit shifted with respect to each other by π radians. The reason for this horizontal shift, which can be easily deduced from the rate equations (Appendix), is that if γ flips its sign, i.e. θ_κ becomes $\theta_\kappa + \pi$, then $\Delta\phi$ is shifted by π radians. This underlines the significance that the signs of κ and γ hold and how controlling them would allow a coupled system to achieve the desired phase difference as predicted by the rate equations. However, the even more significant finding from Fig. 4.5(a) is that as β increases, both the in-phase and out-of-phase solutions expand in size, which is consistent with what was observed in Fig. 4.1(a) and (b). We would like to note that not all coupling values illustrated in Fig. 4.5(a) are realistically achievable in experiment. For instance, for coupled systems with $Q_{(+/-)}$ on the order of hundreds of more, γ cannot be on the same order as κ and therefore θ_κ values around $\pm\pi/2$ cannot be realized from the definition of the coupling coefficient provided in Section II. Nevertheless, the purpose of choosing this range of complex coupling coefficients is to provide an accurate picture of how the stability regions expand as β is increased.

Another interesting observation is the coexistence of in-phase and out-of-phase solutions in certain parts of the (θ_κ,$|\kappa\tau_p|$) parameter space, specifically around $\theta_\kappa = 0$ (and $\theta_\kappa = \pi$). Recall that around these values, the supermodes have nearly identical losses and therefore exhibit approximately equal probability of being supported by the coupled system. The same coexistence of solutions was also observed in Fig. 4.1(a) and (b), since the purely imaginary and positive coupling coefficient used in the analysis in that section can be viewed as a special case of $\theta_\kappa = 0$. The evolution of these bistable regions as β is varied is plotted in Fig. 4.5(b)-(e). It can be clearly observed that in addition to expanding stable regions, increasing β can also lead to a larger overlap of the in-phase and out-of-phase stable solutions, thereby increasing the likelihood of achieving bistability. Within these bistable regions, the final steady state depends on the initial state of the phase relations between the two solutions. Such bistable operation poses great potential for use as memories such as for optical flip-flops [41, 100] as well as for optical analogues of the degenerated spins in an Ising machine [101].

When non-zero frequency detuning is considered along with the complex coupling coefficient, it is observed that both the in-phase and out-of-phase stable regions have a lower bound in $|\kappa\tau_p|$, which is due to the SN boundary arising from the non-zero $\Delta\omega$. As $\Delta\omega$ increases, both the SN and Hopf bifurcation points are shifted in a manner that reduces the stable phase locking region in the parameter space (θ_κ, $|\kappa\tau_p|$). However, for any non-zero $\Delta\omega$, an enhanced stability from higher β can always be observed, which is consistent with the results from previous sections.

Though discussed briefly here, the detailed results are not included in this work for brevity.

In summary, with regards to stable phase-locking, increasing β unequivocally leads to an expansion in the stability regions despite considering varying pump rates, detuned frequencies and both imaginary and complex coupling coefficients. The robustness of the desirable effects of high β on stability truly emphasize the tantalizing potential of nanolaser arrays to harness this advantage and help in the generation of high optical power via in-phase locking. Additionally, high-β nanolaser arrays can also aid in the development of next generation active optical phased arrays as discussed in the next section.

4.4 Phase difference modulation vs. β

In the previous section, the stability of phase locking was studied as functions of β, P, $\Delta\omega$ and θ_κ. The results were focused on the in-phase ($\Delta\phi = 0$) and out-of-phase ($\Delta\phi = \pi$) solutions for their potential in high-power beam generation and optical memory. In some other applications such as beam steering for Lidar and imaging systems, a tunable phase offset between adjacent lasers is required. In fact, having a wide range of tunable phase differences between coupled lasers can prove essential in these applications, since this attribute can help increase the azimuthal and vertical scanning ranges. Using lasers as array elements instead of passive phase shifters injected by a single laser source offers the advantage of both frequency and phase reconfiguration, which are essential for complex detection and sensing applications [96, 97]. In this section, we theoretically propose and analyze a method to modulate the phase difference between two coupled lasers. For a symmetrically coupled system like we have considered thus far, i.e. equal pumping rate $P_1 = P_2$, the case of zero-frequency detuning $\Delta\omega = 0$ yields only two possible solutions for the steady-state phase difference $\Delta\phi$: the in-phase ($\Delta\phi = 0$) and the out-of-phase solutions ($\Delta\phi = \pi$). If the symmetry between the two lasers is broken by pumping the cavities at dissimilar rates, then values of $\Delta\phi$ that are neither 0 nor π are achievable. In fact, $\Delta\phi$ can then be tuned within the stable phase-locking range according to the ratio of the pump rates for the two lasers.

To identify the feasibility of nanolasers to be implemented in novel phased arrays for beam steering, the dependence of the phase difference tunability on β is investigated. In the simulation for each β value, the pump rate for one of the lasers, P_1, is fixed while the pump rate for its neighbor, P_2, is varied. We choose to keep $P_1/P_{th} = 1.2$ for the same reason of energy efficiency that was mentioned in the previous sections. To realize phase difference modulation, P_2 needs to be varied within a range where only stable phase locking is supported by the coupled cavities. Additionally, P_2 needs to be experimentally achievable and is thus varied only from P_{th} to $12P_{th}$ throughout this simulation. The three sequential steps followed to perform the analysis are as follows: First, by keeping β and P_1 constant, a one-parameter bifurcation analysis by varying P_2 is conducted, and the maximum and minimum possible $\Delta\phi$ within the stable region are recorded. Secondly, the above step is repeated for β's ranging from 10^{-5} to 1, and the maximum and minimum $\Delta\phi$ that can be achieved by varying P_2 are recorded for each β value. Finally, these results are depicted in Fig. 4.6(a) where the maximum and minimum $\Delta\phi$ values are plotted as a function of β, as well as in Fig. 4.6(b) where the phase tuning range representing the differences between the maximum and minimum $\Delta\phi$ is also shown as a function of β. For these simulations, the frequency detuning between the two lasers is neglected, and γ is assumed to be 0 for simplicity. Additionally, only an imaginary and constant coupling rate of $\kappa\tau_p = 10^{-3}$ is considered. It is important to note here that phase tunability was only observed with a coupling rate within the first stability region (to the left of the supercritical Hopf bifurcation boundary in Fig. 4.1(a)) and not for $\kappa\tau_p$ values in the second stability region (to the right of the subcritical Hopf boundary in Fig. 4.1(a)). Moreover, within the first stability region, varying $\kappa\tau_p$ affects the values of $\Delta\phi$ only in a negligible manner.

As can be clearly observed in Fig. 4.6(a) and (b), as β is increased, a wider range of tuning in $\Delta\phi$ is afforded. Specifically, in the yellow region demarcated by extremely low-β (10^{-5} to 10^{-3}), the maximum and minimum $\Delta\phi$ achievable are around -0.05π and 0.05π, respectively. As

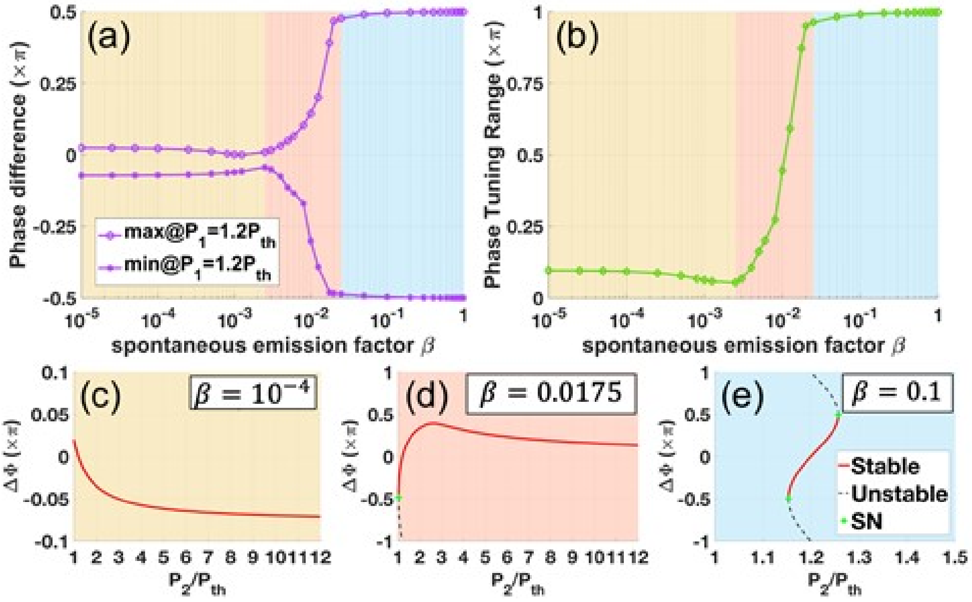

Figure 4.6: (a) Maximum and minimum phase differences achieved by varying the pump rate P_2 while keeping P_1 constant, plotted as a function of β. For each β value, the maximum values are marked with circles, and the minimum values are marked with asterisks. P_1 is set to be $1.2P_{th}$ (purple). (b) Phase difference tuning range as a function of β. The colored regions in both (a) and (b) represent the number of bifurcation points observed in the solutions. This is better illustrated in (c)-(e) which show the steady-state phase differences for three different values of β. Depending on the value of β, there may exist zero (c), one (d) or two (e) SN bifurcations points in the solution, corresponding to the yellow, pink and blue regions in (a), respectively.

β is increased to values in the blue region, the range for Δϕ expands significantly to about [-π/2, π/2]. Therefore, the phase tuning range shown in Fig. 4.6(b) increases from around 0.1π to π as β increases from that of conventional semiconductor lasers, i.e. $\beta \leq 10^{-3}$, to that of microscale and nanoscale lasers, i.e. $\beta > 0.01$. The reason for this wider range of phase tunability brought about by increasing β lies in the manner in which bifurcation points alter the stable solutions. For the range of extremely low-β values shaded as the yellow region in Fig. 4.6(a), the coupled lasers remain stable for all values of $P_2/P_{th} \in [1, 12]$ as shown in Fig. 4.6(c). However, when β is increased to values in the pink region of Fig. 4.6(a), an SN bifurcation point arises that pushes the lower limit of Δϕ closer to -π/2. This result is encapsulated in Fig. 4.6(d) for a specific value of $\beta = 0.0175$ that lies within the pink region in Fig. 4.6(a). Finally, for high-β values in the blue region of Fig. 4.6(a), two SN bifurcation points further define the stability boundary such that Δϕ can now vary from -π/2 to π/2 when P_2/P_{th} varies within a small range around 1.2, as illustrated in Fig. 4.6(e) for $\beta = 0.1$. Therefore, increasing β can significantly increase the range of phase differences possible for stable phase-locked solutions, highlighting the fact that laterally coupled nanolasers with intrinsically high β values can prove valuable in realizing wide scanning angles in optical phased arrays.

4.5 Conclusion

The theoretical effects of varying the spontaneous emission factor, β, on the stability and tunability of phase-locking in two laterally coupled semiconductor lasers are presented in this chapter. In order to first determine how β affects the stability of the coupled system, bifurcation analysis is performed over the laser rate equations using numerical continuation. Initial results with a simplistic model considering constant and equal pump rates, identical resonance frequencies and an imaginary coupling coefficient reveal that increasing β leads to an overall expansion of the stable phase-locking regions. To account for realistic experimental conditions and practical device designs, additional control parameters such as varying pump rate, frequency detuning and complex coupling coefficients were considered in the model. The desirable effects of high-β on stability were found to be robust to the addition of these multiple parameters. More importantly, the stable in-phase locking regions, conducive for generating high output optical power, were observed to increase in area as a direct result of increasing β. Such stability enhancement becomes even more significant for $\beta \geq 0.89$, where the in-phase solutions are stable over a wide range of coupling coefficients and frequency detuning. During the stability analysis, regions of bistability that increase in area due to increasing β were also observed. The simultaneous coexistence of two solutions in this manner can find applications in optical memories. Finally, higher values of β were also found to exert influence on the range of stable phase differences attainable from a laterally coupled system. By breaking the symmetry of pumping for the two lasers while altering β, a range of phase differences as wide as π (from -π/2 to π/2) was attained for $\beta > 0.025$. Wide ranges of tunability of this form are desirable in applications that require a large scanning angle and beam steering such as in lidar systems. This is the first study demonstrating rigorous analysis on the specific effects of high-β on the phase-locking stability and tunability of laterally coupled semiconductor lasers, to the best of our knowledge. Future analysis on the stability of coupled lasers can consider more than just two interacting lasers as well as specific coupling geometries.

4.6 Acknowledgement

Chapter 4, in full, has been submitted for publication of the material as it may appear in S. Jiang, S. S. Deka, S. H. Pan and Y. Fainman "Effects of High-β on Phase-locking Stability and Tunability in Laterally Coupled Lasers". The dissertation author was co-first author and contributed to the main idea of analyzing stability for high-β nanolasers, the discussion and writing of the manuscript.

Chapter 5

Reviewing Applications-Based Nanolaser Arrays

5.1 Introduction

In Chapters 3 and 4, the coupling between two semiconductor nanolasers was elaborated upon. While it is important to first understand the fundamentals of coupling with just two lasers, scaling up design to allow dense integration of a multitude of such emitters in a larger array format falls into the natural roadmap of the nanolaser technology [4, 102]. In this chapter, we will discuss the plethora of unique applications that become accessible due to larger-sized nanolaser arrays where the number of elements in the array, N is greater than 2. It is important to emphasize here, however, that not all nanolaser arrays rely on the same operating principles. The main distinction to be made is between uncoupled and coupled arrays. Uncoupled arrays comprise individual nanolasers that function independently and do not interact with their nearest neighbors. Some of the techniques to ensure isolation for two nanolaser systems [15, 103] can be extended to ensure zero cross talk for dense lattices. In direct contrast, coupled arrays, as the name suggests, rely on coupling of some form involving the constituent resonators comprising the system. This may be exhibited either in terms of evanescent coupling between the nanocavities or excitonic state-plasmonic surface lattice resonance coupling. Owing to their clear disparity, coupled and uncoupled arrays are each appropriate for different types of applications.

5.2 Uncoupled arrays

Coupling, especially strong coupling, makes the task of distinguishing between the individual resonators more complex since the two (or multiple) emitters can now be viewed as a new, larger system [15]. Therefore, for applications that rely on the individual state or output of each element in the lattice, uncoupled arrays are most suitable. A majority of sensing and imaging applications fall into this category as they rely on recording the wavelength shift of each nanolaser due to changes in the refractive index environment. One such study authored by Hachuda et al. [104] demonstrates the detection of protein in the form of streptavidin (SA) by using a 16-element 2D photonic crystal nanolaser array. The nanolaser geometry and array design, depicted in Figure 5.1A, show how a nanoslot is incorporated into the design. These nanoslots help with the localization of the optical mode which is especially significant, given that the measurements are performed in water to help with thermal stability [104, 105]. Although all the nanolasers are designed to be identical, the independence is maintained by optically pumping each one separately to record the redshift in emission wavelength – $\Delta\lambda$ – caused by the adsorption of protein in each individual nanolaser. The overall wavelength alterations for all 16 devices are then statistically evaluated using averaging and confidence intervals. Figure 5.1B portrays the results for $\Delta\lambda$ for each element in the array when impure solutions containing the protein SA are exposed to the nanolaser array. With water serving as the control (blue), it can be clearly observed that the array can distinguish between a sample containing SA (red) and those without it (black) based on the shift in emission wavelengths. In this experiment, bovine serum albumin (BSA) is treated as a contaminant to which the target protein, SA, is attached [104]. By averaging the results for all nanolasers in the array and increasing the amount of contaminant BSA, the limit of the array's sensitivity and selectivity can also be determined as shown in Figure 5.1C.

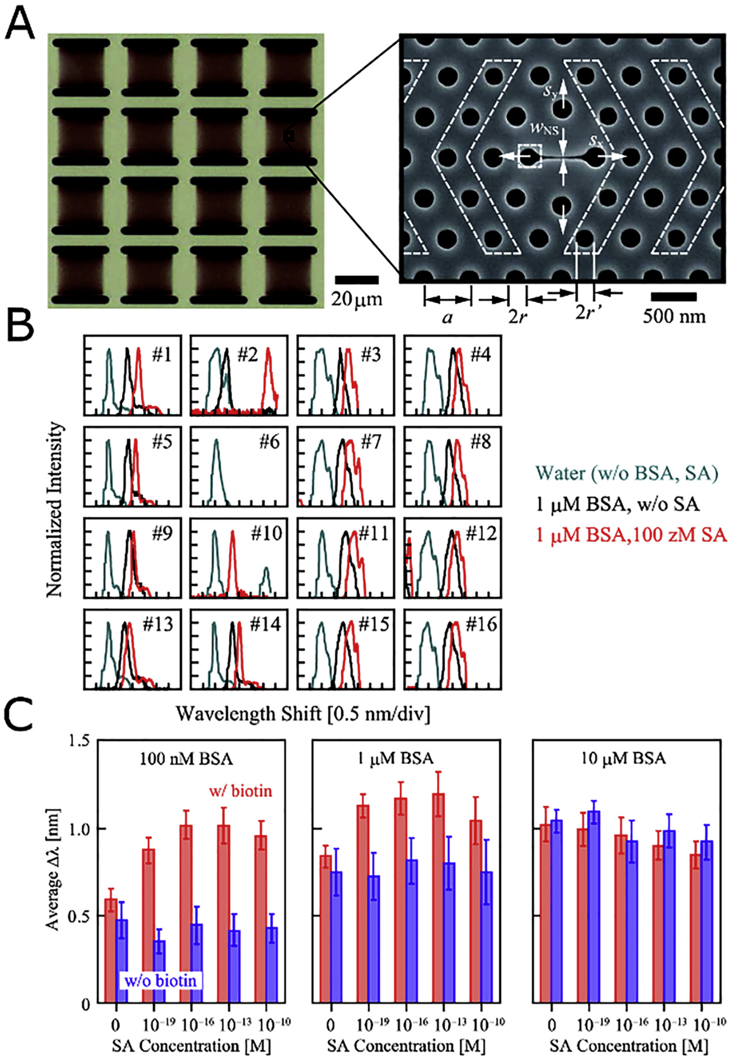

Figure 5.1: (A) Schematic of 16-element photonic crystal uncoupled array (left) and Scanning Electron Microscope (SEM) image of nanoslot-incorporated single laser (right). (B) Normalized intensity showing wavelength shift for all 16 elements under varying solutions. Water serves as the control. (C) Average wavelength shift calculated from all lasers – Δλ – plotted for increasing amount of contaminant bovine serum albumin (BSA). (Reprinted from [40].)

Based on the same principle of using Δλ from individual lasers, Abe et al. [106] demonstrate imaging of living cells using uncoupled arrays comprising 21 × 21 = 441 photonic crystal nanolasers. In their study, the cross talk isolation between individual array constituents is ensured by designing an offset in radii for all neighboring lasers, an idea reviewed earlier in Chapter 3. Figure 5.2A illustrates that it is possible to optically pump the entire array yet maintain independent operation due to the radii mismatch engineered in the design. To perform imaging, the target cell was deposited on top of the nanolaser array, and the subsequent shift in the emission wavelength was recorded for each array element. The $\Delta\lambda$ image is created by measuring the reference λ for each nanolaser and then mapping the $\Delta\lambda$ at each laser's position in the array. The results – illustrated in Figure 5.2B – not only provide an accurate albeit rough image of the cell but also demonstrate time evolution since the detection is continuous. Additionally, by employing nanoslots in their design, a Δn image is created which suppresses the noise and calibrates nonuniformity to yield a more accurate capture than its $\Delta\lambda$ based counterpart [106]. Figure 5.2C describes the ability of a Δn image to track the movement of a cell until it is desorbed, which in this case is shown to take upwards of 10 h.

Besides sensing and imaging, uncoupled lasing arrays can also be purposed to address other complex problems. By creating organic molecule-based laser arrays and using them in conjunction with distinct organic solutions, Feng et al. [107] demonstrate the possibility of creating nondeterministic cryptographic primitives. The randomness in the size distribution of the individual nanolasers is caused by the stochastic manner in which the organic solution forms capillary bridges around the array elements. The varying array types formed with four distinct organic solutions is shown in Figure 5.3A. Owing to multiple vibrational sublevels, the organic molecule used in this study is capable of exhibiting dual wavelength lasing at either 660 or 720 nm or both depending on the length of the cavity. Figure 5.3B describes the emission behavior as a function of the cavity length for arrays created with the different solutions. Clearly, four distinct emission states can be observed depending on the stochastic size distribution of the nanolasers – (1) no lasing, (2) lasing at 660 nm only, (3) lasing at both 660 and 720 nm, and (4) lasing at 720 nm only. These states can be represented as either quaternary bits ('0' for no lasing, '1' for lasing at 660 nm etc.) or double binary bits ('00' for no lasing, '01' for lasing at 660 nm, etc.). In order

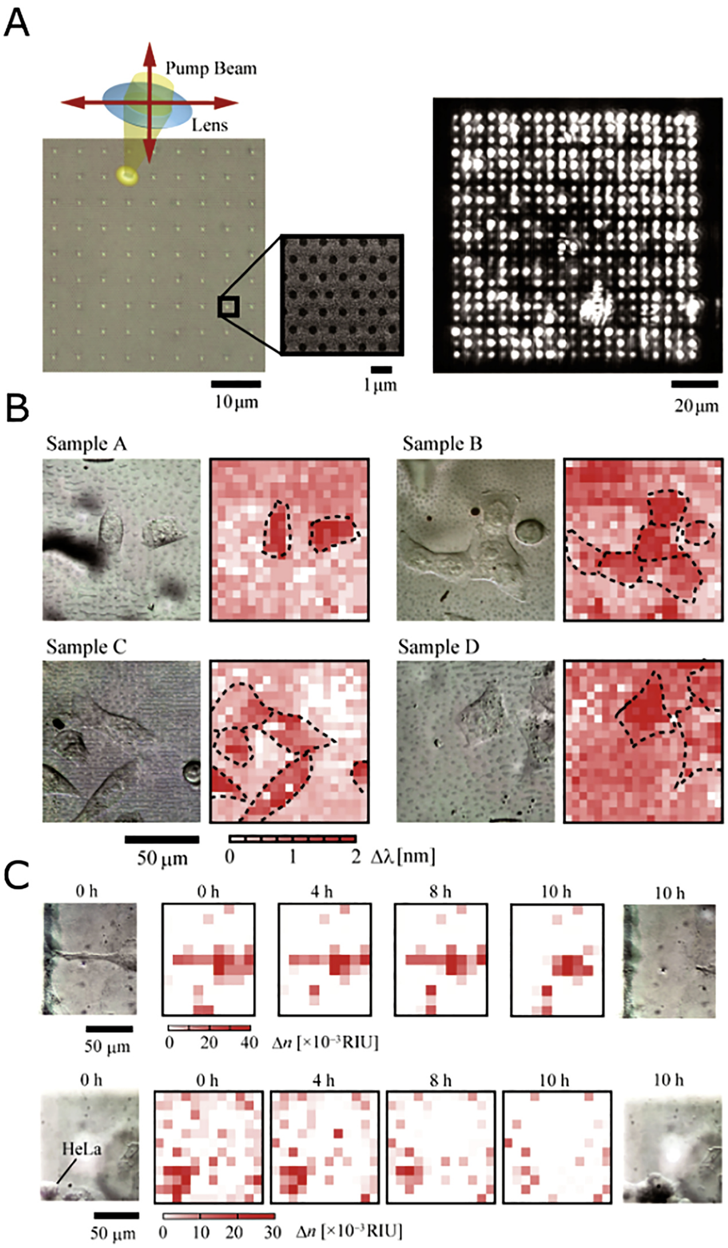

Figure 5.2: (A) SEM image of uncoupled nanolaser array (left) and near-field emission of the array (right). (B) Δλ image (right panels) of different samples of cells (optical micrographs; left panels) and (C) Δn image (center panels) tracking movement of a single cell (optical micrographs; left and right panels). (Reprinted from [40].)

to generate a cryptographic sequence from the arrays, each nanolaser is pumped separately with the pump then subsequently scanned to get the emission spectra from all other devices [107]. This technique, portrayed in Figure 5.3C, yields different encoding bits for each nanolaser (depending on its cavity length) which can be used to generate cryptographic bit sequences like in Figure 5.3D. In fact, encoding as double binary bits makes it possible to generate up to 2048 binary bits.

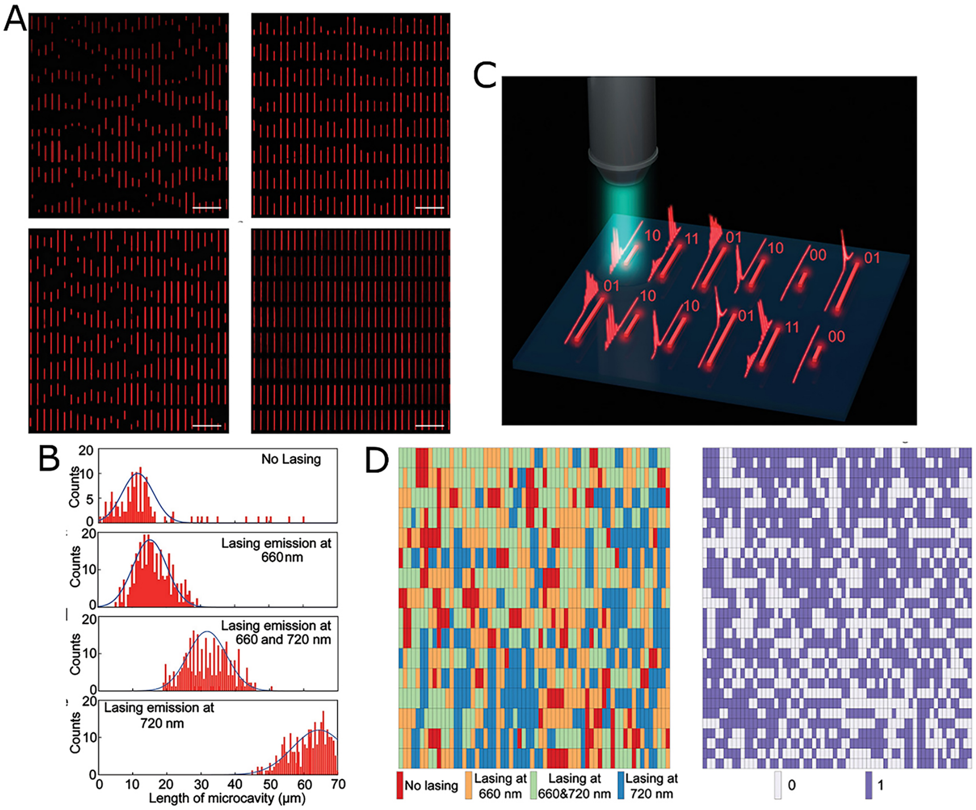

Figure 5.3: (A) Organic nanolaser arrays with stochastic size distribution dependent on the organic solution used during fabrication. Scale bar: 100 μm. (B) Distribution of cavity lengths for four distinct emission states. The distribution illustrates how the length of the nanolaser determines the emission state. (C) Scanning of each individual nanolaser with a pump pulse. Depending on the emission state, the spectral information can be encoded as a bit. (D) Cryptographic sequence generated by treating emission states as quaternary bits (left) and double binary bits (right). (Reprinted from [40].)

The studies elaborated above are only a fraction of the multiple works demonstrating how uncoupled arrays can achieve unique applications. Whether used for refractive index sensing, imaging or developing next generation, all-photonic cryptographic primitives, maintaining the independence of each nanolaser in the array is of vital importance for these applications [106–108]. Additionally, nanolaser arrays offer distinct advantages for some of these applications such as higher sensitivity compared to Raman-based sensors as well as a label-free imaging method

[106, 108]. The use of such arrays can also be extended to telecommunications, lab-on-a-chip applications, spectroscopy, and parallel detection [109–111]. Finally, integration of up to 11,664 nanolasers has already been demonstrated in a photonic crystal uncoupled array, underlining the feasibility of achieving even higher on-chip packing density in the future [112].

5.3 Coupled arrays

Contrary to independent nanolaser operation in uncoupled arrays, coupling can give rise to different types of nonlinear dynamics and in general, increases the complexity of the physical mechanisms involved in the process. It is well worth investing effort to understand these underlying phenomena however, as coupling allows much greater control on the emission properties than is possible with uncoupled operation. Coupling in arrays has been demonstrated in a variety of manners including bound state in-continuum mode coupling [113, 114], interferential coupling [115], transverse-mode coupling [116], surface plasmon–based coupling [117–125], and evanescent coupling [126–130]. We will focus this chapter mainly on the latter two forms since a majority of the literature on nanolaser arrays was found to rely primarily on these two mechanisms.

In order to present an idea of the breadth of functionalities enabled due to coupling, in this section, we review some of the relevant alterations to the emission along with the associated studies demonstrating the principle. It is important to note here that plasmon-based coupling is usually reported to affect properties of the emission such as directionality and wavelength. For most implementations of coupled arrays based on this physics, a lattice of metal nanoparticles creates the localized surface plasmon (LSP) resonance while some form of liquid dye medium, in which the lattice is immersed, serves as the gain or exciton states(ESs). This type of hybrid resonance is referred to as the ES-LSP. Although some aspects of the lasing phenomena are yet to be fully understood, the general consensus is that it occurs due to the excited-state molecules being stimulated to transfer energy to the lattice plasmons of the same frequency, phase, and polarization [119, 131]. In other words, the localized near-fields of the plasmonic particles comprising the array can stimulate the gain regions surrounding the particles to emit stimulated light at a wavelength that matches that of the lattice plasmon mode. With stimulated emission from the dye gain and a distributed cavity-like resonance provided by the lattice plasmon, lasing action can thus be obtained. It is important to note here that the reason for the tight confinement of light in these 2D metallic nanoparticle arrays is due to the strong interaction between the LSP resonances of individual particles and the far-field diffractive modes that satisfy the Bragg conditions of the array [132]. In comparison, evanescently coupled arrays can yield high powers and even generate states with orbital angular momentum (OAM) through the interplay between the lattice geometry and the modes of the individual lasers. Unlike for ES-LSP coupling where the resonance structure and gain are disparate media, for evanescent interactions, the active medium (usually comprised III-V semiconductors) is not external to the resonant structure; instead, it is a part of the cavity that supports the electromagnetic mode.

5.3.1 Beam directionality

Ability to control the direction of emission is of notable significance for wireless communications and nanoscale biosensors among other applications. A manner in which the angle of maximum emission from a nanolaser array can be modified involves altering the angle and/or polarization of the input optical pump. Zhou et al. [119] demonstrate this functionality by employing Au and Ag nanoparticle arrays immersed in a polymer gain comprising polyurethane and IR-140 dye gain. The schematic of the nanoparticle array is reproduced in Figure 5.4A, where the glass substrate and coverslip sandwich the lattice and gain layers. When the authors tune the pump angle to either be parallel to or 45° to the lattice direction, the far-field lasing beam patterns from the array are noticeably distinct as illustrated in Figure 5.4B. Depending on the angle of the pump, certain nanoparticles exhibit increased localizations of the electromagnetic mode, which in turn, affects the overall direction of the beam emitted from the array. It is also observed that the Ag array performed significantly better than its Au-based counterpart owing to reduced optical losses of the former [119].

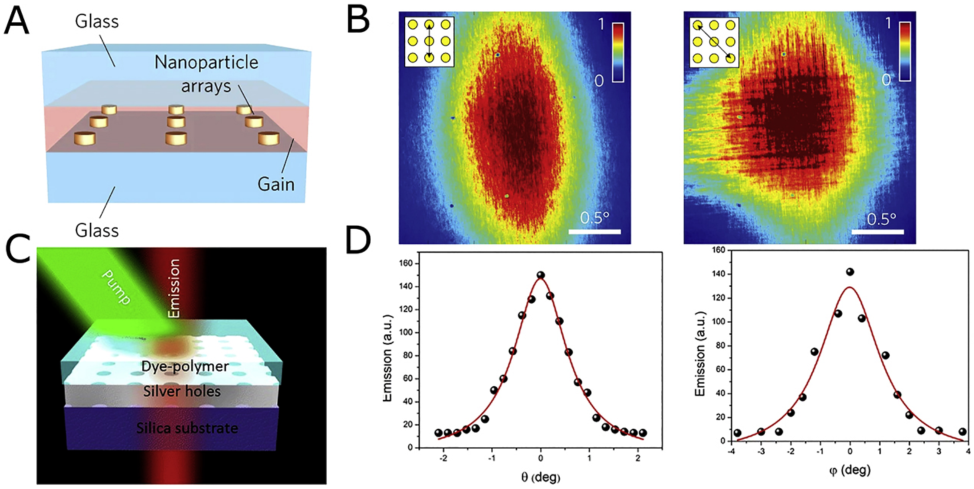

Figure 5.4: (A) Schematic of metal nanoparticles embedded in dye gain and sandwiched between two glass slides. (B) Far-field emission patterns of the nanolaser array in (A) for pump incidence angle parallel to (left) and 45deg (right) to the lattice direction. (C) Schematic of Ag film with nanoholes immersed in dye-polymer gain. (D) Emission intensity from the coupled nanolaser array in (C) as the detector angle is varied along the horizontal (left) and vertical (right) directions. (Reprinted from [40].)

Based on a similar though not identical material system as the work above, Meng et al. [120] also demonstrate highly directional lasing from their coupled spaser array. Their design consists of an Ag film with nanometer-sized holes, as opposed to nanoparticles, which is covered with an organic dye-polymer gain as shown in Figure 5.4C. Instead of altering the pump incidence angle, however, the detector itself is rotated to measure the directionality of the array output emission. Measuring the emission at varying detector angles along both the horizontal and vertical directions yields the results in Figure 5.4D. The narrow width of the measured emission as a function of the detector angle confirms the coherent, directional nature of the output beam. Lasing from this array is attributed to a surface plasmon polariton Bloch wave which also relies on some amount of feedback from plasmonic mode coupling between the Ag holes. The presence of the feedback is confirmed by the absence of lasing when an aperiodic lattice is used instead of a periodic one [118].

5.3.2 Tunable emission wavelength

Control over the emission wavelength of nanoscale light sources is desirable for dense wavelength division multiplexing (WDM) applications at a chip-scale level [44]. Other potential uses of tuning can be in lidar and imaging/sensing systems. In addition to achieving directionality of beam emission, it is also possible to alter the wavelength of output light from coupled arrays. Incidence angle and polarization of the pump can play a determining role in this respect as well. In one study, Knudson et al. [121] create a rhombohedral Al nanoparticle array which is then immersed in dye gain like the works referenced to in the previous section. Depending on the in-plane pump polarization, the ES-LSP–based mechanism leads to the array emitting at either 513 and 570 nm or both. This tuning of the output light from the array is described via Figure 5.5A and B which show the experimental streak camera images and numerically simulated spectra of the structure used in the study, respectively. The authors also elaborate on how selection of the nanoparticle shape comprising the array can determine the location of the electric field enhancement (i.e., the plasmon hotspots) [121]. In fact, other studies have demonstrated that unique shapes such as bowties can also exhibit ES-LSP–based nanocavity array lasing along with wavelength tuning [122]. Moreover, the Purcell factor is significantly enhanced due to the bowtie design, which in turn drives down the threshold allowing for room temperature lasing [122].

Finally, van Beijnum et al. [123] use a related phenomenon – surface plasmon associated lasing – to report that depending on the angle at which the emission from their array (comprising Au holes and InGaAs gain) is measured, the wavelength recorded varies. Besides angle-resolved experiments to select the peak emission wavelength, altering the temperature is another technique that can be leveraged to attain the same goal. This may be accomplished via two main mechanisms: the first involves modifying the stoichiometry of the gain material based on thermal annealing. The second pertains to the temperature-induced red-shift of the bandgap commonly referred to as

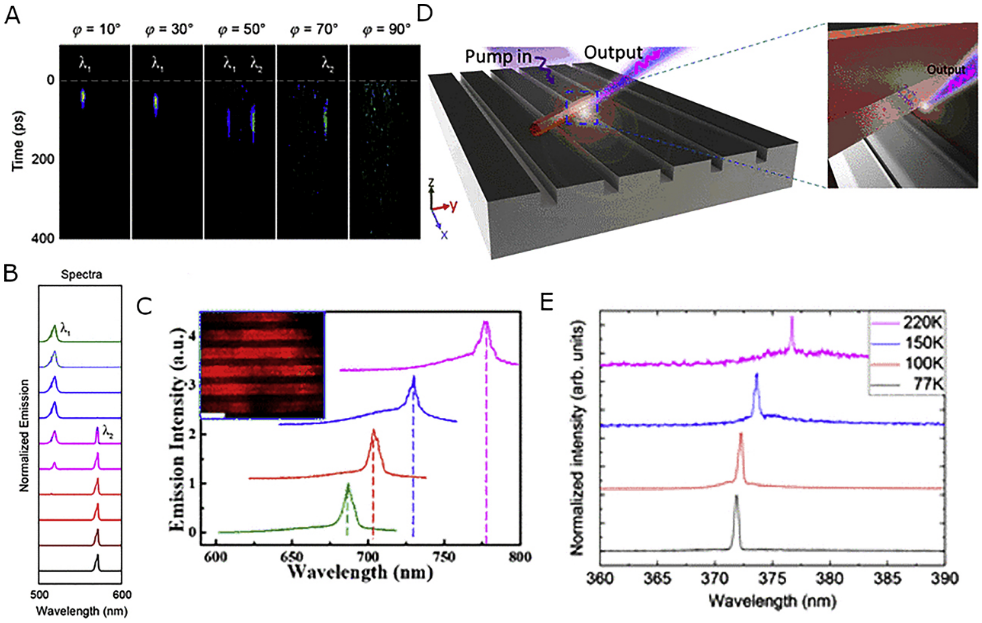

Figure 5.5: (A) Experimental streak camera images of nanolaser array as the in-plane pump polarization is altered. (B) Numerical simulation of the spectra for varying pump polarization. (C) Spectra of nanolaser array as sample is annealed. A blue-shift in the peak wavelength occurs; Inset: Fluorescent microscope image of nanolaser array. (D) Schematic of pseudowedge nanolaser array with ZnO nanowire placed on top of Ag grating. (E) Varshni red-shift of emission wavelength as ambient temperature is increased. (Reprinted from [40].)

the Varshni shift [133]. Huang et al. [124] demonstrate a wavelength-tunable device based on the former principle by combining an Au/SiO2 grating resonance with lead halide perovskite gain material. By thermally annealing their structure in a CH_3NH_3Br environment, the hybrid plasmonic mode in which the coupled nanolaser array operates in is observed to be blueshifted in emission wavelength as shown in Figure 5.5C. More importantly, this modification of the wavelength is a reversible change and the original peak wavelength can be recovered after the annealing process [124].

Similar to thermal annealing-based alterations, tuning predicated on the Varshni shift is also caused by temperature acting as the catalyzing factor. However, the latter method differs in that it does not require any specific chemical environment to be implemented and the alteration in the emission wavelength is always a red-shift irrespective of the material. The pseudowedge plasmonic nanolaser array presented by Chou et al. [125] exhibits such a red-shift in the emission wavelength based on operating temperature. Their structure, consisting of a ZnO nanowire placed on an Ag grating (Figure 5.5D), forms an unconventional array from the intersection points of the nanowire and the grating notches. This array displays single-mode lasing albeit subject to the manner in which the nanowire is positioned. By increasing the operating temperature from 77 to 220 K, the array undergoes a clear spectral red-shift as evidenced in Figure 5.5E due to the bandgap alterations in the ZnO caused by increased temperature.

5.3.3 Single and multimode lasing

The studies on coupled arrays mentioned thus far portray instances of single-mode lasing. However, some specific cases such as multimode fiber–based WDM sources and on-chip multiplexing in photonic devices may also benefit from multimodal operation instead [134]. To meet the need in these niche areas, some studies such as the one authored by Wang et al. [117] have created ES-LSP nanolasing arrays with the capability to switch between the more common single-mode operation and a multimodal one. The researchers are able to do so by designing two distinct types of lattices – a single lattice where the individual nanoparticles collectively contribute to the resonance and a superlattice,where several single lattices combine to give rise to multiple band edge states. This contrast is displayed in Figure 5.6A, where the lasing emission from a single lattice (left, bottom) is seen to be single mode (right, bottom) while that from the superlattice (left, top) is observed to be multimodal in nature (right, top).

While single-mode and multimode operation can be demonstrated on individual lattices, an altered superlattice as illustrated in Figure 5.6B is designed to combine the two functionalities. This new design can be viewed as a single lattice from one direction and a superlattice from another. By doing so, both single and multimode emission are achieved from the same sample based on the polarization and direction of the input pump (Figure 5.6B). Specifically, if the pump direction is perpendicular to the lattice, the array operates in the single-mode lasing regime, whereas when the pump is parallel to the lattice direction, multimodal lasing is observed. In addition, the

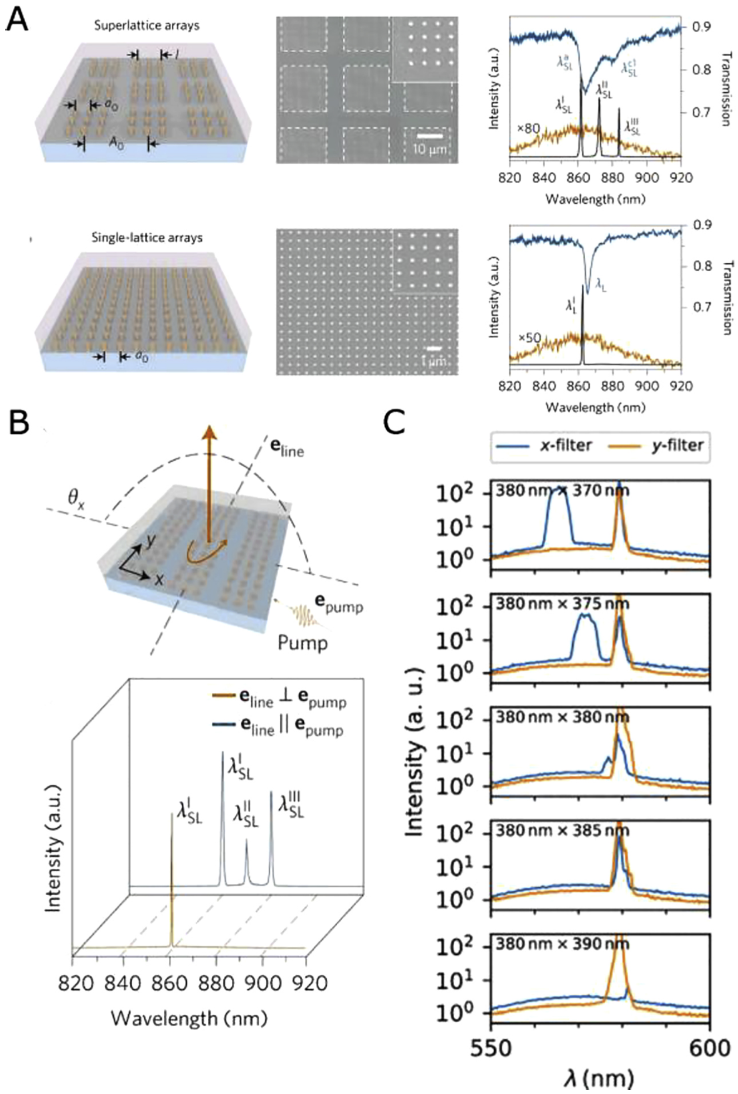

Figure 5.6: (A) Schematic of superlattice and single lattice arrays (left), their SEM images (middle), and their corresponding spectra (right). The superlattice exhibits multimodal lasing (top, right), whereas the single lattice demonstrates single mode lasing (bottom, left) as evidenced by the lasing spectra shown as black solid curves in both figures. (B) Schematic of altered superlattice (top) and its output lasing spectra (bottom). If the pump direction is perpendicular to the lattice, the array operates in single mode lasing regime, whereas when the pump is parallel to the lattice direction, multimodal lasing is observed. (C) Experimental emission spectra for Ni nanodisk array for varying lattice periodicities. The presence of both x and y polarized modes confirms multimode lasing for some periodicities. (Reprinted from [40].)

wavelength of emission can be tuned by altering either the size of the Au nanoparticles or the concentration of the dye gain comprising the nanostructure [117].

By choosing materials with unique properties for the coupled array, the applications for these devices can be extended to an even wider range of platforms. For instance, by employing a FM material like Ni to create nanodisk arrays in conjunction with dye gain, Pourjamal et al. [118] demonstrate the possibility of overcoming inherent losses in magnetoplasmonic systems. Their experimental results portrayed in Figure 5.6C underline the array's capability to switch between single and multimode lasing by modifying the particle periodicities in both the x and y directions. The authors claim that these arrays can potentially be used in the emerging field of topological photonics [118].

5.3.4 Higher output power

Owing to their compact size, nanolasers inherently possess low power consumption characteristics and low output power [135]. However, if the lasers are designed and placed in close proximity such that the emission of a multitude of such lasers is coherently combined, a significantly higher output power can be obtained. The studies demonstrating this concept that are discussed in this section underline the great potential for nanolaser arrays to be employed in farfield applications, such as optical interconnects [4] and beam synthesis [136].

In their study based on a $N = 81$ element evanescently coupled photonic crystal nanolaser array, shown in Figure 5.7A, Altug et al. [127] are able to observe higher output powers with their coupled array than with a single emitter. Specifically, the maximum power achieved by the coupled array is found to be about $\sim$100 times higher than that reached by the single cavity. More importantly, the coupled nanolaser array demonstrates a $\sim$20-fold increase in the differential quantum efficiency (DQE) compared to their single laser counterpart. The DQE here refers to the slope of the LL curve above threshold and is extracted from the experimental results depicted in Figure 5.7B. Additionally, numerical analysis of the coupled rate equations reveals that with increasing N, both DQE and the maximum output power achievable show a corresponding increase (Figure 5.7C).

Increased output power has also been observed with other material systems such as metal-

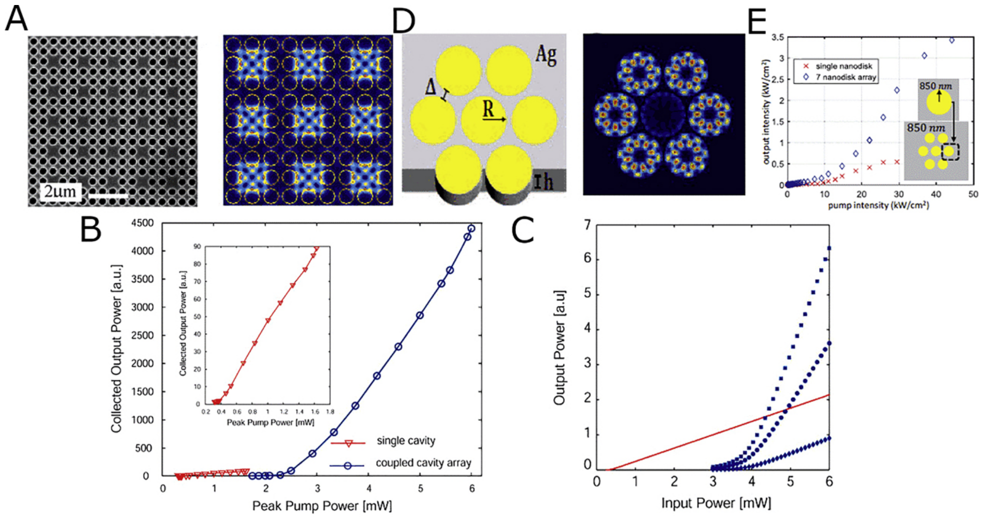

Figure 5.7: (A) SEM image of photonic crystal nanolaser array (left) and simulation of the modes supported by the system (right). (B) Output power of coupled cavity array shown in (A) compared to that of a single cavity. Inset: Magnified version of curve for single cavity. (C) Numerical simulations of coupled rate equations comparing output power for single cavity (red) vs. that for a coupled cavity array with N = 10 (diamond), N = 40 (circle), and N = 70 (square). (D) Schematic of seven hexagonally designed metal-coated nanodisk lasers (left) and simulation of the mode structure supported (right). (E) Output intensity of one nanodisk vs. array as pump intensity is increased. Slope efficiency and power of array are much greater than that of single emitter. (Reprinted from [40].)

clad nanolaser arrays as reported by Hayenga et al. [128]f. In this investigation, the overall power emitted by a seven-element metallic nanodisk array arranged in a hexagonal pattern (Figure 5.7D) is measured. The electromagnetic mode pattern supported by this design is first simulated and is shown in Figure 5.7D. Then, upon measurement, the output intensity of this array is found to be 35 times higher than that of a single nanodisk. Additionally, the array's slope efficiency is five times that of the single nanolaser. These results, encapsulated in Figure 5.7E, emphasize the ability to coherently combine the emission of multiple nanolasers to yield higher powers.

5.3.5 Orbital angular momentum

In addition to obtaining higher power, nanolasers may also be engineered to produce unique properties such as vortex beams with OAM in the far-field. Operating in such a state requires careful consideration of the lattice size, shape, and even type of nanolaser comprising the array. Hayenga et al. [129] demonstrate that by altering the types of evanescently coupled metallic nanolasers, it is possible to segment arrays into those that exclusively output vortex beams but do not carry OAM and those that display both characteristics. Specifically, an array of 500 nm diameter coaxial nanolasers exhibits the former, regardless of the array size, while a nanodisk array with 850 nm radius produces the latter as portrayed in Figure 5.8A and B, respectively. The dissimilarity in the two designs is explained by the interplay between the geometrical shape of the lattice and the whispering gallery modes supported by individual nanolasers. Whereas rotation is essential for higher order modes supported by the nanodisks to reduce the overlap with the lossy metal, it has no significant effect on the TE_{01} modes supported by the comparatively smaller-sized coaxial nanolasers. Furthermore, the topological charge associated with the beams carrying OAM can be tuned according to the number of lasers in the array as depicted in Figure 5.8C.

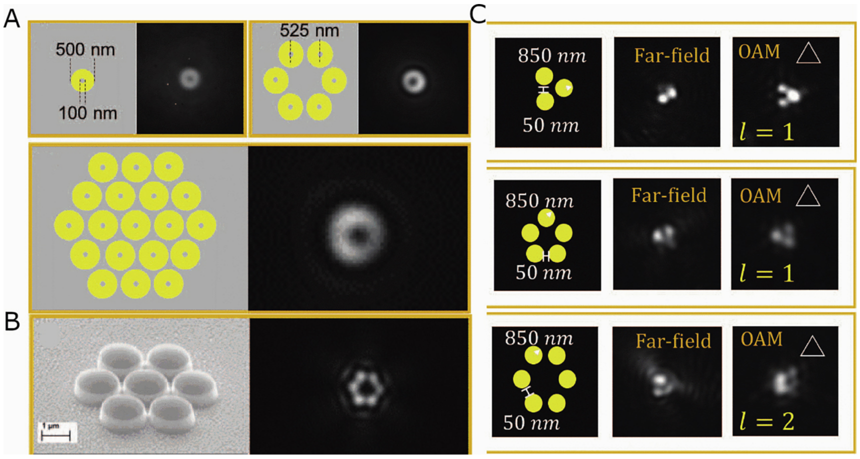

Figure 5.8: (A) Schematics and experimental far-field mode structure for coaxial metal nanolasers of different array sizes. Vortex beam with no angular momentumis observed regardless of array size. (B)SEM image (left) and far-field mode structure of seven nanodisk array (right). A vortex beam with angular momentum is confirmed. (C) Varying nanodisk array sizes (left), their corresponding far-field patterns (middle), and their respective topological charges (right).

It is also possible to multiplex OAM beams with high topological charges using integrated microscale lasers as demonstrated by Bahari et al. [137] in a recent study. This is accomplished by designing circular boundaries between topologically distinct photonic crystal structures as shown in Figure 5.9A. In this Scanning Electron Microscope (SEM) image, rings 1 and 3 are composed of a photonic crystal with a nontrivial bandgap obtained by bonding InGaAsP multiple quantum wells on yttrium iron garnet (YIG). In contrast, ring 2 comprises a trivial bandgap photonic crystal. The dissimilarities in these concentric resonators gives rise to orthogonal OAM beams of alternating chirality [137]. In other words, the sign of the topological charge alternates as one moves from the innermost to the outermost ring. The chirality of the beams can also be reversed by applying an external magnetic field. Figure 5.9B demonstrates the far-field intensity patterns of OAM beams arising from each individual laser and also from the multiplexed array. The topological charges associated with rings 1, 2, and 3 are $|l1| =100$, $|l2| =156$, and $|l3| =276$, respectively. The observation of interference fringes in both theory and experiment for ring 2 is characteristic of beams carrying OAM. Although there is no coupling between the individual lasers in this array, it nevertheless presents a tantalizing possibility of dense integration of any arbitrary number of lasers for multiplexed OAM generation [137]. Generating such beams on a more compact platform based on nanolaser arrays can be a promising direction for future research. Finally, another manner in which the properties of the beam emission such as OAM and directionality can be controlled is by choosing whether the topological nanolasers operate in a bulk or edge state. Using semiconductor nanodisk arrays, Shao et al. [138] demonstrate single-mode lasing from a bulk state by relying on band-inversion–induced reflection between trivial and topological photonic crystal cavities which exhibit opposite parities. As a result, although this bulk state mode does not carry OAM ($l = 0$), the emission is highly directional in the axis vertical to the cavity plane with divergence angles less than 6deg and side-mode suppression ratios of over 36 dB. Based on a similar material system but with a slightly altered cavity design, authors from the same group are also able to observe lasing of spin-momentum–locked edge states [139]. In addition to vertical emission, the output beam from these cavities is observed to carry a topological charge of l = -2, while also allowing for higher side-mode suppression ratios of over 42 dB.

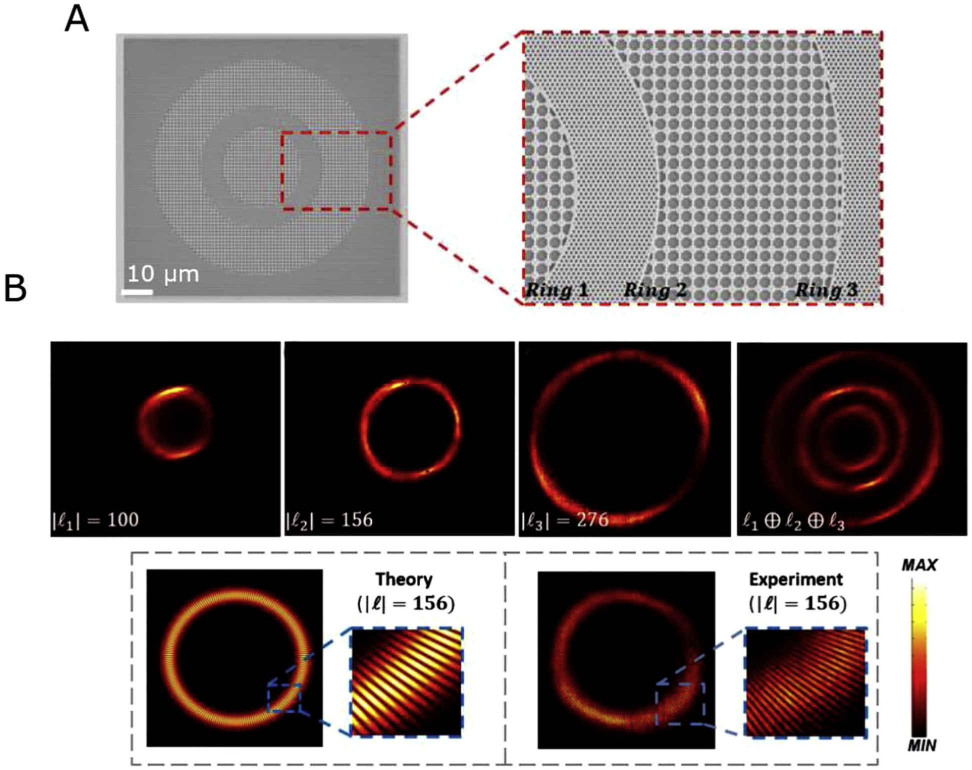

Figure 5.9: (A) SEM image of three concentric ring lasers composed of two different photonic crystal structures. Inset: rings 1 and 3 are composed of a photonic crystal with a nontrivial bandgap obtained by bonding InGaAsP multiple quantum wells on yttrium iron garnet (YIG). In contrast, ring 2 comprises a trivial bandgap photonic crystal and cylindrical air-holes. (B) Measured far-field intensity of the rings showing their individual OAM beams (top row, first three images from left) and the multiplexed OAM beam formed (top row, far right image) when all rings are pumped simultaneously. The interference pattern observed in the far-field emission from ring 2 matches well with theory and confirms the OAM carried in the beams.

Creation of vectorial vortex beams such as the ones mentioned in the above studies can be of great value in areas such as imaging, optical trapping, and laser machining [140]. At the same time, beams carrying OAM can find applications in micromanipulation and both classical and quantum communication systems [141]. Therefore, the ability of nanolaser arrays to demonstrate useful attributes such as in-phase and out-of-phase supermodes and vortex beams with and without OAM makes them an ideal device platform for catering to a plethora of applications [126, 130].

5.4 Conclusion

To conclude, recent progress on the development of array architectures of nanolasers is reviewed in this chapter. The focus was on valuable attributes realized due to unique array designs and the underlying physics that may help enable real-world applications such as biological sensing, imaging, and on-chip communications. Larger arrays can be distinguished depending on whether their constituent elements function independently from one another or demonstrate coupling of some form. Uncoupled arrays are more intuitive to understand and suitable for applications such as imaging, biosensing, and even cryptography. On the other hand, although coupling in nanolaser arrays can create complex dynamics, control over many aspects of the emission behavior such as beam directionality, mode switching, and OAM are afforded.

5.5 Acknowledgement

Chapter 5, in full, is a reprint of the material as it appears in S.S. Deka, S. Jiang, S.H. Pan, and Y. Fainman ”Nanolaser arrays: toward application-driven dense integration,” *Nanophootnics*, Vol. 10, Issue 1, pp. 149-169, 2021. The dissertation author was the primary investigator and author of this publication.

Chapter 6

Conclusion and Future Directions

In this dissertation, we focused on investigating particular attributes of metallo-dielectric nanolasers (MDNLs) that make them ideal candidates for dense on-chip integration in photonic integrated circuits (PICs) of the future. The studies were both theoretical as well as experimental in nature. In Chapter 2, we demonstrated the dynamic wavelength tuning and high-speed modulation of an MDNL based on an external electric-field. Such an E-field was found to induce alterations in the bandgap of the quantum well-comprised gain medium via the Quantum confined Stark effect (QCSE). Specifically, the QCSE causes two simultaneous bandgap alterations: 1) the energy levels of the bound states move towards each other which results in a redshift of the peak emission wavelength and 2) the electron and hole wavefunctions are move away from each other spatially which reduces the overlap between the wavefunctions and results in a decrease in emission intensity. We were able to experimentally observe a wavelength shift of upto 8.35 nm and an intensity attenuation upto $\sim$89% through this technique. Additionally, since the alterations are electronic-based (i.e. changes to bandgap), the wavelength tuning and intensity attenuation can be modulated at high speeds unlike with heat-based effects. In fact, we witnessed an intensity modulation upto 400 MHz, only limited by the detector 3 dB bandwidth. The ability to self-tune a laser and control its intensity in this manner can prove to be crucial for dense wavelength division multiplexing (WDM) applications at a chipscale level.

Since it is unlikely that a single nanolaser works in isolation in any real-world device, in Chapter 3, we considered the case of two MDNLs and investigated at what intercavity distances does near-field evanescent coupling become pronounced. Though intuitively, one would expect the metal to prevent any optical cross-talk between the neighboring resonators, our study showed that when designed close enough together, the two MDNLs interact via near-field evanescence at distances less than $\sim$50 nm despite the presence of the metal. Specifically, the increased coupling between the two resonators leads to the creation of two supermodes - the bonding and anti-bonding modes - which cause an exponential split in the eigenmode wavelengths and Q-factors of the modes supported by the system as the intercavity distance is reduced. Since some applications might require the two sources to operate independently without cross-talk, we also discussed two ways in which coupling may be inhibited between the two MDNLs: 1) by detuning the resonances of the two cavities via designing the radius of one laser to be 5% larger than that of its neighbor or 2) by designing the cavity radii to be larger so that they support higher order modes which are better confined to the gain media than lower order ones supported by smaller cavities. The results presented in this chapter underline the high packing density attainable on a chip with the use of subwavelength MDNLs.

Continuing from the previous chapter, in Chapter 4, we dived into further detail about the specifics of coupling but with regards to achieving phase locking between two laterally coupled lasers, a desirable goal which holds immense value for development of high-power and coherent optical beams necessary for applications such as LiDAR. Specifically, we numerically analyzed the effect of increasing β in the coupled rate equations for two laterally coupled lasers. Our results clearly demonstrated that high β values led to increased regions of stability for the coupled system despite varying control parameters such as the pump rate, frequency detuning and coupling coefficient. Additionally, high β values can also contribute to a wider range of stable phase differences possible (upto π radians) if the two lasers are pumped asymmetrically. Since

MDNLs innately exhibit high-β values, these results further encapsulate how they can form the building-blocks for densely packed optical phased arrays on chip.

Finally, in Chapter 5 we briefly discuss how nanolasers seem to be headed towards the inevitable direction of dense integration into arrays and lattices and some of the unique applications that have resulted. The focus was on valuable attributes realized due to unique array designs and the underlying physics that may help enable real-world applications such as biological sensing, imaging, and on-chip communications. Larger arrays can be distinguished depending on whether their constituent elements function independently from one another or demonstrate coupling of some form. Uncoupled arrays are more intuitive to understand and suitable for applications such as imaging, biosensing, and even cryptography. On the other hand, although coupling in nanolaser arrays can create complex dynamics, control over many aspects of the emission behavior such as beam directionality, mode switching, and OAM are afforded.

In summary, MDNLs offer a wealth of unique advantages such as ultrasmall footprints, low thresholds, electromagnetic isolation and current injection that make them more suitable for use as on-chip sources compared to other types of nanolasers. Other advantages elaborated on in this dissertation, such as dynamic, high-speed wavelength tunability and intensity modulation and stable phase-locking due to high β values, further add to their claim as ideal chipscale emitters. As highlighted in Chapter 5, research groups have already started undertaking the next step of realizing dense integration of nanolasers to achieve unique applications from sensing and imaging to beam directionality and OAM beam generation. However, there are still some directions yet to be experimentally demonstrated with regards to nanolaser arrays that we will discuss in the sections below:

6.1 Phase-locked laser arrays

As discussed extensively in Chapter 4, high β values unique to nanolasers significantly increase the possibility of achieving stable phase-locking with such emitters. However, achieving phase-locking in practice would require careful tuning of the important control parameters involved such as pump rate, frequency detuning as well as the coupling coefficient. Specifically, with regards to the coefficient, the nanolaser system must be designed such that the in-phase mode (usually the bonding supermode) is supported and has lower losses than the out-of-phase modes (anti-bonding modes). Achieving near-field coupling in this manner with nanolasers can unlock a plethora of novel applications previously inaccessible.

Whereas near-field coupling can lead to higher powers via in-phase stable locking, far-field coupling can also be used to realize this goal. In addition, combining far-field coupling with control over the phase and amplitude of individual nanolasers in an array can result in an optical phased array with both frequency and phase tunability, akin to RF phased arrays. The methods to achieve directionality in array beam emission demonstrated thus far are limited to altering the incidence angle/polarization of the pump. In contrast, a true optical phased array of nanolasers can offer multiple degrees of freedom and much more nuanced control of the directionality since each emitter in the array can be individually tuned in both frequency and phase. Such far-field coupling with quantum cascade laser arrays has already been demonstrated [84]. The challenge that lies ahead is to achieve the same for subwavelength nanolaser arrays and preferably, with current injection.

6.2 Ultrashort pulse generation

When discussing nanolasers, an often-overlooked topic is ultrashort pulse generation. Typically, such pulses are created using mode-locking techniques, which can include both active and passive mode-locking. Due to the need for external design elements such as saturable absorbers or electro-optic modulators, achieving mode-locking with nanoscale lasers faces impediments. However, Gongora et al. [142] demonstrate in a recent work that it is in fact possible to mode-lock nanolasers in an array without external design elements by relying on the nonradiative nature of anapole states. Using this technique, the authors numerically demonstrate an ultrashort pulse down to 95 fs generated from an array whose constituent nanolasers are spaced apart evenly in frequency from one another to mirror mode-spacing in traditional mode-locking theory. It is also observed that the position of the nanolasers can alter the duration of the pulse generated [142]. Despite this result, experimental results of mode-locked nanolasers for ultrashort pulse generation are yet to be demonstrated. Doing so can unlock a wealth of applications in areas requiring short optical pulses such as LiDAR, optical regeneration, nonlinear optics, and optical sampling [55].

6.3 Acknowledgement

Chapter 6, in part, is a reprint of the material as it appears in S.S. Deka, S. Jiang, S.H. Pan, and Y. Fainman ”Nanolaser arrays: toward application-driven dense integration,” *Nanophootnics*, Vol. 10, Issue 1, pp. 149-169, 2021. The dissertation author was the primary investigator and author of this publication.

Appendix A

Normalization and the Linear Analysis of Coupled Rate Equations

Before we perform the small signal analysis, the different bifurcation points need to be introduced and identified. The saddle-node bifurcation indicates the collision and disappearance of two equilibria. A pitchfork bifurcation occurs when the system transitions from one fixed point to three fixed points. In both these types of bifurcation points, the Jacobian matrix of the dynamical systems has one zero eigenvalue. In contrast, at the Hopf bifurcation points, the solution switches from being stable to exhibiting periodicity, i.e. instability. For the supercritical Hopf bifurcation, one fixed point diverges into periodic oscillations, while the reverse holds true for the subcritical Hopf bifurcation. The occurrence of this Hopf point corresponds to a pair of purely imaginary eigenvalues. We use a linear gain model for $G(N_{1,2})$ with $G(N_{1,2}) = G_N(N_{1,2} - N_0)$, where G_N is the differential gain and N_0 is the carrier density at transparency. The rate equations in (1) can be normalized using $X_{1,2} = |E_{1,2}|\sqrt{G_N \tau_{nr}}$, $Y_{1,2} = (N_{1,2} - N_0)\Gamma \tau_p G_N$ and a dimensionless time that is normalized to the photon lifetime as $t = \tau/\tau_p$. We can then write the normalized equation as:

$$
\begin{aligned}
\frac{dX_{1,2}}{dt} &= \frac{1}{2}(Y_{1,2}-1)X_{1,2} + \frac{\tau_{nr}}{\tau_{rad}}\frac{F_p\beta}{2}\frac{Y_{1,2}+N0_{norm}}{|X_{1,2}|^2}|X_{1,2}| \\
&\mp \kappa\tau_p cos(\Delta\phi)X_{2,1} + \gamma\tau_p sin(\Delta\phi)X_{2,1} && \text{(A.1)} \\
\frac{dY_{1,2}}{dt} &= T_{norm}[P_{norm} - \gamma_c(Y_{1,2}+N0_{norm}) - Y_{1,2}X_{1,2}^2] && \text{(A.2)} \\
\frac{d\Delta\phi}{dt} &= \frac{\alpha}{2}(Y_2-Y_1) + \Delta\omega\tau_p + \kappa\tau_p(\frac{X_1}{X_2}-\frac{X_2}{X_1})cos(\Delta\phi) \\
&- \gamma\tau_p(\frac{X_1}{X_2}+\frac{X_2}{X_1})sin(\Delta\phi) && \text{(A.3)}
\end{aligned}
$$

where $\mathrm{T}_{norm} = \tau_p/\tau_{nr}$, $\mathrm{N}_0 norm = \mathrm{N}_0\Gamma\tau_p\mathrm{G}_N$, $\gamma_c = \frac{\tau_{nr}}{\tau_{rad}}(\mathrm{F}_p\beta + 1 - \beta)$, and $\mathrm{P}_{norm} = \mathrm{P}_{norm}\Gamma\tau_p\mathrm{G}_N/\tau_{nr}$ is the normalized pump rate.

We then perform small signal analysis like in ref. 16 and assume:

$$
X_{1,2} = \overline{X}_{1,2} + x_{1,2}e^{\lambda t}, Y_{1,2} = \overline{Y}_{1,2} + y_{1,2}e^{\lambda t}, \Delta\phi = \Delta\overline{\phi} + \delta\phi e^{\lambda t} \qquad \text{(A.4)}
$$

Substituting (A2) into (A1), neglecting higher order terms and assuming $\overline{X}_1 \approx \overline{X}_1$, results in:

$$
\begin{aligned}
x_1\lambda &= \frac{1}{2}(\overline{Y_1}-1)x_1 - \frac{\tau_{nr}}{\tau_{rad}}\frac{F_p\beta}{2}\frac{(Y_1+N0_{norm}}{|\overline{X}_1|^2}x_1 + (\frac{1}{2}\overline{X}_1 + \frac{\tau_{nr}}{\tau_{rad}}\frac{F_p\beta}{2}\frac{1}{\overline{X}_1})y_1 \\
&+ [\gamma\tau_p cos(\Delta\overline{\phi}) - \kappa\tau_p sin(\Delta\overline{\phi})]x_2 - [\gamma sin(\Delta\overline{\phi}) + \kappa cos(\Delta\overline{\phi})]\overline{X}_2\delta\phi && \text{(A.5)} \\
x_2\lambda &= \frac{1}{2}(\overline{Y_2}-1)x_2 - \frac{\tau_{nr}}{\tau_{rad}}\frac{F_p\beta}{2}\frac{(Y_2+N0_{norm}}{|\overline{X}_2|^2}x_2 + (\frac{1}{2}\overline{X}_2 + \frac{\tau_{nr}}{\tau_{rad}}\frac{F_p\beta}{2}\frac{1}{\overline{X}_2}) \\
&+ [\gamma\tau_p cos(\Delta\overline{\phi}) + \tau_p sin(\Delta\overline{\phi})]x_1 - [\gamma sin(\Delta\overline{\phi}) - \kappa cos(\Delta\overline{\phi})]\overline{X}_1\delta\phi && \text{(A.6)} \\
y_1\lambda &= T_{norm}(-\gamma_c y_1 - 2\overline{X}_1\overline{Y}_1 x_1 - \overline{X_1}^2 y_1) && \text{(A.7)} \\
y_2\lambda &= T_{norm}(-\gamma_c y_2 - 2\overline{X}_2\overline{Y}_2 x_2 - \overline{X_2}^2 y_2) && \text{(A.8)} \\
\delta\phi\lambda &= \frac{\alpha}{2}(y_2-y_1) + 2\kappa\tau_p cos(\Delta\overline{\phi})\frac{x_1-x_2}{\overline{X_1}} - 2\gamma\tau_p sin(\Delta\overline{\phi})\frac{x_1+x_2}{\overline{X}_1} - 2\gamma\tau_p cos(\Delta\overline{\phi})\delta\phi && \text{(A.9)}
\end{aligned}
$$

By considering equal pumping and neglecting the dissipative coupling by setting $\gamma = 0$, the above equations can be further simplified. We then add (A3a) and (A3b), as well as (A3c) and (A3d) and arrive at:

$$
\begin{aligned}
&(x_1+x_2)[\lambda - \frac{1}{2}(\overline{Y_1}-1) + \frac{\tau_{nr}}{\tau_{rad}}\frac{F_p\beta}{2}\frac{(Y_1+N_{0norm})}{|\overline{X}_1|^2}] \\
&\quad = (\frac{1}{2}\overline{X}_1 + \frac{\tau_{nr}}{\tau_{rad}}\frac{F_p\beta}{2}\frac{1}{\overline{X_1}})(y_1+y_2)(x_1+x_2)(-2T_{norm}\overline{X_1 Y_1}) \\
&\quad = [\lambda + T_{norm}(\gamma_c + \overline{X_1}^2)](y_1+y_2) \qquad \text{(A.10)}
\end{aligned}
$$

Combining (A4a) and (A4b), we have:

$$\lambda^2 + A_1\lambda + A_2 = 0 \qquad \text{(A.11)}$$

where $A_1 = T_{norm}(\gamma_c + \overline{X_1}^2) - \frac{1}{2}(\overline{Y_1}-1) + \frac{\tau_{nr}}{\tau_{rad}}\frac{F_p\beta}{2}\frac{(Y_1+N_{0norm})}{|\overline{X}_1|^2}$

Recall that $\frac{\tau_{nr}}{\tau_{rad}}\frac{F_p\beta}{2}\frac{(Y_1+N_{0norm})}{|\overline{X}_1|^2} = -\frac{1}{2}(\overline{Y_1}-1)$ and $A_1 = T_{norm}(\gamma_c + \overline{X_1}^2) - (Y_1 - 1)$. In order for the small perturbations to approach zero as time evolves, the real part of λ must be negative. This requires $A_1 = 2\mathrm{Re}(\lambda) > 0$. For the expression of A_1, the first term on the RHS signifies the radiative recombination of carriers by all means, and the second term denotes recombination involving only spontaneous emission. Therefore, $A_1 > 0$ always holds true.

We then subtract (A3b) from (A3a), as well as (A3d) from (A3c) and arrive at:

$$\begin{aligned}(x_1 - x_2)[\lambda - \frac{1}{2}(\overline{Y_1} - 1) + \frac{\tau_{nr}}{\tau_{rad}}\frac{F_p\beta}{2}\frac{Y_1 + N_{0norm}}{|\overline{X_1}|^2}] \\ = (\frac{1}{2}\overline{X_1} + \frac{\tau_{nr}}{\tau_{rad}}\frac{F_p\beta}{2}\frac{1}{\overline{\overline{X_1}}})(y_1 - y_2) - 2\kappa\tau_p cos(\Delta\overline{\phi})\overline{X_1}\delta\phi(x_1 - x_2)(-2T_{norm}\overline{X_1 Y_1}) \quad \text{(A.12)} \\ = [\lambda + T_{norm}(\gamma_c + \overline{X_1}^2)](y_1 - y_2) \quad \text{(A.13)}\end{aligned}$$

Substituting (A3e) into (A5a) results in:

$$\lambda^3 + B_1\lambda^2 + B_2\lambda + B_3 = 0 \quad \text{(A.14)}$$

where

$$\begin{aligned}B_1 &= T_{norm}(\gamma_c + \overline{X_1}^2) - (\overline{Y_1} - 1) \quad \text{(A.15)} \\ B_2 &= T_{norm}\overline{X_1 Y_1}(\overline{X_1} + \frac{\tau_{nr}}{\tau_{rad}}F_p\beta\frac{1}{\overline{\overline{X_1}}}) \\ &\quad - T_{norm}(\gamma_c + \overline{X_1}^2)(\overline{Y_1} - 1) + 4\kappa^2\tau_p^2 cos^2(\Delta\overline{\phi}) \quad \text{(A.16)} \\ B_3 &= 4\kappa^2\tau_p^2 cos^2(\Delta\phi)T_{norm}(\gamma_c + \overline{X_1}^2) + 2\alpha\kappa\tau_p T_{norm}\overline{X_1}^2\overline{Y_1}cos(\Delta\overline{\phi}) \quad \text{(A.17)}\end{aligned}$$

The solutions to (A6) are one real value and two conjugate complex values. The real solution gives the saddle-node bifurcations or pitchfork bifurcations while the complex solutions gives the Hopf bifurcations.

For very weak coupling, B_3 in (A7c) is approximately 0 and (A6) can be simplified to be quadratic. Consequentially, the solution of λ can then be approximated to be that of the relaxation oscillations (RO), where Re(λ) is the damping rate and Im(λ) is the RO frequency, which is $T_{norm}(\gamma_c + \overline{X_1}^2) + \frac{\tau_{nr}}{\tau_{rad}}F_p\beta\frac{Y_1 + N_{0norm}}{|\overline{X_1}|^2}$. In this case, a larger β always results in faster damping, therefore, enhancing the stability in the weak coupling region. The pump rate can also increase the damping rate for small β. For large β, the scenario becomes more complex and requires more detailed examination. However, since the damping rate can be approximated to be that of the RO as $\mathrm{T}_{norm}(\gamma_c + \overline{X_1}^2) + \frac{\tau_{nr}}{\tau_{rad}} F_p \beta \frac{Y_1 + N_{0norm}}{|X_1|^2}$, for very small β, the second term can be neglected. This means that as pump rate increases, a larger $\overline{X_1}^2$ gives a faster damping, i.e. better stability. While for larger β, the second term can not be neglected. Since $\overline{X_1}^2$ is now in the denominator, a larger $\overline{X_1}^2$ gives a slower damping rate, i.e. a worse stability.

To have the real parts of the solutions to λ be negative, and thus have stable phase locking, the following conditions must hold,

$$B_1 > 0, B_3 > 0, B_1 B_2 - B_3 > 0 \tag{A.18}$$

Since $\mathrm{B}_1 = \mathrm{A}_1 > 0$ has already been proven to be true, we focus on the second and the third conditions. The condition $\mathrm{B}_3 > 0$ makes the real solution negative, and thus yields,

$$4\kappa^2 \tau_p^2 cos^2(\Delta\bar{\phi}) T_{norm}(\gamma_c + \overline{X_1}^2) > -2\alpha\kappa\tau_p T_{norm} \overline{X_1}^2 \overline{Y_1} cos(\Delta\bar{\phi}) \tag{A.19}$$

In the case of zero detuning, this can be simplified to:

$$\kappa\tau_p > -\frac{\alpha T_{norm} \overline{X_1}^2 \overline{Y_1}}{2T_{norm}(\gamma_c + \overline{X_1}^2)}, when \Delta\bar{\phi} = 0, \tag{A.20}$$

And

$$\kappa\tau_p > \frac{\alpha T_{norm} \overline{X_1}^2 \overline{Y_1}}{2T_{norm}(\gamma_c + \overline{X_1}^2)}, when \Delta\bar{\phi} = \pi, \tag{A.21}$$

For the condition $\mathrm{B}_1\mathrm{B}_2 - \mathrm{B}_3 > 0$ to hold true, the real part of the complex solutions to λ must be negative. Consequentially, this yields a second order equation for κ,

$$C_1\kappa^2 + C_2\kappa + C_3 > 0 \tag{A.22}$$

where

$$C_1 = -4cos^2(\Delta\overline{\phi})(\overline{Y_1} - 1) \tag{A.23}$$

$$C_2 = -2\alpha T_{norm}cos(\Delta\overline{\phi})\overline{X_1}^2\overline{Y_1} \tag{A.24}$$

$$\begin{aligned} C_3 = {} & T_{norm}[T_{norm}(\gamma_c + \overline{X_1}^2) - (\overline{Y_1} - 1)] \\ & \times (\frac{\beta\tau_{nr}}{\tau_{rad}}\overline{Y_1} - \gamma_c\overline{Y_1} + \gamma_c + \overline{X_1}^2) \end{aligned} \tag{A.25}$$

An explicit expression describing the stable phase-locking conditions is challenging to obtain. Nevertheless, we can plot out and observe that the Hopf bifurcation boundary with $C_1\kappa^2 + C_2\kappa + C_3 = 0$, is a parabolic function, whose center and width vary with β and P. Each set of parameters generates a different parabolic function, and generates either zero, one or two roots, as shown in Fig. 4.1(a).

Bibliography

[1] T. H. Maiman, “Stimulated optical radiation in ruby,” *nature*, vol. 187, no. 4736, pp. 493–494, 1960.

[2] “Physics history,” *APS News*, vol. 19, no. 5, 2010.

[3] D. A. Miller, “Device requirements for optical interconnects to silicon chips,” *Proceedings of the IEEE*, vol. 97, no. 7, pp. 1166–1185, 2009.

[4] R.-M. Ma and R. F. Oulton, “Applications of nanolasers,” *Nature Nanotechnology*, vol. 14, no. 1, pp. 12–22, 2019.

[5] J. A. Schuller, E. S. Barnard, W. Cai, Y. C. Jun, J. S. White, and M. L. Brongersma, “Plasmonics for extreme light concentration and manipulation,” *Nature materials*, vol. 9, no. 3, pp. 193–204, 2010.

[6] O. Painter, R. Lee, A. Scherer, A. Yariv, J. O’brien, P. Dapkus, and I. Kim, “Two-dimensional photonic band-gap defect mode laser,” *Science*, vol. 284, no. 5421, pp. 1819–1821, 1999.

[7] H. Altug, D. Englund, and J. Vučković, “Ultrafast photonic crystal nanocavity laser,” *Nature physics*, vol. 2, no. 7, pp. 484–488, 2006.

[8] K. Nozaki, S. Kita, and T. Baba, “Room temperature continuous wave operation and controlled spontaneous emission in ultrasmall photonic crystal nanolaser,” *Optics express*, vol. 15, no. 12, pp. 7506–7514, 2007.

[9] S.-H. Kim, J.-H. Choi, S.-K. Lee, S.-H. Kim, S.-M. Yang, Y.-H. Lee, C. Seassal, P. Regrency, and P. Viktorovitch, “Optofluidic integration of a photonic crystal nanolaser,” *Optics Express*, vol. 16, no. 9, pp. 6515–6527, 2008.

[10] S. Matsuo, A. Shinya, T. Kakitsuka, K. Nozaki, T. Segawa, T. Sato, Y. Kawaguchi, and M. Notomi, “High-speed ultracompact buried heterostructure photonic-crystal laser with 13 fj of energy consumed per bit transmitted,” *Nature Photonics*, vol. 4, no. 9, pp. 648–654, 2010.

[11] B. Ellis, M. A. Mayer, G. Shambat, T. Sarmiento, J. Harris, E. E. Haller, and J. Vučković, "Ultralow-threshold electrically pumped quantum-dot photonic-crystal nanocavity laser," *Nature photonics*, vol. 5, no. 5, pp. 297–300, 2011.

[12] S. McCall, A. Levi, R. Slusher, S. Pearton, and R. Logan, "Whispering-gallery mode microdisk lasers," *Applied physics letters*, vol. 60, no. 3, pp. 289–291, 1992.

[13] T. Kippenberg, J. Kalkman, A. Polman, and K. Vahala, "Demonstration of an erbium-doped microdisk laser on a silicon chip," *Physical Review A*, vol. 74, no. 5, p. 051802, 2006.

[14] R. Chen, T.-T. D. Tran, K. W. Ng, W. S. Ko, L. C. Chuang, F. G. Sedgwick, and C. Chang-Hasnain, "Nanolasers grown on silicon," *Nature Photonics*, vol. 5, no. 3, pp. 170–175, 2011.

[15] S. S. Deka, S. H. Pan, Q. Gu, Y. Fainman, and A. El Amili, "Coupling in a dual metallo-dielectric nanolaser system," *Optics letters*, vol. 42, no. 22, pp. 4760–4763, 2017.

[16] R. F. Oulton, V. J. Sorger, T. Zentgraf, R.-M. Ma, C. Gladden, L. Dai, G. Bartal, and X. Zhang, "Plasmon lasers at deep subwavelength scale," *Nature*, vol. 461, no. 7264, pp. 629–632, 2009.

[17] M. Noginov, G. Zhu, A. Belgrave, R. Bakker, V. Shalaev, E. Narimanov, S. Stout, E. Herz, T. Suteewong, and U. Wiesner, "Demonstration of a spaser-based nanolaser," *Nature*, vol. 460, no. 7259, pp. 1110–1112, 2009.

[18] Y.-J. Lu, J. Kim, H.-Y. Chen, C. Wu, N. Dabidian, C. E. Sanders, C.-Y. Wang, M.-Y. Lu, B.-H. Li, X. Qiu, *et al.*, "Plasmonic nanolaser using epitaxially grown silver film," *science*, vol. 337, no. 6093, pp. 450–453, 2012.

[19] D. J. Bergman and M. I. Stockman, "Surface plasmon amplification by stimulated emission of radiation: quantum generation of coherent surface plasmons in nanosystems," *Physical review letters*, vol. 90, no. 2, p. 027402, 2003.

[20] M. P. Nezhad, A. Simic, O. Bondarenko, B. Slutsky, A. Mizrahi, L. Feng, V. Lomakin, and Y. Fainman, "Room-temperature subwavelength metallo-dielectric lasers," *Nature Photonics*, vol. 4, no. 6, pp. 395–399, 2010.

[21] M. T. Hill, Y.-S. Oei, B. Smalbrugge, Y. Zhu, T. De Vries, P. J. Van Veldhoven, F. W. Van Otten, T. J. Eijkemans, J. P. Turkiewicz, H. De Waardt, *et al.*, "Lasing in metallic-coated nanocavities," *Nature Photonics*, vol. 1, no. 10, pp. 589–594, 2007.

[22] K. Ding, M. Hill, Z. Liu, L. Yin, P. Van Veldhoven, and C.-Z. Ning, "Record performance of electrical injection sub-wavelength metallic-cavity semiconductor lasers at room temperature," *Optics express*, vol. 21, no. 4, pp. 4728–4733, 2013.

[23] Q. Gu, J. Shane, F. Vallini, B. Wingad, J. S. Smalley, N. C. Frateschi, and Y. Fainman, "Amorphous al2o3 shield for thermal management in electrically pumped metallo-dielectric nanolasers," *IEEE Journal of Quantum Electronics*, vol. 50, no. 7, pp. 499–509, 2014.

[24] S. H. Pan, Q. Gu, A. El Amili, F. Vallini, and Y. Fainman, “Dynamic hysteresis in a coherent high-β nanolaser,” *Optica*, vol. 3, no. 11, pp. 1260–1265, 2016.

[25] C.-Y. Fang, S. H. Pan, F. Vallini, A. Tukiainen, J. Lyytikäinen, G. Nylund, B. Kanté, M. Guina, A. El Amili, and Y. Fainman, “Lasing action in low-resistance nanolasers based on tunnel junctions,” *Optics letters*, vol. 44, no. 15, pp. 3669–3672, 2019.

[26] M. Khajavikhan, A. Simic, M. Katz, J. Lee, B. Slutsky, A. Mizrahi, V. Lomakin, and Y. Fainman, “Thresholdless nanoscale coaxial lasers,” *Nature*, vol. 482, no. 7384, pp. 204–207, 2012.

[27] C. Xu, W. E. Hayenga, M. Khajavikhan, and P. Likamwa, “Measuring the frequency response of optically pumped metal-clad nanolasers,” *Optics express*, vol. 27, no. 15, pp. 21834–21842, 2019.

[28] S. H. Pan, S. S. Deka, A. El Amili, Q. Gu, and Y. Fainman, “Nanolasers: second-order intensity correlation, direct modulation and electromagnetic isolation in array architectures,” *Progress in Quantum Electronics*, vol. 59, pp. 1–18, 2018.

[29] Q. Gu, B. Slutsky, F. Vallini, J. S. Smalley, M. P. Nezhad, N. C. Frateschi, and Y. Fainman, “Purcell effect in sub-wavelength semiconductor lasers,” *Optics express*, vol. 21, no. 13, pp. 15603–15617, 2013.

[30] F. Qian, Y. Li, S. Gradečak, H.-G. Park, Y. Dong, Y. Ding, Z. L. Wang, and C. M. Lieber, “Multi-quantum-well nanowire heterostructures for wavelength-controlled lasers,” *Nature materials*, vol. 7, no. 9, pp. 701–706, 2008.

[31] Y. Fu, H. Zhu, C. C. Stoumpos, Q. Ding, J. Wang, M. G. Kanatzidis, X. Zhu, and S. Jin, “Broad wavelength tunable robust lasing from single-crystal nanowires of cesium lead halide perovskites (cspbx3, x= cl, br, i),” *ACS nano*, vol. 10, no. 8, pp. 7963–7972, 2016.

[32] Y. Lu, F. Gu, C. Meng, H. Yu, Y. Ma, W. Fang, and L. Tong, “Multicolour laser from a single bandgap-graded cdsse alloy nanoribbon,” *Optics express*, vol. 21, no. 19, pp. 22314–22319, 2013.

[33] X. Liu, Q. Zhang, J. N. Yip, Q. Xiong, and T. C. Sum, “Wavelength tunable single nanowire lasers based on surface plasmon polariton enhanced burstein–moss effect,” *Nano letters*, vol. 13, no. 11, pp. 5336–5343, 2013.

[34] A. Yang, T. B. Hoang, M. Dridi, C. Deeb, M. H. Mikkelsen, G. C. Schatz, and T. W. Odom, “Real-time tunable lasing from plasmonic nanocavity arrays,” *Nature communications*, vol. 6, no. 1, pp. 1–7, 2015.

[35] P. Xu, J. Gong, X. Guo, C. Xin, H. Wu, P. Qing, X. Lin, W. Fang, D. Di, and L. Tong, “Fast lasing wavelength tuning in single nanowires,” *Advanced Optical Materials*, vol. 7, no. 20, p. 1900797, 2019.

[36] M. Zapf, R. Roder, K. Winkler, L. Kaden, J. Greil, M. Wille, M. Grundmann, R. Schmidt-Grund, A. Lugstein, and C. Ronning, “Dynamical tuning of nanowire lasing spectra,” *Nano letters*, vol. 17, no. 11, pp. 6637–6643, 2017.

[37] S. S. Deka, S. H. Pan, S. Jiang, A. El Amili, F. Vallini, Q. Gu, and Y. Fainman, “Real-time dynamic wavelength tuning and intensity modulation of metal-clad nanolasers,” *Optics Express*, vol. 28, no. 19, pp. 27346–27357, 2020.

[38] S. Wang and H. Winful, “Dynamics of phase-locked semiconductor laser arrays,” *Applied physics letters*, vol. 52, no. 21, pp. 1774–1776, 1988.

[39] H. Winful and S. Wang, “Stability of phase locking in coupled semiconductor laser arrays,” *Applied physics letters*, vol. 53, no. 20, pp. 1894–1896, 1988.

[40] S. S. Deka, S. Jiang, S. H. Pan, and Y. Fainman, “Nanolaser arrays: toward application-driven dense integration,” *Nanophotonics*, vol. 10, no. 1, pp. 149–169, 2020.

[41] P. Hamel, S. Haddadi, F. Raineri, P. Monnier, G. Beaudoin, I. Sagnes, A. Levenson, and A. M. Yacomotti, “Spontaneous mirror-symmetry breaking in coupled photonic-crystal nanolasers,” *Nature Photonics*, vol. 9, no. 5, pp. 311–315, 2015.

[42] X. Yang, Z. Shan, Z. Luo, X. Hu, H. Liu, Q. Liu, Y. Zhang, X. Zhang, M. Shoaib, J. Qu, *et al.*, “An electrically controlled wavelength-tunable nanoribbon laser,” *ACS nano*, vol. 14, no. 3, pp. 3397–3404, 2020.

[43] Q. Gu, J. S. Smalley, M. P. Nezhad, A. Simic, J. H. Lee, M. Katz, O. Bondarenko, B. Slutsky, A. Mizrahi, V. Lomakin, *et al.*, “Subwavelength semiconductor lasers for dense chip-scale integration,” *Advances in Optics and Photonics*, vol. 6, no. 1, pp. 1–56, 2014.

[44] G. Cossu, A. Khalid, P. Choudhury, R. Corsini, and E. Ciaramella, “3.4 gbit/s visible optical wireless transmission based on rgb led,” *Optics express*, vol. 20, no. 26, pp. B501–B506, 2012.

[45] M.-H. Zhuge, C. Pan, Y. Zheng, J. Tang, S. Ullah, Y. Ma, and Q. Yang, “Wavelength-tunable micro/nanolasers,” *Advanced Optical Materials*, vol. 7, no. 17, p. 1900275, 2019.

[46] Y.-J. Lu, C.-Y. Wang, J. Kim, H.-Y. Chen, M.-Y. Lu, Y.-C. Chen, W.-H. Chang, L.-J. Chen, M. I. Stockman, C.-K. Shih, *et al.*, “All-color plasmonic nanolasers with ultralow thresholds: autotuning mechanism for single-mode lasing,” *Nano letters*, vol. 14, no. 8, pp. 4381–4388, 2014.

[47] H. Zhu, Y. Fu, F. Meng, X. Wu, Z. Gong, Q. Ding, M. V. Gustafsson, M. T. Trinh, S. Jin, and X. Zhu, “Lead halide perovskite nanowire lasers with low lasing thresholds and high quality factors,” *Nature materials*, vol. 14, no. 6, pp. 636–642, 2015.

[48] Z. Yang, D. Wang, C. Meng, Z. Wu, Y. Wang, Y. Ma, L. Dai, X. Liu, T. Hasan, X. Liu, *et al.*, “Broadly defining lasing wavelengths in single bandgap-graded semiconductor nanowires,” *Nano letters*, vol. 14, no. 6, pp. 3153–3159, 2014.

[49] S. Liu, C. Li, J. J. Figiel, S. R. Brueck, I. Brener, and G. T. Wang, “Continuous and dynamic spectral tuning of single nanowire lasers with subnanometer resolution using hydrostatic pressure,” *Nanoscale*, vol. 7, no. 21, pp. 9581–9588, 2015.

[50] S. Kreinberg, K. Laiho, F. Lohof, W. E. Hayenga, P. Holewa, C. Gies, M. Khajavikhan, and S. Reitzenstein, “Thresholdless transition to coherent emission at telecom wavelengths from coaxial nanolasers,” *arXiv preprint arXiv:1905.09924*, 2019.

[51] A. A. Vyshnevyy and D. Y. Fedyanin, “Lasing threshold of thresholdless and non-thresholdless metal-semiconductor nanolasers,” *Optics Express*, vol. 26, no. 25, pp. 33473–33483, 2018.

[52] D. Y. Fedyanin, A. V. Krasavin, A. V. Arsenin, and A. V. Zayats, “Lasing at the nanoscale: coherent emission of surface plasmons by an electrically driven nanolaser,” *Nanophotonics*, vol. 9, no. 12, pp. 3965–3975, 2020.

[53] D. Massoubre, J.-L. Oudar, A. O’Hare, M. Gay, L. Bramerie, J.-C. Simon, A. Shen, and J. Decobert, “Analysis of thermal limitations in high-speed microcavity saturable absorber all-optical switching gates,” *Journal of lightwave technology*, vol. 24, no. 9, p. 3400, 2006.

[54] J. S. Smalley, Q. Gu, and Y. Fainman, “Temperature dependence of the spontaneous emission factor in subwavelength semiconductor lasers,” *IEEE Journal of Quantum Electronics*, vol. 50, no. 3, pp. 175–185, 2014.

[55] L. A. Coldren, S. W. Corzine, and M. L. Mashanovitch, *Diode lasers and photonic integrated circuits*, vol. 218. John Wiley & Sons, 2012.

[56] S. Schlichting, G. M. O. Hönig, J. Müßener, P. Hille, T. Grieb, S. Westerkamp, J. Teubert, J. Schörmann, M. R. Wagner, A. Rosenauer, *et al.*, “Suppression of the quantum-confined stark effect in polar nitride heterostructures,” *Communications Physics*, vol. 1, no. 1, pp. 1–8, 2018.

[57] J. W. Robinson, J. H. Rice, K. H. Lee, J. H. Na, R. A. Taylor, D. G. Hasko, R. A. Oliver, M. J. Kappers, C. J. Humphreys, and G. A. D. Briggs, “Quantum-confined stark effect in a single ingan quantum dot under a lateral electric field,” *Applied Physics Letters*, vol. 86, no. 21, p. 213103, 2005.

[58] D. O’Brien, M. Settle, T. Karle, A. Michaeli, M. Salib, and T. Krauss, “Coupled photonic crystal heterostructure nanocavities,” *Optics express*, vol. 15, no. 3, pp. 1228–1233, 2007.

[59] M. Marconi, F. Raineri, A. Levenson, A. M. Yacomotti, J. Javaloyes, S. H. Pan, A. El Amili, and Y. Fainman, “Mesoscopic limit cycles in coupled nanolasers,” *Physical Review Letters*, vol. 124, no. 21, p. 213602, 2020.

[60] A. Nakagawa, S. Ishii, and T. Baba, “Photonic molecule laser composed of gainasp microdisks,” *Applied Physics Letters*, vol. 86, no. 4, p. 041112, 2005.

[61] S. V. Boriskina, "Spectrally engineered photonic molecules as optical sensors with enhanced sensitivity: a proposal and numerical analysis," *JOSA B*, vol. 23, no. 8, pp. 1565–1573, 2006.

[62] S. V. Boriskina, "Coupling of whispering-gallery modes in size-mismatched microdisk photonic molecules," *Optics letters*, vol. 32, no. 11, pp. 1557–1559, 2007.

[63] E. I. Smotrova, A. I. Nosich, T. M. Benson, and P. Sewell, "Optical coupling of whispering-gallery modes of two identical microdisks and its effect on photonic molecule lasing," *IEEE Journal of Selected Topics in Quantum Electronics*, vol. 12, no. 1, pp. 78–85, 2006.

[64] S. Ishii, A. Nakagawa, and T. Baba, "Modal characteristics and bistability in twin microdisk photonic molecule lasers," *IEEE Journal of selected topics in Quantum Electronics*, vol. 12, no. 1, pp. 71–77, 2006.

[65] M. T. Hill, H. J. Dorren, T. De Vries, X. J. Leijtens, J. H. Den Besten, B. Smalbrugge, Y.-S. Oei, H. Binsma, G.-D. Khoe, and M. K. Smit, "A fast low-power optical memory based on coupled micro-ring lasers," *nature*, vol. 432, no. 7014, pp. 206–209, 2004.

[66] H. Hodaei, M. A. Miri, A. U. Hassan, W. Hayenga, M. Heinrich, D. Christodoulides, and M. Khajavikhan, "Parity-time-symmetric coupled microring lasers operating around an exceptional point," *Optics letters*, vol. 40, no. 21, pp. 4955–4958, 2015.

[67] M. Liertzer, L. Ge, A. Cerjan, A. Stone, H. E. Türeci, and S. Rotter, "Pump-induced exceptional points in lasers," *Physical Review Letters*, vol. 108, no. 17, p. 173901, 2012.

[68] M. Ghulinyan, C. Oton, G. Bonetti, Z. Gaburro, and L. Pavesi, "Free-standing porous silicon single and multiple optical cavities," *Journal of Applied Physics*, vol. 93, no. 12, pp. 9724–9729, 2003.

[69] K. A. Atlasov, K. F. Karlsson, A. Rudra, B. Dwir, and E. Kapon, "Wavelength and loss splitting in directly coupled photonic-crystal defect microcavities," *Optics express*, vol. 16, no. 20, pp. 16255–16264, 2008.

[70] P. B. Johnson and R.-W. Christy, "Optical constants of the noble metals," *Physical review B*, vol. 6, no. 12, p. 4370, 1972.

[71] Q. Wang, H. Zhao, X. Du, W. Zhang, M. Qiu, and Q. Li, "Hybrid photonic-plasmonic molecule based on metal/si disks," *Optics express*, vol. 21, no. 9, pp. 11037–11047, 2013.

[72] S. Haddadi, P. Hamel, G. Beaudoin, I. Sagnes, C. Sauvan, P. Lalanne, J. A. Levenson, and A. Yacomotti, "Photonic molecules: tailoring the coupling strength and sign," *Optics express*, vol. 22, no. 10, pp. 12359–12368, 2014.

[73] E. I. Smotrova, A. I. Nosich, T. M. Benson, and P. Sewell, "Threshold reduction in a cyclic photonic molecule laser composed of identical microdisks with whispering-gallery modes," *Optics letters*, vol. 31, no. 7, pp. 921–923, 2006.

[74] C. V. Poulton, A. Yaacobi, D. B. Cole, M. J. Byrd, M. Raval, D. Vermeulen, and M. R. Watts, "Coherent solid-state lidar with silicon photonic optical phased arrays," *Optics letters*, vol. 42, no. 20, pp. 4091–4094, 2017.

[75] B. G. Lee, J. Kansky, A. K. Goyal, C. Pflügl, L. Diehl, M. A. Belkin, A. Sanchez, and F. Capasso, "Beam combining of quantum cascade laser arrays," *Optics Express*, vol. 17, no. 18, pp. 16216–16224, 2009.

[76] D. Kedar and S. Arnon, "Urban optical wireless communication networks: the main challenges and possible solutions," *IEEE Communications Magazine*, vol. 42, no. 5, pp. S2–S7, 2004.

[77] D. Kwong, A. Hosseini, J. Covey, Y. Zhang, X. Xu, H. Subbaraman, and R. T. Chen, "On-chip silicon optical phased array for two-dimensional beam steering," *Optics letters*, vol. 39, no. 4, pp. 941–944, 2014.

[78] J. K. Doylend, M. Heck, J. T. Bovington, J. D. Peters, L. Coldren, and J. Bowers, "Two-dimensional free-space beam steering with an optical phased array on silicon-on-insulator," *Optics express*, vol. 19, no. 22, pp. 21595–21604, 2011.

[79] C. Henry, "Theory of the linewidth of semiconductor lasers," *IEEE Journal of Quantum Electronics*, vol. 18, no. 2, pp. 259–264, 1982.

[80] S. Shahin, F. Vallini, F. Monifi, M. Rabinovich, and Y. Fainman, "Heteroclinic dynamics of coupled semiconductor lasers with optoelectronic feedback," *Optics letters*, vol. 41, no. 22, pp. 5238–5241, 2016.

[81] B. Bahari, A. Ndao, F. Vallini, A. El Amili, Y. Fainman, and B. Kanté, "Nonreciprocal lasing in topological cavities of arbitrary geometries," *Science*, vol. 358, no. 6363, pp. 636–640, 2017.

[82] M. P. Hokmabadi, N. S. Nye, R. El-Ganainy, D. N. Christodoulides, and M. Khajavikhan, "Supersymmetric laser arrays," *Science*, vol. 363, no. 6427, pp. 623–626, 2019.

[83] Z. Jia, L. Wang, J. Zhang, Y. Zhao, C. Liu, S. Zhai, N. Zhuo, J. Liu, L. Wang, S. Liu, *et al.*, "Phase-locked array of quantum cascade lasers with an intracavity spatial filter," *Applied Physics Letters*, vol. 111, no. 6, p. 061108, 2017.

[84] T.-Y. Kao, J. L. Reno, and Q. Hu, "Phase-locked laser arrays through global antenna mutual coupling," *Nature Photonics*, vol. 10, no. 8, pp. 541–546, 2016.

[85] M. Adams, D. Jevtics, M. Strain, I. Henning, and A. Hurtado, "High-frequency dynamics of evanescently-coupled nanowire lasers," *Scientific reports*, vol. 9, no. 1, pp. 1–7, 2019.

[86] M. Adams, N. Li, B. Cemlyn, H. Susanto, and I. Henning, "Effects of detuning, gain-guiding, and index antiguiding on the dynamics of two laterally coupled semiconductor lasers," *Physical Review A*, vol. 95, no. 5, p. 053869, 2017.

[87] H. Erzgräber, S. Wieczorek, and B. Krauskopf, "Dynamics of two laterally coupled semiconductor lasers: Strong-and weak-coupling theory," *Physical Review E*, vol. 78, no. 6, p. 066201, 2008.

[88] J. Shena, J. Hizanidis, V. Kovanis, and G. P. Tsironis, "Turbulent chimeras in large semiconductor laser arrays," *Scientific reports*, vol. 7, no. 1, pp. 1–8, 2017.

[89] D. T. Cassidy, "Spontaneous-emission factor of semiconductor diode lasers," *JOSA B*, vol. 8, no. 4, pp. 747–752, 1991.

[90] E. Schlottmann, S. Holzinger, B. Lingnau, K. Lüdge, C. Schneider, M. Kamp, S. Höfling, J. Wolters, and S. Reitzenstein, "Injection locking of quantum-dot microlasers operating in the few-photon regime," *Physical Review Applied*, vol. 6, no. 4, p. 044023, 2016.

[91] S. Kreinberg, X. Porte, D. Schicke, B. Lingnau, C. Schneider, S. Höfling, I. Kanter, K. Lüdge, and S. Reitzenstein, "Mutual coupling and synchronization of optically coupled quantum-dot micropillar lasers at ultra-low light levels," *Nature communications*, vol. 10, no. 1, pp. 1–11, 2019.

[92] T. Suhr, P. T. Kristensen, and J. Mørk, "Phase-locking regimes of photonic crystal nanocavity laser arrays," *Applied Physics Letters*, vol. 99, no. 25, p. 251104, 2011.

[93] Y. Zhao, C. Qian, K. Qiu, Y. Gao, and X. Xu, "Ultrafast optical switching using photonic molecules in photonic crystal waveguides," *Optics express*, vol. 23, no. 7, pp. 9211–9220, 2015.

[94] Z. Gao, D. Siriani, and K. D. Choquette, "Coupling coefficient in antiguided coupling: magnitude and sign control," *JOSA B*, vol. 35, no. 2, pp. 417–422, 2018.

[95] B. Ermentrout, *Simulating, analyzing, and animating dynamical systems: a guide to XPPAUT for researchers and students*. SIAM, 2002.

[96] P. Antonik, M. C. Wicks, H. D. Griffiths, and C. J. Baker, "Frequency diverse array radars," in *2006 IEEE Conference on Radar*, pp. 3–pp, IEEE, 2006.

[97] A.-M. Yao, W. Wu, and D.-G. Fang, "Frequency diverse array antenna using time-modulated optimized frequency offset to obtain time-invariant spatial fine focusing beampattern," *IEEE Transactions on Antennas and Propagation*, vol. 64, no. 10, pp. 4434–4446, 2016.

[98] Y. Xu, X. Shi, J. Xu, and P. Li, "Range-angle-dependent beamforming of pulsed frequency diverse array," *IEEE Transactions on Antennas and Propagation*, vol. 63, no. 7, pp. 3262–3267, 2015.

[99] G. Crosnier, D. Sanchez, S. Bouchoule, P. Monnier, G. Beaudoin, I. Sagnes, R. Raj, and F. Raineri, "Hybrid indium phosphide-on-silicon nanolaser diode," *Nature Photonics*, vol. 11, no. 5, pp. 297–300, 2017.

[100] L. Liu, R. Kumar, K. Huybrechts, T. Spuesens, G. Roelkens, E.-J. Geluk, T. De Vries, P. Regreny, D. Van Thourhout, R. Baets, *et al.*, “An ultra-small, low-power, all-optical flip-flop memory on a silicon chip,” *Nature Photonics*, vol. 4, no. 3, p. 182, 2010.

[101] P. L. McMahon, A. Marandi, Y. Haribara, R. Hamerly, C. Langrock, S. Tamate, T. Inagaki, H. Takesue, S. Utsunomiya, K. Aihara, *et al.*, “A fully programmable 100-spin coherent ising machine with all-to-all connections,” *Science*, vol. 354, no. 6312, pp. 614–617, 2016.

[102] M. Smit, J. Van der Tol, and M. Hill, “Moore’s law in photonics,” *Laser & Photonics Reviews*, vol. 6, no. 1, pp. 1–13, 2012.

[103] H. Han and K. A. Shore, “Zero crosstalk regime direct modulation of mutually coupled nanolasers,” *IEEE Photonics Journal*, vol. 9, no. 4, pp. 1–12, 2017.

[104] S. Hachuda, S. Otsuka, S. Kita, T. Isono, M. Narimatsu, K. Watanabe, Y. Goshima, and T. Baba, “Selective detection of sub-atto-molar streptavidin in 10 13-fold impure sample using photonic crystal nanolaser sensors,” *Optics express*, vol. 21, no. 10, pp. 12815–12821, 2013.

[105] S. Kita, K. Nozaki, S. Hachuda, H. Watanabe, Y. Saito, S. Otsuka, T. Nakada, Y. Arita, and T. Baba, “Photonic crystal point-shift nanolasers with and without nanoslots—design, fabrication, lasing, and sensing characteristics,” *IEEE journal of selected topics in quantum electronics*, vol. 17, no. 6, pp. 1632–1647, 2011.

[106] H. Abe, M. Narimatsu, T. Watanabe, T. Furumoto, Y. Yokouchi, Y. Nishijima, S. Kita, A. Tomitaka, S. Ota, Y. Takemura, *et al.*, “Living-cell imaging using a photonic crystal nanolaser array,” *Optics express*, vol. 23, no. 13, pp. 17056–17066, 2015.

[107] J. Feng, W. Wen, X. Wei, X. Jiang, M. Cao, X. Wang, X. Zhang, L. Jiang, and Y. Wu, “Random organic nanolaser arrays for cryptographic primitives,” *Advanced Materials*, vol. 31, no. 36, p. 1807880, 2019.

[108] S. Kita, K. Nozaki, and T. Baba, “Refractive index sensing utilizing a cw photonic crystal nanolaser and its array configuration,” *optics express*, vol. 16, no. 11, pp. 8174–8180, 2008.

[109] J.-J. Wu, H. Gao, R. Lai, M.-P. Zhuo, J. Feng, X.-D. Wang, Y. Wu, L.-S. Liao, and L. Jiang, “Near-infrared organic single-crystal nanolaser arrays activated by excited-state intramolecular proton transfer,” *Matter*, vol. 2, no. 5, pp. 1233–1243, 2020.

[110] H. Kim, W.-J. Lee, A. C. Farrell, J. S. Morales, P. Senanayake, S. V. Prikhodko, T. J. Ochalski, and D. L. Huffaker, “Monolithic ingaas nanowire array lasers on silicon-on-insulator operating at room temperature,” *Nano letters*, vol. 17, no. 6, pp. 3465–3470, 2017.

[111] H. Yan, R. He, J. Johnson, M. Law, R. J. Saykally, and P. Yang, “Dendritic nanowire ultraviolet laser array,” *Journal of the American Chemical Society*, vol. 125, no. 16, pp. 4728–4729, 2003.

[112] T. Watanabe, H. Abe, Y. Nishijima, and T. Baba, "Array integration of thousands of photonic crystal nanolasers," *Applied Physics Letters*, vol. 104, no. 12, p. 121108, 2014.

[113] S. T. Ha, Y. H. Fu, N. K. Emani, Z. Pan, R. M. Bakker, R. Paniagua-Domínguez, and A. I. Kuznetsov, "Directional lasing in resonant semiconductor nanoantenna arrays," *Nature nanotechnology*, vol. 13, no. 11, pp. 1042–1047, 2018.

[114] A. Kodigala, T. Lepetit, Q. Gu, B. Bahari, Y. Fainman, and B. Kanté, "Lasing action from photonic bound states in continuum," *Nature*, vol. 541, no. 7636, pp. 196–199, 2017.

[115] T.-J. Lin, H.-L. Chen, Y.-F. Chen, and S. Cheng, "Room-temperature nanolaser from cdse nanotubes embedded in anodic aluminum oxide nanocavity arrays," *Applied Physics Letters*, vol. 93, no. 22, p. 223903, 2008.

[116] K. Wang, Z. Gu, S. Liu, W. Sun, N. Zhang, S. Xiao, and Q. Song, "High-density and uniform lead halide perovskite nanolaser array on silicon," *The journal of physical chemistry letters*, vol. 7, no. 13, pp. 2549–2555, 2016.

[117] D. Wang, A. Yang, W. Wang, Y. Hua, R. D. Schaller, G. C. Schatz, and T. W. Odom, "Band-edge engineering for controlled multi-modal nanolasing in plasmonic superlattices," *Nature nanotechnology*, vol. 12, no. 9, p. 889, 2017.

[118] S. Pourjamal, T. K. Hakala, M. Necada, F. Freire-Fernandez, M. Kataja, H. Rekola, J.-P. Martikainen, P. Torma, and S. Van Dijken, "Lasing in ni nanodisk arrays," *ACS nano*, vol. 13, no. 5, pp. 5686–5692, 2019.

[119] W. Zhou, M. Dridi, J. Y. Suh, C. H. Kim, D. T. Co, M. R. Wasielewski, G. C. Schatz, T. W. Odom, *et al.*, "Lasing action in strongly coupled plasmonic nanocavity arrays," *Nature nanotechnology*, vol. 8, no. 7, p. 506, 2013.

[120] X. Meng, J. Liu, A. V. Kildishev, and V. M. Shalaev, "Highly directional spaser array for the red wavelength region," *Laser & Photonics Reviews*, vol. 8, no. 6, pp. 896–903, 2014.

[121] M. P. Knudson, R. Li, D. Wang, W. Wang, R. D. Schaller, and T. W. Odom, "Polarization-dependent lasing behavior from low-symmetry nanocavity arrays," *ACS nano*, vol. 13, no. 7, pp. 7435–7441, 2019.

[122] J. Y. Suh, C. H. Kim, W. Zhou, M. D. Huntington, D. T. Co, M. R. Wasielewski, and T. W. Odom, "Plasmonic bowtie nanolaser arrays," *Nano letters*, vol. 12, no. 11, pp. 5769–5774, 2012.

[123] F. van Beijnum, P. J. van Veldhoven, E. J. Geluk, M. J. de Dood, W. Gert, and M. P. van Exter, "Surface plasmon lasing observed in metal hole arrays," *Physical review letters*, vol. 110, no. 20, p. 206802, 2013.

[124] C. Huang, W. Sun, Y. Fan, Y. Wang, Y. Gao, N. Zhang, K. Wang, S. Liu, S. Wang, S. Xiao, *et al.*, "Formation of lead halide perovskite based plasmonic nanolasers and nanolaser arrays by tailoring the substrate," *ACS nano*, vol. 12, no. 4, pp. 3865–3874, 2018.

[125] Y.-H. Chou, K.-B. Hong, C.-T. Chang, T.-C. Chang, Z.-T. Huang, P.-J. Cheng, J.-H. Yang, M.-H. Lin, T.-R. Lin, K.-P. Chen, *et al.*, "Ultracompact pseudowedge plasmonic lasers and laser arrays," *Nano letters*, vol. 18, no. 2, pp. 747–753, 2018.

[126] M. Parto, W. Hayenga, A. Marandi, D. N. Christodoulides, and M. Khajavikhan, "Realizing spin hamiltonians in nanoscale active photonic lattices," *Nature materials*, vol. 19, no. 7, pp. 725–731, 2020.

[127] H. Altug and J. Vučković, "Photonic crystal nanocavity array laser," *Optics express*, vol. 13, no. 22, pp. 8819–8828, 2005.

[128] W. Hayenga, M. Parto, H. Hodaei, P. LiKamWa, D. Christodoulides, and M. Khajavikhan, "Coupled metallic nanolaser arrays," in *2017 Conference on Lasers and Electro-Optics (CLEO)*, pp. 1–1, IEEE, 2017.

[129] W. Hayenga, M. Parto, E. S. Cristobal, D. Christodoulides, and M. Khajavikhan, "Direct generation of structured light in metallic nanolaser arrays," in *2018 Conference on Lasers and Electro-Optics (CLEO)*, pp. 1–2, IEEE, 2018.

[130] M. Parto, W. Hayenga, D. Christodoulides, and M. Khajavikhan, "Mode-dependent coupling and vectorial optical vortices in metallic nanolaser arrays," in *2019 Conference on Lasers and Electro-Optics (CLEO)*, pp. 1–2, IEEE, 2019.

[131] A. F. Koenderink, "Plasmon nanocavity array lasers: Cooperating over losses and competing for gain," *ACS nano*, vol. 13, no. 7, pp. 7377–7382, 2019.

[132] M. B. Ross, C. A. Mirkin, and G. C. Schatz, "Optical properties of one-, two-, and three-dimensional arrays of plasmonic nanostructures," *The journal of physical chemistry C*, vol. 120, no. 2, pp. 816–830, 2016.

[133] P. Xu, J. Gong, X. Guo, C. Xin, H. Wu, P. Qing, X. Lin, W. Fang, D. Di, and L. Tong, "Fast lasing wavelength tuning in single nanowires," *Advanced Optical Materials*, vol. 7, no. 20, p. 1900797, 2019.

[134] J. Cheng, C. Shieh, X. Huang, G. Liu, M. Murty, C.-C. Lin, and D. Xu, "Efficient long wavelength algainas vertical-cavity surface-emitting lasers for coarse wdm applications over multimode fibre," *Electronics Letters*, vol. 40, no. 19, pp. 1184–1185, 2004.

[135] M. T. Hill and M. C. Gather, "Advances in small lasers," *Nature Photonics*, vol. 8, no. 12, pp. 908–918, 2014.

[136] M. Lorke, T. Suhr, N. Gregersen, and J. Mørk, "Theory of nanolaser devices: Rate equation analysis versus microscopic theory," *Physical Review B*, vol. 87, no. 20, p. 205310, 2013.

[137] B. Bahari, L.-Y. Hsu, S. Pan, D. Preece, A. Ndao, A. E. Amili, Y. Fainman, and B. Kanté, "Topological lasers generating and multiplexing topological light," *arXiv preprint arXiv:1904.11873*, 2019.

[138] Z.-K. Shao, H.-Z. Chen, S. Wang, X.-R. Mao, Z.-Q. Yang, S.-L. Wang, X.-X. Wang, X. Hu, and R.-M. Ma, "A high-performance topological bulk laser based on band-inversion-induced reflection," *Nature nanotechnology*, vol. 15, no. 1, pp. 67–72, 2020.

[139] Z.-Q. Yang, Z.-K. Shao, H.-Z. Chen, X.-R. Mao, and R.-M. Ma, "Spin-momentum-locked edge mode for topological vortex lasing," *Physical Review Letters*, vol. 125, no. 1, p. 013903, 2020.

[140] Q. Zhan, "Cylindrical vector beams: from mathematical concepts to applications," *Advances in Optics and Photonics*, vol. 1, no. 1, pp. 1–57, 2009.

[141] A. M. Yao and M. J. Padgett, "Orbital angular momentum: origins, behavior and applications," *Advances in Optics and Photonics*, vol. 3, no. 2, pp. 161–204, 2011.

[142] J. S. T. Gongora, A. E. Miroshnichenko, Y. S. Kivshar, and A. Fratalocchi, "Anapole nanolasers for mode-locking and ultrafast pulse generation," *Nature communications*, vol. 8, no. 1, pp. 1–9, 2017.